ABSTRACT

Title of Dissertation:	ELECTRICAL PROPERTIES OF A TUBE-IN-A-TUBE SEMICONDUCTOR
	Allen L. Ng, Doctor of Philosophy, 2017
Dissertation directed by:	Professor YuHuang Wang Department of Chemistry and Biochemistry

Tube-in-a-tube (Tube^2) nanostructures were synthesized through the outer-wall selective covalent functionalization of double-walled carbon nanotubes (DWCNTs) at high functional densities. Upon functionalization, the properties of individual walls within the structure decouple resulting in an electrically insulating functional outer tube while the inner tube retains exceptional CNT properties. The exceptional electrical properties of Tube^2 semiconductor structures were demonstrated for applications that include molecular and biological sensors and patterning of CNT-based structures with electronic type specificity.

Tube^2 thin film transistor (TFT) sensors exhibited simultaneous ultrahigh sensitivity and selectivity towards chemical and biological targets. Carboxylic acid terminated Tube^2 sensors displayed an NH_3 sensitivity of 60 nM, which is comparable with

small molecule aqueous solution detection using state-of-the-art TFT sensors while simultaneously attaining 6,000 times higher chemical selectivity towards a variety of amine containing analyte molecules over carboxylic acids. Similarly, 23-base oligonucleotide terminated Tube^2 sensors demonstrated concomitant sensitivity down to 5 nM towards their complementary sequence without amplification techniques and single mismatch selectivity without the use of a gate electrode. Unique sensor architectures can be designed with the requirement of a gate electrode, such as the creation of millimeter-scale point sensors.

The optical features and unique structural features of Tube^2 thin films were also exploited to address the challenge of patterning CNT nanostructures with electronic type specificity. Patterned dot arrays and conductive pathways were created on an initially insulating Tube^2 thin film by tuning the resonance of the direct-writing laser with the electronic type of the inner tube (*i.e.*, metallic or semiconducting). The successful patterning of Tube^2 thin films was unambiguously confirmed with *in situ* Raman spectral imaging and electrical characterization.

Furthermore, a hybrid 2-D carbon nanostructure comprised of a functionalized graphene that covers a semiconducting (6,5) SWCNT network (fG/sSWCNT) was developed. The hybrid fG/sSWCNT nanostructure exhibits similar structural and electrical properties as a semiconducting Tube^2 thin film, but possesses a transconductance that is an order of magnitude larger than Tube^2 and ON/OFF ratios as high as 5400 without the useful of further processing steps such as electrical breakdown.

ELECTRICAL PROPERTIES OF A TUBE-IN-A-TUBE SEMICONDUCTOR

by

Allen Lee Ng

Dissertation submitted to the Faculty of the Graduate School of the
University of Maryland, College Park, in partial fulfillment
of the requirements for the degree of
Doctor of Philosophy
2017

Advisory Committee:
Professor YuHuang Wang, Chair
Professor Cheng S. Lee
Professor Sang Bok Lee
Professor Zhihong Nie
Professor Min Ouyang, Dean's Representative

Acknowledgements

Being a part of the graduate process at the University of Maryland has been an otherworldly and breathless experience. Over the years, I have been fortunate enough to have the assistance of so many people who supported and encouraged me through positive and occasionally trying times. As such, it is only fitting that I acknowledge that without them this body of work would be take a far lesser form.

I would like to start by acknowledging my family who have made immense sacrifices and understanding that allowed me to freely pursue my own direction. Next, I would like to acknowledge my friends for being there when I needed them. They have always been a second family to me. Among them special thanks goes out to Emad Din, Joey Jenkins, Tony Chou, Zhengzhe Liu, Keely Armet, Aaron Geller, and Lyndsey Powell all for different, but priceless contributions.

I would also like to thank the numerous past and current lab mates in the YuHuang Wang group for their welcoming camaraderie and invaluable assistance over my years as a graduate student. I would especially like to acknowledge my mentors Chien-Fu Chen, Zhiwei Peng, and Jia Huang who have over the past years provided guidance that simplified my learning curve. Another important set of acknowledgements must go to other past and current project collaborators Lyndsey Powell, Dr. Hyejin Kwon, Brendan Meany, Prof. ChuanFu Sun, and Dr. Yong Sun – without them this work would also be less impactful.

Very special acknowledgements goes out to my advisor Prof. YuHuang Wang for his commitment, time, and unwavering leadership, which created new directions in both

my research and personal life as well as my co-advisor Prof. Cheng Lee for all the unmeasurable wisdom and insights.

Finally, I would like to thank the University of Maryland, numerous faculty members that served as my advisors or lecturers, my committee members – Prof. Sang Bok Lee, Prof. Zhihong Nie, Prof. Min Ouyang, along with my two advisors – for this wonderful graduate (and undergraduate) experience and opportunity.

As my graduate career approaches its end, another chapter will open, but the selfless contributions of everyone will remain dear to me.

-AN

Table of Contents

1. Introduction

1.1. Brief Overview and Properties of Carbon Nanotubes

Since the discovery of carbon nanotubes (CNTs) by Iijima in 1991,[1] it has been demonstrated that CNTs exhibit exceptional optical (NIR-II fluorescence),[2,3] electrical (high mobility),[4,5] and mechanical (tensile strength) properties.[6,7] As a result, these materials have been proposed as futuristic biomarkers,[8,9] biological[10,11] and molecular sensors,[12,13] next-generation integrated circuits,[14] and conductive wires.[15] (**Figure 1-1**) These exceptional properties are due to their sp^2 carbon cylindrical lattice, 1-D quantum confinement, high aspect ratio, and structural geometry.[16]

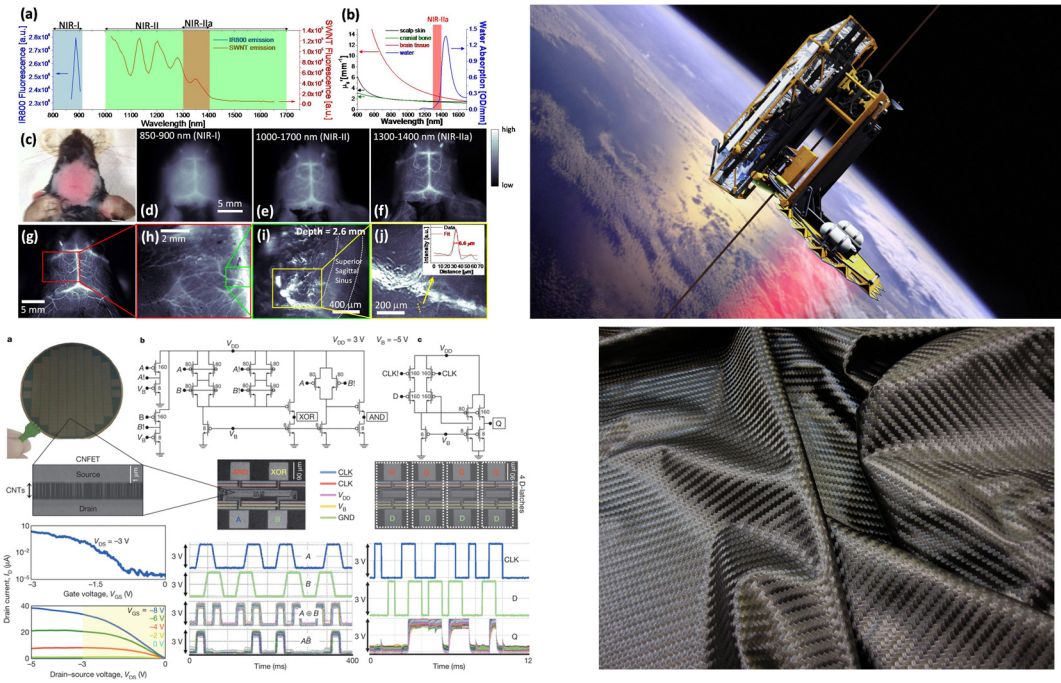

Figure 1-1. Applications of carbon nanotubes.[8,14,15,17]

Depending on the growth conditions, carbon nanotubes can vary in diameter and wrapping angle as well as the number of concentric walls, which result in an ensemble of different properties.[4,18] Each single-walled carbon nanotube (SWCNT) can be defined using two indices (n,m) where n and m are positive integers pertaining to the axis from

the carbon nanotube is wrapped up.[19] (**Figure 1-2**a-d) A CNT exhibits semiconducting properties when (n-m) mod 3 ≠ 0 and exhibits metallic properties when (n-m) mod 3 = 0. As such, 2/3 of SWCNT chiralities are semiconducting and 1/3 are metallic.[20] Specifically, semiconducting CNTs exhibit near-infrared (NIR) fluorescence and exceptionally high mobilities (79000 $cm^2V^{-1}s^{-1}$) compared with conventional semiconductors[5] like silicon (1000 $cm^2V^{-1}s^{-1}$) (Figure 1-2e) and metallic CNTs having three orders of magnitude higher charge capacity than that of standard conductors such as copper (10^9 Am^{-2}).[4] (Figure 1-2f)

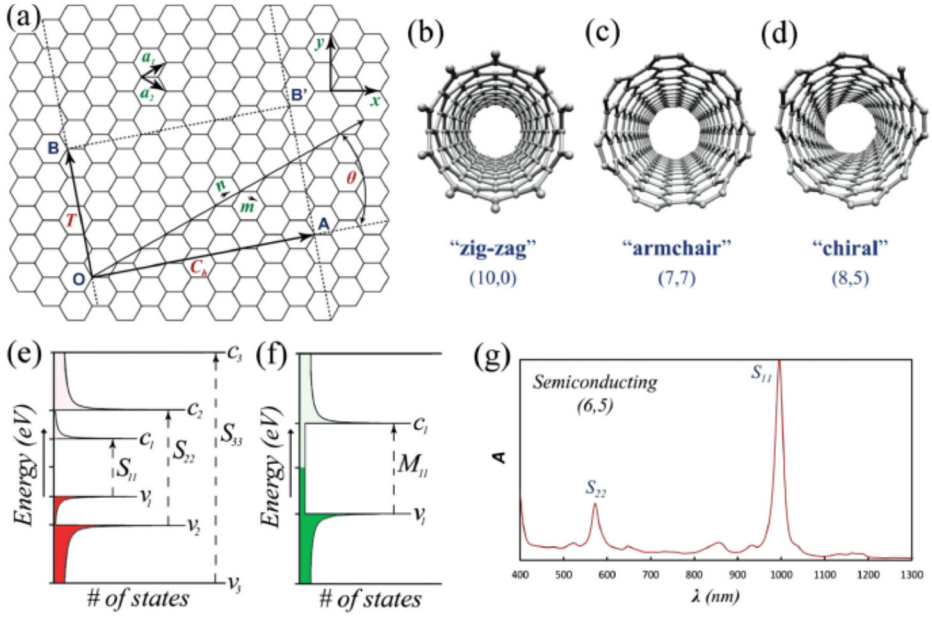

Figure 1-2. Carbon nanotube chirality and electronic type.[21]

The electronic properties of multi-walled carbon nanotubes (MWCNTs), which comprise of multiple concentric walls of CNTs, are also determined by the chiral indices of each wall, but are dominated by metallic chiralities.[22] If any of the walls of the MWCNT are of a metallic chirality, the entire nanotube is metallic due to each wall being able to act as a parallel resistor within a circuit configuration as shown by an example in **Figure 1-3** for a double-walled carbon nanotube (DWCNT).[23] As such, MWCNTs containing numerous

walls are almost all metallic due to an increasing probability that any one wall within the structure is metallic ($P = 1-(2/3)^{\wedge W}$).

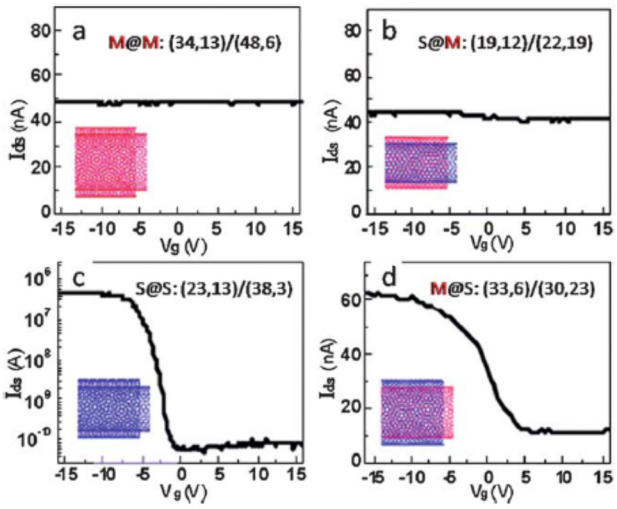

Figure 1-3. Electronic type combinations of DWCNTs.[23]

1.2. Challenges of Carbon Nanotubes

1.2.1. Bundling and Nonspecific Interactions

The exceptional properties of CNTs that arise due to their unique geometric and molecular structure has also resulted in some critical challenges. Due to their sp^2 carbon lattice, carbon nanotubes, much like other carbon nanomaterials, have high affinity towards similar individual structures due to strong π-π stacking interactions that result in the aggregation of individual CNTs into 'bundles'.[24] This bundling effect has most commonly been addressed through dispersing by sonication of bundles in a surfactant solution.[25,26] Although there is debate on what specific morphology surfactants take while encapsulated around the CNTs,[27] it is agreed that the surfactant serves as a polar molecule to reduce interstructural interactions within aqueous solutions.[25] While surfactants have enabled the utilization of individually dispersed CNTs in solutions,

generally for desired applications, surfactants impede and decrease the properties and performance of CNTs.[28,29]

Similar to bundling, CNTs due to their sp^2 graphitic structure also are known to have strong affinity towards organic molecules[30,31] and are highly susceptible to environmental doping[32-34] and nonspecific interactions[32] that may greatly affect their properties (**Figure 1-4**), making the handling and processing of CNTs for applications challenging.[32,35]

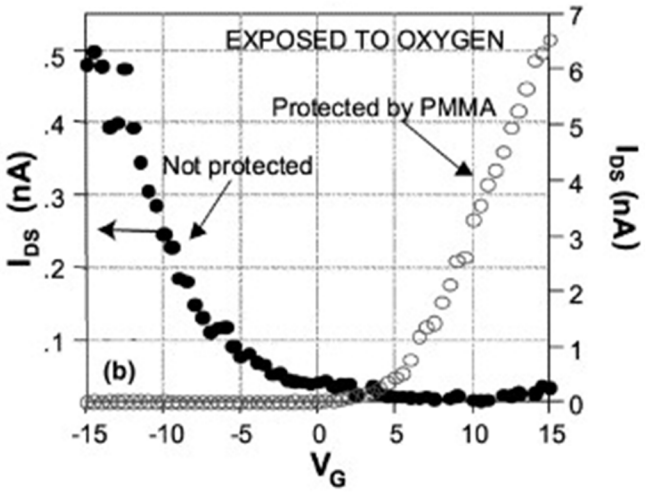

Figure 1-4. Effect of a CNT transistor affected by oxygen doping.[34]

1.2.2. Mixed Electronic Types

The electrical properties of semiconducting and metallic CNTs are exceptional, respectively. However, to effectively incorporate carbon nanotubes to electronic applications, these two electronic types must be sorted to prevent shorting of transistors for the semiconducting applications (**Figure 1-5**) and dampened conduction for metallic applications.[36,37] Methods that preferentially grow CNTs have been established, but the electronic type purity greatly falls short.[38,39] Techniques have been developed to sort carbon nanotubes in solution using techniques including density gradient

ultracentrifugation,[40,41] size-exclusion chromatography,[42,43] and DNA-based separations[44,45] allowing for higher purities, but are limited to SWCNT structures and nevertheless fall short of purity requirements for realistic applications.[14]

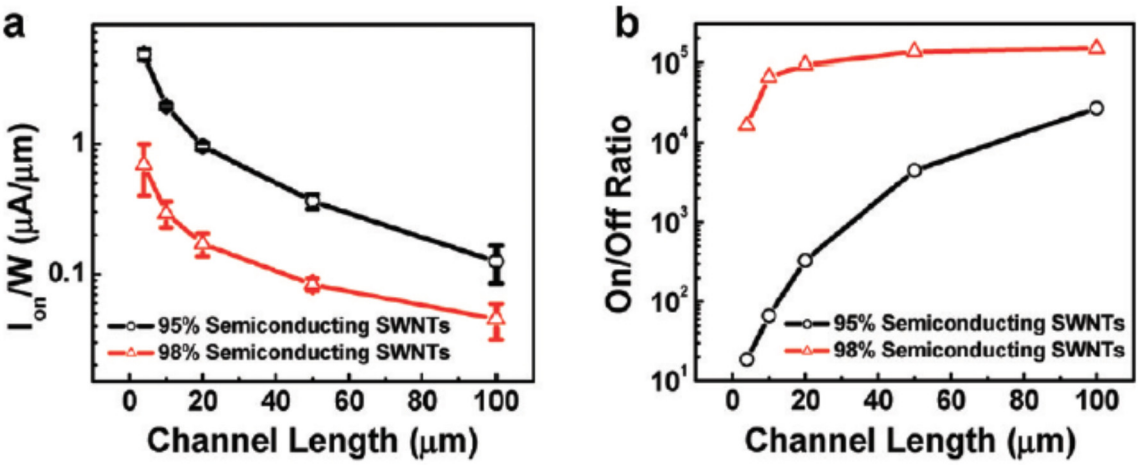

Figure 1-5. The effect of transistor properties (on-current and on/off ratio) as a functional of semiconducting purity.[36]

1.2.3. Covalent Functionalization

Along with the unique and outstanding properties of CNTs, another advantageous feature involves their sp^2 cylindrical carbon surface which can be chemically tailored through well-known covalent[46-48] and noncovalent functionalization strategies[49,50] that have been developed in organic chemistry with aromatic carbon structures. By functionalizing the CNT surface with terminal groups that possess desired properties or features, additional beneficial properties such as solubility[51,52] and molecular affinity for sensing[31] can be achieved with CNTs that would otherwise not be possible using pristine (non-functionalized) CNTs.

Although additional benefits can be achieved through functionalization of carbon nanotubes, almost all instances of functionalization to SWCNT applications were noncovalent.[53-55] This is result of electronic scattering that occurs at the sp^3 defect sites that break the 1-D geometry and greatly decreases transport (**Figure 1-6**).[56]

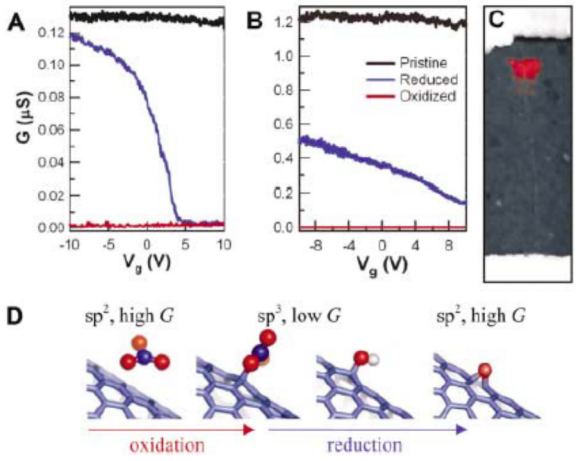

Figure 1-6. Effect of covalent functionalization on electron transport.[56]

1.3. Outer Wall-Selective Functionalized Double-Walled Carbon Nanotubes (Tube^2)

1.3.1. Preparation of Tube^2

The preparation of DWCNTs, which are the Tube^2 precursor, follow a multi-step procedure starting from growth typically through chemical vapor deposition.[57,58] After the growth, tubes are freed from the substrate, placed in water and sonicated within surfactant to debundle the tubes, which would otherwise have strong π-π interactions with each other. Once dispersed in aqueous media, density gradient ultracentrifugation is used to generate a gradient of buoyant density, which allows the isolation of DWCNTs through separation by number of walls (**Figure 1-7**).[59] Density gradient

ultracentrifugation can be further extended to isolate DWCNTs by their outer-wall chirality, which if done correctly can greatly enrich the semiconducting yield of a DWCNT population.[60]

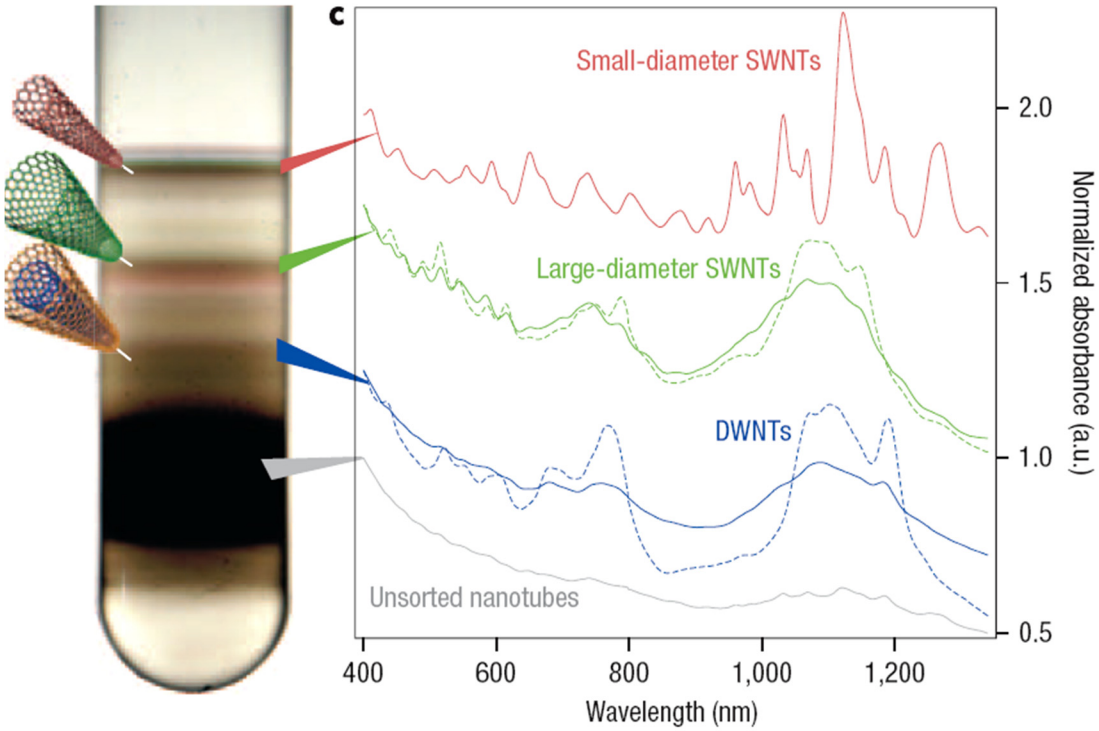

Figure 1-7. Density gradient ultracentrifugation of carbon nanotubes.[59]

With the following preparations, micron long surfactant-dispersed DWCNTs in water can be prepared and used for FET device fabrication.[13,35] However, a key limitation of DWCNT preparation is that established separation techniques are only capable of sorting based on the electronic properties of the outer wall allowing metallic inner walls to dominate structural properties.[35,60] Utilization of metallic DWCNTs (*m*-DWCNTs) instead of semiconducting DWCNTs (*s*-DWCNTs) will result in low transconductances, shorting of the device, reduced performance, high device-to-device variations, and poor yield for semiconductor applications.[35]

Outer-wall selective functionalization, in which only the outer-most wall of the CNT structure is functionalized, is possible due to the structural features of DWCNTs that include the submonolayer (0.36 nm) interwall separation[61] and benzene sized pores that prevents endohedral functionalization through a size-exclusion mechanism that prevent the permeation of functionalization reagent to the inner walls.[62] Various outer-wall selective chemistries have been developed for the creation of Tube^2 with different surface properties.[62,63]

1.3.2. Decoupled Properties of Tube^2

While covalent functionalization of SWCNTs resulted in the loss of their electronic properties, it was found that covalent functionalization of MWCNTs allow overall retention of CNT properties including conductance if the functionalization is outer wall-selective.[48] This has enabled functionalized MWCNTs (*f*-MWCNTs) to be developed for composite materials[64] and chemiresistor sensor arrays,[48] which would not have been possible without the covalent functionalization due to the need for high functional density and robust groups. However, MWCNTs owing to their many walls are likely to be metallic, limiting *f*-MWCNTs to non-semiconductor applications.

DWCNTs are a unique subset of MWCNTs where the number of total walls are two. Structurally, they can be seen as two concentric SWCNTs, one nested within the other, although they can exhibit interesting coupling with each other.[65] As reported in literature, exclusive functionalization to the outer wall preserves the properties of the inner walls and removes the optical (**Figure 1-8**) and electrical (**Figure 1-9**) contributions[62] from the outer wall as if the functionalized outer wall was decoupled with the rest of the structure.[62,63]

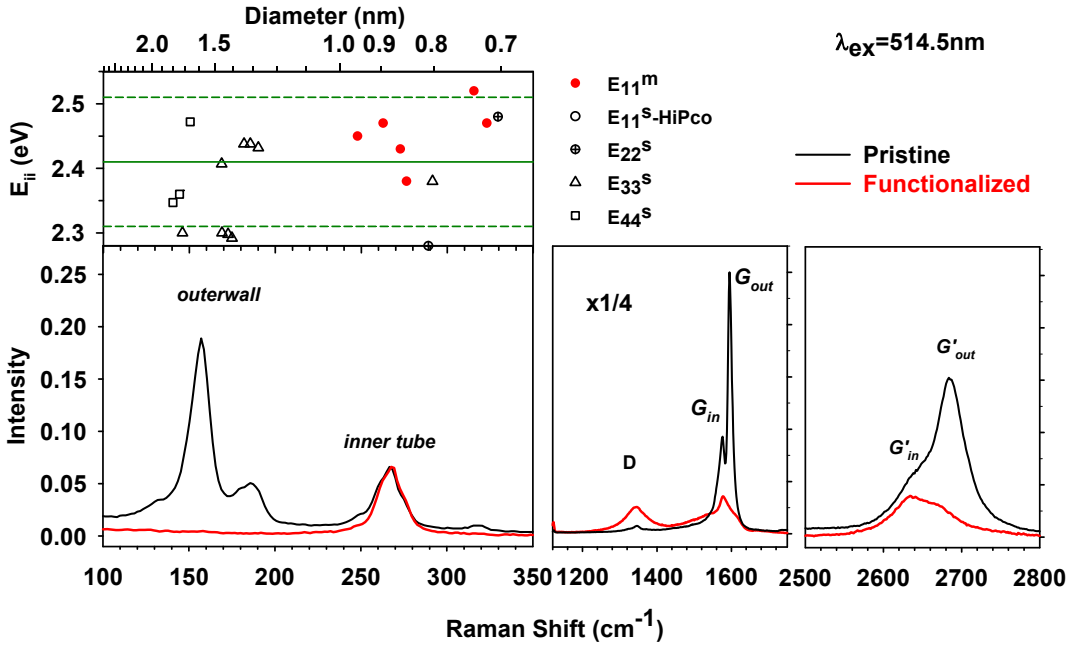

Figure 1-8. Retention of inner-tube optical properties in outer-wall selective covalent functionalization of DWCNTs.[62]

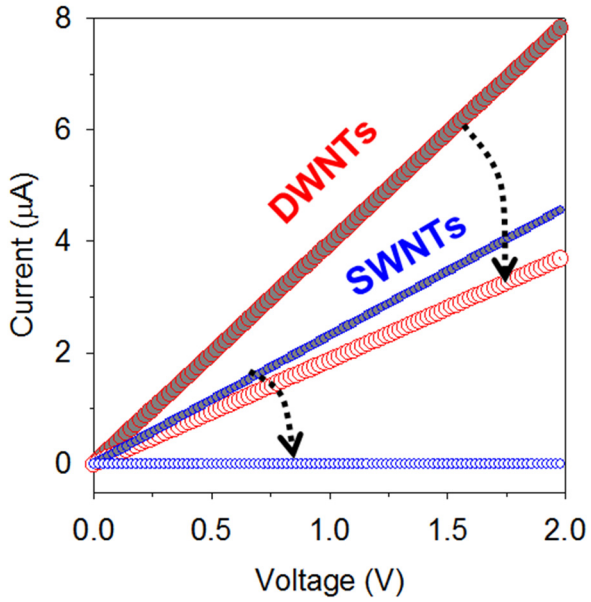

Figure 1-9. Retention of conductivity in outer-wall selective covalent functionalization of a DWCNT thin film.[62]

Furthermore, this Tube^2 structure has been applied to attain desired features such as blocking environmental doping through steric and electronic hindrance[13] and enhancing solubility by attaching polar carboxylic acid groups to address the fundamental challenge of carbon nanotube bundling (**Figure 1-10**).[52] By modulating the functional group of Tube^2 various functional nanostructures can be developed such as for molecular sensing.[13,35]

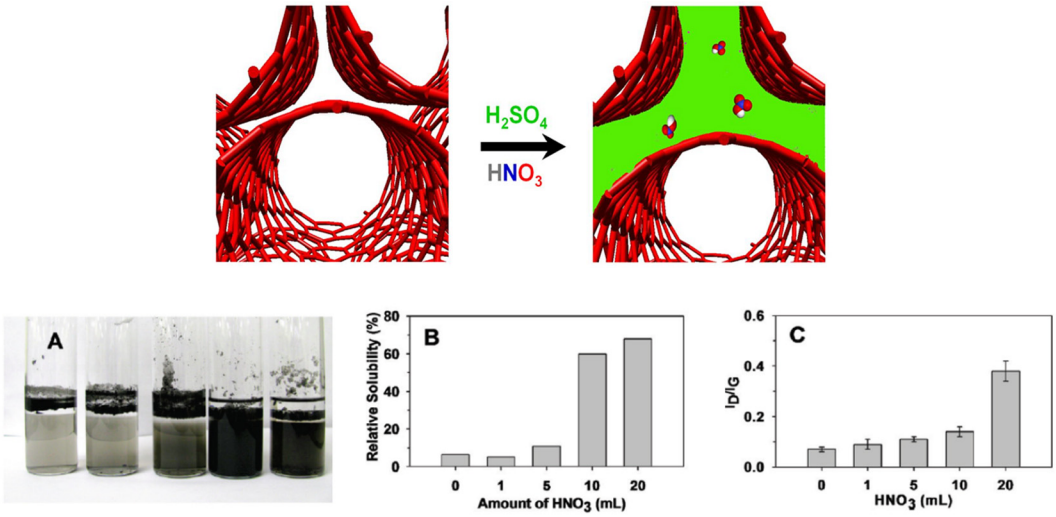

Figure 1-10. Enhanced solubility of Tube^2 structures with increased outer wall selective functional degree.[52]

1.4. Carbon Nanotube Field-Effect Transistors

1.4.1. History and Motivation of FETs

A field-effect transistor (FET) is an extension of a two-terminal resistor with an added gate terminal that can be used to modulate a semiconductor's conductance through capacitance-based coupling.[66] By controlling the electric potential applied to the gate, a FET can tuned to a higher operational current ON-state by enhancing the conductance of

a semiconductor or an insulating OFF-state. This simple feature has been in the inspiration behind the modern electronics industry.[14,67-69]

The technological transformation within the past half-decade that brings us to the current-day digital macrocosm is in great part due to the scalability of FETs on integrated circuits (ICs), which until recent years has been well predicted by Moore's Law.[70] Moore's Law has been sustained primarily by the improvement of spatial patterning technologies that have reduced transistor size and improved transistor packing.[71] In recent years, fundamental limitations of spatial patterning has led to recent drop-offs in Moore's Law.[72] Consequently, the utilization of next-generation materials with better electronic properties than silicon, such as CNTs[5,14,73] and InGaAs,[74] are being considered as the future for electronic performance advancement.

Aside from ICs, FETs have also shown promise in electrical sensing through the chemical tailoring of a semiconductor circuit with molecular probes.[10,12,75] The first ion-selective field-effect transistor (ISFET) sensor was developed in 1975 by Janata demonstrating that bound charged analytes, resultant from affinity towards attached probes, in proximity of a semiconductor can modulate the conductance of the FET much like the use of a gate, providing a measurable parameter in conductance change to detect charged molecular targets.[76] Owing to their simple, real-time, label-free sensing mechanism of FET-based sensing and the ability to fabricate FETs in small size scales, FETs have been considered for cost-effective, on-site sensors.[75,77,78] For similar reasons as with ICs, CNTs are attractive materials for FET sensors due to their extraordinary mobility and ability to be modified through functionalization.[10,78] In fact many CNT FET based sensors have taken advantage of the high mobility and single point covalent

functionalization on SWCNTs to develop ultrasensitive devices capable of detecting confirmation changes within a single molecule for molecular dynamics studies (**Figure 1-11**).[10,79]

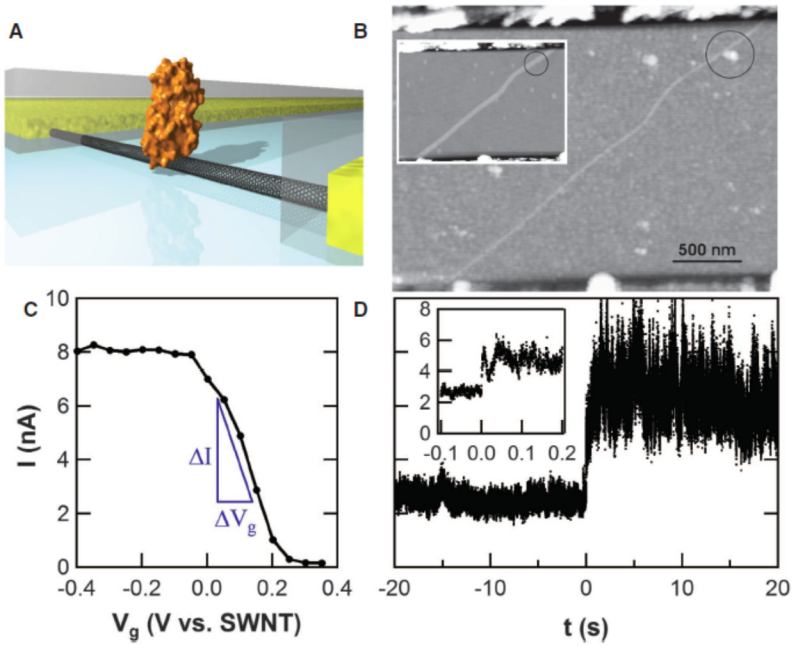

Figure 1-11. Probing single protein conformation changes using a CNT FET.[10]

1.4.2. Carbon Nanotube Thin Film Transistors

To extend these promising CNT FET findings to realistic sensing platforms, common issues associated with CNT, such as their scalability, reproducibility, and most importantly specificity, must be addressed.[13,35,53,80-83] To compensate for the statistical variation of CNT electronic type, length, and mobility, CNT FETs can be prepared as thin film transistors (TFTs) in which the electric circuit is a percolated network of CNTs in the form of a typical submonolayer thin film. CNT TFTs have shown advantages in reproducibility, simplicity of fabrication, high fabrication yield, scalability, and higher

operational current outputs than their single nanotube counterparts with only marginal decreases in their mobility with high aligned films (**Figure 1-12**).[81,83]

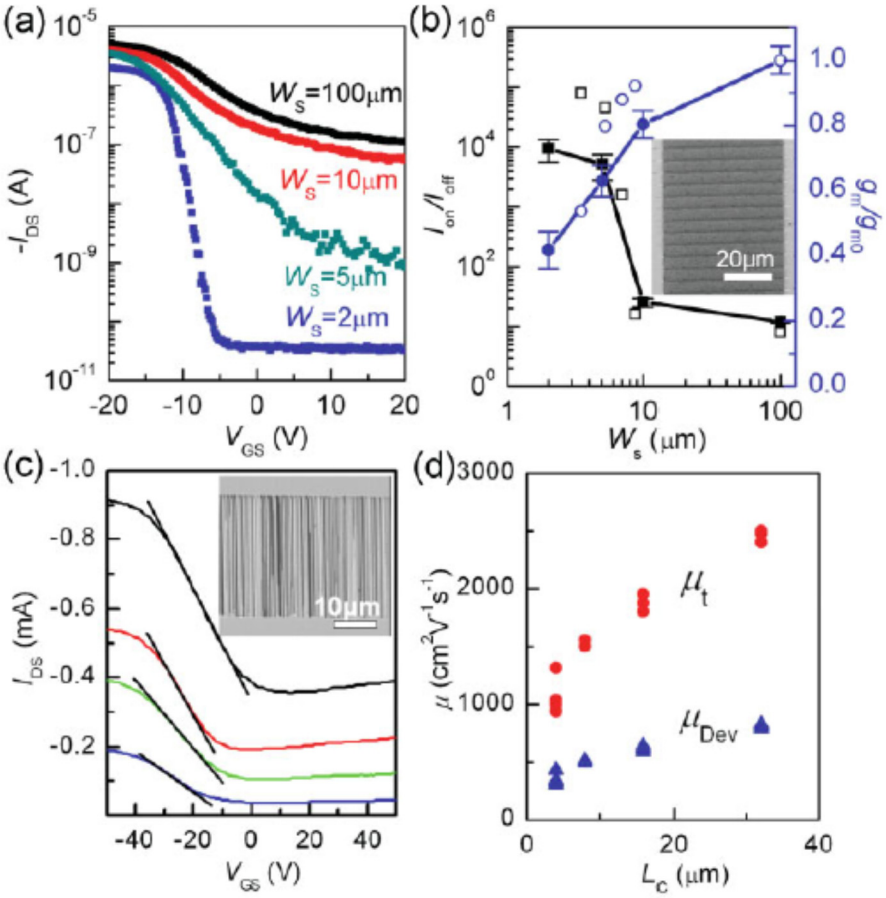

Figure 1-12. Carbon nanotube thin film transistors.[81]

1.4.3. Tube^2 TFT Sensors

The ability to pack high densities of molecular probes on the CNT to enhance specificity remains as one critical challenge not addressed by the TFT platform.[53] Previously demonstrated CNT FETs and TFTs have used point covalent functionalization[10,84] or noncovalent functionalization[49,53] for attachment of molecular probes due to loss in electrical properties upon significant covalent functionalization. However, these techniques come at the sacrifice of low molecular specificity because of low probe

coverage. Furthermore, point functionalization limits the dynamic range while noncovalent techniques lack long term stability for robust applications.[48]

To address the goal of CNT sensor specificity that requires high covalent functional densities, Tube^2 arises an ideal system. Tube^2 offers a CNT-based structure that is compatible with covalent functionalization without the loss of electrical properties[13,62] while having a substantial semiconducting subpopulation.[13,35] As such, combination of Tube^2 with a TFT configuration provides a potentially promising direction for electrical sensing innovation.

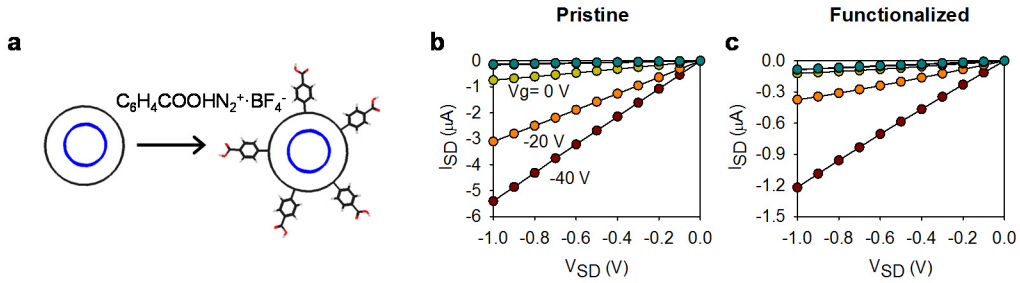

Figure 1-13. Gate-dependent transport properties of non-functionalized and outer-wall selectively functionalized DWCNTs.[13]

1.5. Thesis Topics

The following thesis will entail research that describes the unique electrical features of Tube^2 TFTs, how previous roadblocks related to Tube^2 TFT preparation can be overcome, and the sensing mechanism of Tube^2 TFT sensing. Projects involving the enrichment of semiconducting pathways, demonstration of a Tube^2 TFT small molecule sensor, and development of a non-gated Tube^2 TFT oligonucleotide sensor will be presented. Additionally, we will show a technique that enables creation of CNT pathways with electronic type specificity that occurs because of the unique structural and

electronical features of Tube^2 and the creation of a 2-D carbon nanostructure with similar electrical properties as Tube^2 thin film.

It is noted that Chapters 2 and 3 have been adapted from published articles[13,35] and Chapters 4-6 from submitted articles

2. Selective Breakdown of Metallic Pathways in Double-Walled Carbon Nanotube Networks

(This chapter is adapted from Selective Breakdown of Metallic Pathways in Double-Walled Carbon Nanotube Networks[35] by Ng, A. L.; Sun, Y.; Powell, L.; Sun, C. F.; Chen, C. F.; Lee, C. S.; Wang, Y. Ng, A. L. conceived the electrical breakdown technique and fabrication procedure for DWCNT TFTs and contributed to the fabrication of DWCNT TFTs, electrical characterization, and wrote the manuscript.)

2.1. Introduction

A double-walled carbon nanotube (DWCNT) is comprised of two nested single-walled carbon nanotubes (SWCNTs) that display intricate and interesting electronic properties.[61] This emerging class of carbon nanostructures exhibit unique electrical,[13,23] mechanical,[85,86] and optical properties.[59,87,88] Recent progress by us[13,52,62] and Martel *et al.*[63] has further demonstrated that outer wall-selective covalent functionalization of DWCNTs produces a new structure with outer wall protection and SWCNT-like electrical properties stemming from the protected inner tube. Desired surface properties, such as solubility[52] and reactivity of terminal groups for sensing,[13] can be obtained with DWCNTs by judicious selection of functional groups. This ability to tailor surface properties cannot be obtained with SWCNTs due to defect-induced electron scattering,[56] which transforms SWCNTs into insulators even at relatively low degrees of functionalization.[62] Covalent functionalization of DWCNTs provides an unprecedented platform to attach robust functional groups while maintaining the exceptional electronic properties of the inner tube for applications such as high performance sensors with simultaneous sensitivity and selectivity.[13]

Depending on the nanotube diameter and chiral angle, both the inner and outer walls of a DWCNT can be independently semiconducting or metallic. The semiconducting tubes can have hole mobilities exceeding 70,000 $cm^2V^{-1}s^{-1}$ while the metallic ones may attain current carrying capacities 1000 times greater than that of copper.[5,89] Due to the unique combination of extremely high carrier mobility, one-dimensional structure, and surface protection, DWCNTs can become ideal building blocks for high performance semiconductor field-effect transistors applications such as logic gates, p-n diodes, and single molecule sensors.[10,12,83,90,91]

A major issue that impedes the advance in DWCNT electronics is associated with the structural complexity of DWCNTs.[85,87] A DWCNT possessing a metallic tube in either the inner or outer wall will primarily display metallic electronic properties overall regardless of the other wall. While both semiconducting and metallic DWCNTs are intriguing for a variety of applications, the metallic components within semiconductor devices would inhibit efforts to turn off a transistor and contribute to potential electrical shorting of the circuit. High semiconducting purity is essential for exceptional electronic performance such as high ON-state conductance and ON/OFF ratios.[38,92] The benefits of sorting metallic from semiconducting carbon nanotubes within a mixed CNT array or solution[42,93] have been demonstrated with SWCNTs, for instance, for the development of the first carbon nanotube computer[14] and noncovalently modified electrical sensors.[31,92] Previous studies by Hersam *et al.*, Huh *et al.*, and us have shown the possibility to sort DWCNTs by diameter based on differences in buoyant density,[59,94] chemical reactivity,[95] or even outer wall electronic properties;[60] however, it is not yet possible to eliminate the

electrical contribution from metallic inner tubes. Overcoming this challenge is essential in order to harness the potential of DWCNTs for high performance electronics.

First demonstrated by Collins *et al.*, electrical breakdown is a technique used to induce wall-by-wall destruction within an individual multi-walled carbon nanotube by applying a high voltage bias resulting in Joule heating.[96] Later studies by Rogers *et al.*[81,97], Ohno *et al.*[83], and Maruyama *et al.*[98] applied the technique towards SWCNT networks to preferentially destroy metallic networks while the semiconducting tubes were turned off. This technique has shown significant promise in obtaining enriched semiconducting SWCNT networks with 99.99% purity and could be used in the fabrication of CNT computers where extremely high purity is essential.[14]

Here we demonstrate that metallic DWCNTs, both inner and outer walls, can be selectively eliminated by electrical breakdown (**Figure 2-1**) to simultaneously achieve high ON-state conductance and over two orders of magnitude improvement in ON/OFF ratio within a DWCNT network. Compared with SWCNTs, the challenge of electrical breakdown of DWCNT networks lies in the complex structural composition including small bandgap and large diameter outer wall tubes,[97] low semiconductor composition, and four possible combinations of electronic type stemming from both the inner and outer wall.[23] These factors result in undesired destruction of semiconducting channels during electrical breakdown due to the inability to completely turn off the channel and thermal cross-talk from interconnected metallic channels. By monitoring the electrical breakdown *in situ*, metallic percolated networks were selectively destroyed using breakdown voltage thresholds identified for preserving semiconducting DWCNTs. The intact semiconducting

DWCNTs retained both high ON/OFF ratios and high ON-state conductance even after covalent functionalization.

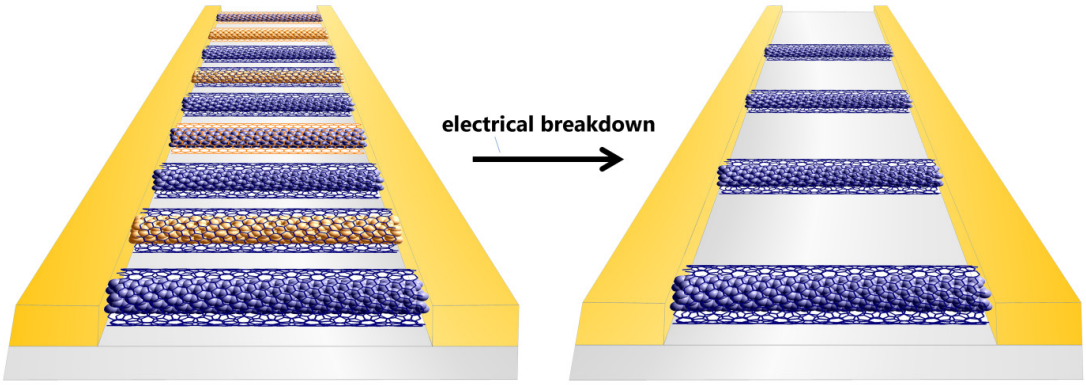

Figure 2-1. Schematic of electrical breakdown of double-walled carbon nanotubes. Blue cylinders represent semiconducting tube chiralities, and golden cylinders represent metallic tube chiralities.

2.2. Results and Discussion

Randomly aligned DWCNT thin film transistors (TFTs) were fabricated using procedures outlined in **Figure 2-2**. Using a modified bilayer photolithography technique,[99] DWCNT TFTs were fabricated in a three-step procedure involving 1) electrode deposition, 2) fabrication of TFT arrays, and 3) passivation of electrodes using the photomask patterns. Bilayer photolithography involved the use of an intermediate sacrificial layer of polymethylgluturimide (PMGI) followed by a standard layer of photoresist. The use of this sacrificial layer is particularly important for the complete removal of photoresist from DWCNT TFTs after photolithography steps, which would result in high patterning resolution. The poor resolution arises from the aromatic structure of DWCNT TFTs, which adhere strongly to photoresist via π-π stacking. Due to its non-aromatic structure, PMGI

can be cleanly removed using standard resist remover, such as Remover PG, ensuring good fabrication resolution.[99] Fabrication of TFT arrays involved electrical separation of adjacent transistors using oxygen plasma etching to prevent electrical cross-talk. The channel regions of the electrodes were then passivated with a layer of SiO_2 to protect their integrity when exposed to aqueous solutions for procedures such as covalent functionalization.

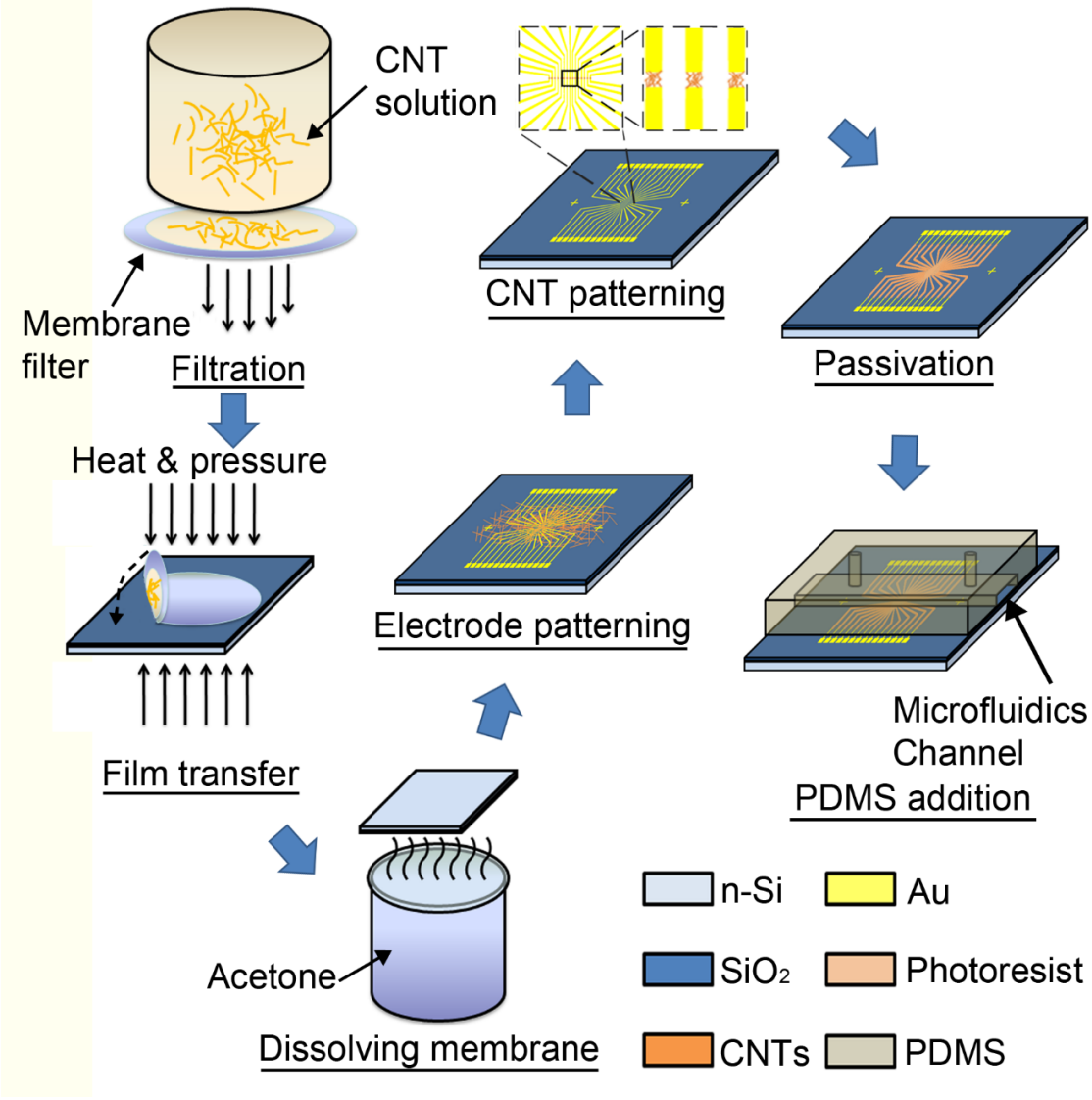

Figure 2-2. Schematic fabrication procedure for a DWCNT TFT.

The performance of the TFTs was evaluated by taking current-voltage (I_{SD}-V_{SD}) and transfer characteristic (I_{SD}-V_g) curves to determine the ON-state conductance and the ON/OFF ratio. Before electrical breakdown, the TFTs showed high ON-state conductance (0.5-5.0 μS), but low-to-moderate ON/OFF ratios (20-500), which was attributed to significant metallic populations despite the use of outer wall purified DWCNTs to make the networks.

When a large source-drain voltage was applied, metallic percolated pathways were selectively heated and destroyed since metallic DWCNTs possess higher electrical non-gated conductance than their semiconducting counterparts. A source-drain voltage of -100 V was applied in cycles of 28 seconds until no appreciable gains in ON/OFF ratio were observed. Electrical characterization was performed *in situ* by monitoring the source-drain current during the breakdown. After each cycle, current-voltage and transfer characteristic curves were taken to determine the electrical performance. **Figure 2-3** shows stepwise decay of the OFF-state conductance at the breakdown voltage while the electrical breakdown cycling was performed. Each abrupt decrease in the source-drain current is indicative of an electrical breakdown event resultant from the destruction of a metallic DWCNT network. The cycling was halted upon no additional stepwise losses in conductance. The OFF-state conductance after electrical breakdown was typically in the range of 10-50 pS.

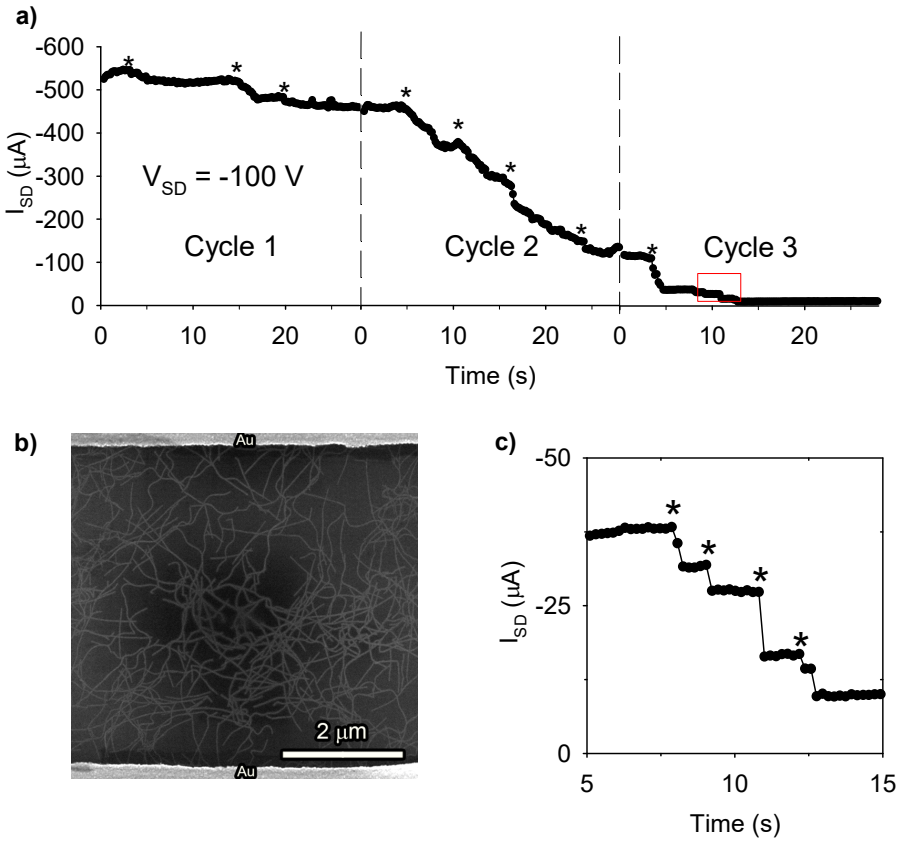

Figure 2-3. *In situ* current versus time measurement during electrical breakdown of a DWCNT TFT thin film at a fixed source-drain voltage (V_{SD} = -100 V) for three cycles. Electrical breakdown events are characterized by sharp decreases in source-drain current (marked by asterisks).

This electrical breakdown procedure produces DWCNT TFTs with ON/OFF ratios as high as 40,700 and concomitant ON-state conductance of approximately 1 μS for 15 μm (length) by 50 μm (width) channels. **Figure 2-4** and **Table 2-1** show the transfer curves and tabulated electrical properties for a sample device. The minimum OFF-state conductance for this device (18 pS) can be attributed to thermally excited carriers at room

temperature and indicates that the metallic tubes are either completely removed or well below the percolation density.

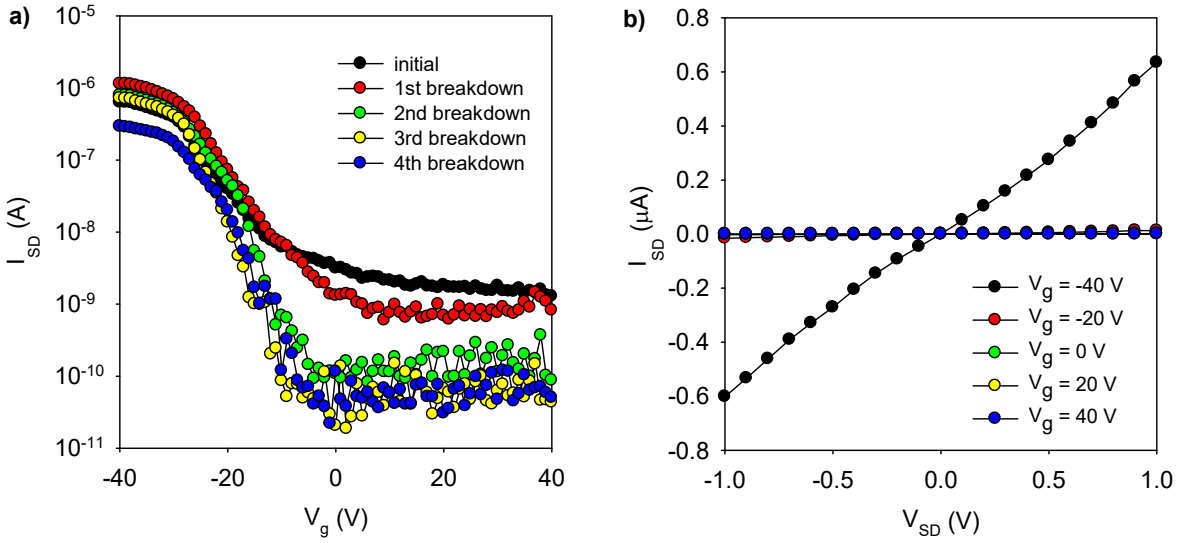

Figure 2-3. Transport properties of a DWCNT TFT after each electrical breakdown event at a fixed source-drain voltage bias (V_{SD} = 1 V) and I-V curve after the third cycle of electrical breakdown.

Table 2-1. Transistor characteristics of a DWCNT TFT after each electrical breakdown cycle.

	Breakdown cycle	**$I_{SD, ON}$ (nA)**	**$I_{SD, ON}$ retention (%)**	**$I_{SD, OFF}$ (nA)**	**$I_{SD, OFF}$ retention (%)**	**ON/OFF ratio**
	Initial	-667	1	-1.28	1	522
Regime 1	1st	-1,210	1.81	-0.596	0.465	2,030
Regime 2	2nd	-830	1.24	-0.082	0.064	10,100

	3rd	-759	1.14	-0.0187	0.0146	40,700
Regime 3	4th	-308	0.46	-0.022	0.0171	14,000

During electrical breakdown cycling, we observed three distinctly different regimes with respect to the ON- and OFF-current (Table 2-1). The first regime, reproducibly displayed approximately a 2-fold increase in ON-current and 2-fold decrease in OFF-current. These changes can be explained by the removal of contaminants such as amorphous carbon along with metallic percolated pathways within the thin film network, which increase the ON-current and decrease the OFF-current, respectively.

The second regime comprises of abrupt decreases in both ON- and OFF-currents, although the OFF-current decreases over 20 times more than the ON-current. This is attributed to the selective destruction of metallic tubes. Moderate decreases of approximately 40% in ON-current may be due to semiconducting percolation pathways that were destroyed in small quantities from the thermal cross-talk between interconnected metallic and semiconducting percolated pathways within the thin film. These observations are consistent with previous works on electrical breakdown with random SWCNT networks.[97]

The third regime is defined by a relatively larger decrease (~60%) in ON-current without any appreciable changes in the OFF-current. In this regime, there are very few metallic percolated pathways remaining in the conduction channel, as evident by the small (10-50 pS) OFF-state conductance, and semiconducting DWCNTs with large diameter outer walls upon prolonged breakdown voltage become more susceptible to breakdown due to their smaller bandgaps.

Compared to SWCNTs, electrical breakdown of DWCNT networks is more challenging due to the complex combination of inner and outer wall types. Furthermore, semiconducting outer walls have smaller bandgaps due to the larger diameters, making it more difficult to differentiate from metallic nanotubes. Both factors can result in unintentional breakdown of semiconducting pathways, as evident by the decrease of ON-state conductance (by 40-75%) within the second and third regimes, due to the inability to completely turn off the channel and prevent thermal cross-talk from interconnected metallic pathways. The ability to eliminate metallic contributions while retaining a high ON-state conductance can be accomplished by cycling up to the second regime.

Unlike SWCNT networks, we found that DWCNT networks do not require gating to achieve the selective breakdown of metallic pathways. No additional selectivity was observed when a gating voltage (as high as 40 V) was applied. This non-gated electrical breakdown behavior is similar to that of previous observations with single MWCNTs by Collins *et al*.[96] We hypothesize that the difference between SWCNTs and DWCNTs originates from lower oxygen doping levels in DWCNTs due to outer wall protection. The lower dopant levels protect the semiconducting DWCNTs from being turned on or reaching the breakdown conductance thresholds even at non-gating conditions. The lack of such protection in SWCNTs exposes the all surface structure to dopants such as oxygen, resulting in substantial residual conductance at non-gating conditions.

Channel length studies show a strong relationship between channel length and breakdown voltage. This channel-length dependence is related to the existence of a power threshold for breakdown. At a fixed voltage, power is inversely related to the resistance and thus the channel length. Longer channel length TFTs have higher resistance and hence

require higher breakdown voltages. We noted that channel lengths of 3 μm could be broken down completely at a source-drain voltage of -15 V, while even a source-drain voltage of -200 V rarely worked for channel lengths larger than 25 μm.

To ensure that the electrical breakdown was not destroying semiconducting DWCNTs, DWCNT TFTs that were electrically broken down to the second regime were then covalently functionalized with 4-carboxylbenzene functional groups using diazonium chemistry (**Figure 2-5**a), which would remove the contributions of outer walls and all exposed inner tubes (if semiconducting outer walls were damaged by electrical breakdown).[13,62] Covalent functionalization of the DWCNT TFT (Figure 2-5b,c) was verified using Raman spectroscopy (Figure 2-5d). Evidence of covalent functionalization includes the disappearance of the outer wall radial breathing mode peak at 100-200 cm^{-1} and the emergence of the D-band (~1300 cm^{-1}). Together, these spectroscopic features support formation of sp^3 defects on the outer wall. Retention of ON-state conductance (Figure 2-5c) and the preservation of the inner wall RBM peak (Figure 2-5d) are jointly strong evidence that the inner walls of semiconducting DWCNTs were protected by the outer walls during the covalent modification. This observation is consistent with our previous results that the functionalization of a DWCNT network of mixed electronic types leads to a decrease in conductance associated with the loss of outer wall electrical properties, but retains the inner wall conductivity.[62] This experiment suggests that the semiconducting DWCNTs within the network, both inner and outer walls, are immune from electrical breakdown through the second regime.

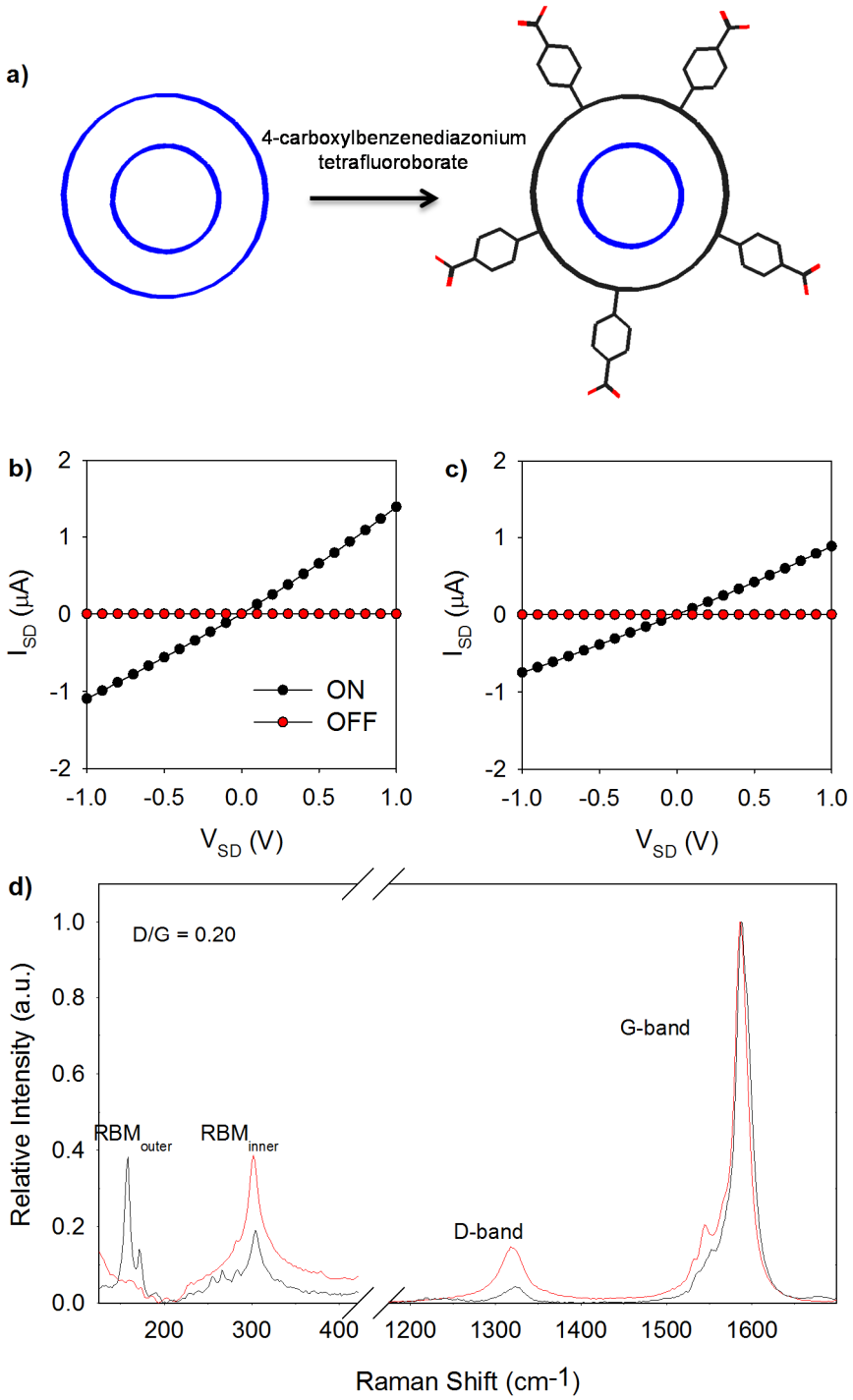

Figure 2-5. Outer-wall selective covalent functionalization of a DWCNT with 4-carboxylbenzene groups shows retention of electrical properties after covalent functionalization.

To further understand the structural features of the DWCNT networks during the three regimes of electrical breakdown, covalent functionalization was used as a probe for intact DWCNTs (**Figure 2-6**). Within the first and second regime both the inner and outer walls from semiconducting DWCNTs are intact, as indicated by the retention of ON-state conductance after functionalization (Figure 2-6b,e). This demonstrates that electrical breakdown can be applied without damaging DWCNT semiconducting network.

In contrast, the third regime shows minimal retention of ON-state conductance upon functionalization indicative of damaged inner or outer walls, or both within semiconducting percolated pathways (Figure 2-6c,g), which corroborates the decrease of ON/OFF ratio in the third regime.

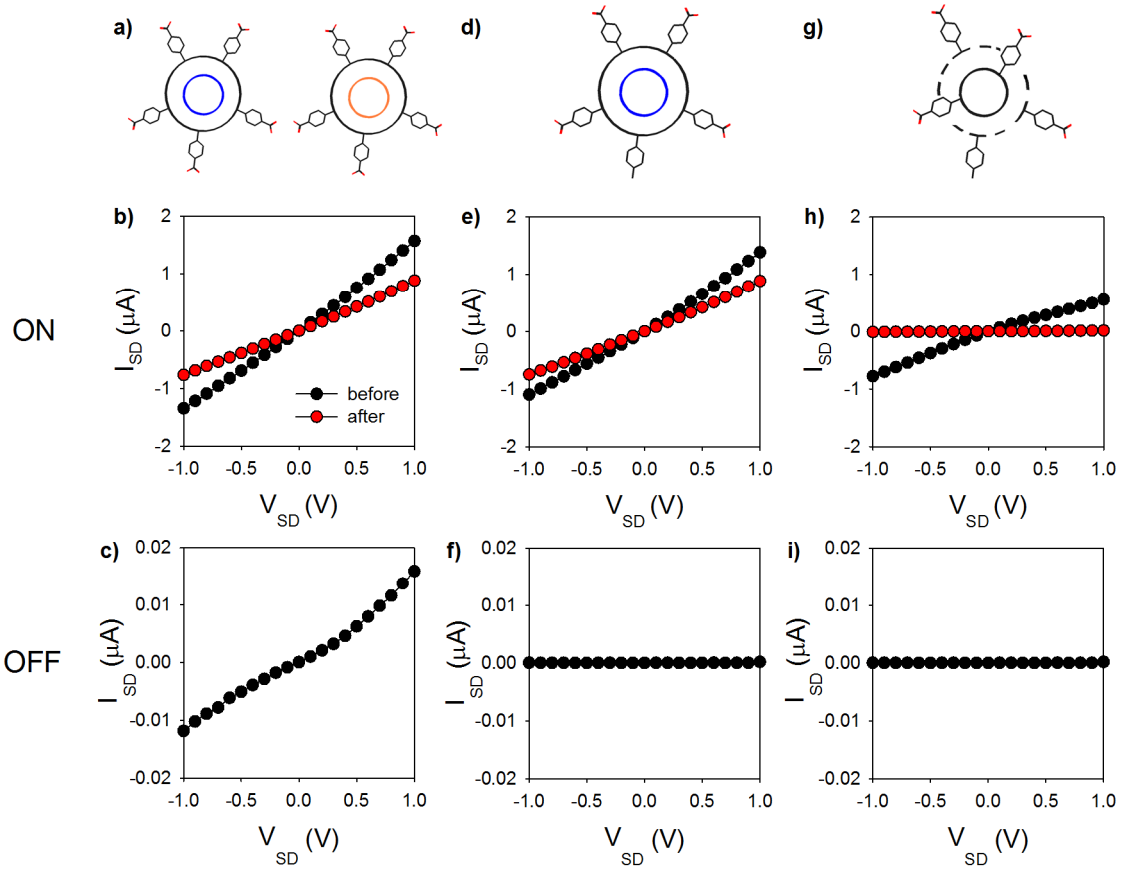

Figure 2-6. Outer wall selective chemistry as a probe for intact DWCNT networks for (a)

first, (d) second, and (g) third regimes. Blue, orange, and black walls represent semiconducting metallic, and insulating tubes chiralities. ON-state (V_g = -40 V) before (black) and after (red) covalent functionalization I-V curves of an electrically broken down DWCNT TFT within the (b) first, (e) second, and (h) third regime. OFF-state (Vg = 40 V) I-V curves for DWCNT conduction channels within the first (c), second (f), and third regime (i) before covalent functionalization.

2.3. Conclusion

We demonstrate high performance Tube^2 TFTs through controlled electrical breakdown of metallic percolated pathways without damaging the inner or outer wall of semiconducting DWCNTs. The selective destruction of metallic percolated pathways significantly increased the ON/OFF ratio, by 360-fold. ON/OFF ratios as high as 40,700 and an ON-state conductance of 600-1000 nS were simultaneously attained. This combination of high ON/OFF ratio and ON-state conductance in DWCNT networks provides an opportunity to create highly stable, robust thin film devices with tailored surface chemistry and excellent electrical properties.

2.4. Experimental Section

Device Fabrication and Bilayer Photolithography: Highly n-doped silicon wafers with a 300 nm thermally grown silicon oxide layer (Silicon Quest International) were used as the back-gated substrates and the gate dielectric respectively. Substrate and DWCNT thin film preparation were prepared using a procedure from previous work.[13] DWCNTs (Unidym DW411UA) possessed average inner and outer wall diameters of 0.86 and 1.61 nm,

respectively and an average length of 900 nm. A randomly aligned thin film network with a DWCNT density of approximately 61 nanotubes per μm^2 was transferred to the substrates. Using bilayer photolithography with PMGI and Shipley 1813 as the sacrificial layer and photoresist respectively, chromium and gold source/drain electrode contacts with a channel length and width of 15 and 50 μm, respectively were patterned. Using a similar patterning procedure with the mask design shown on Figure S1b, bilayer photolithography was again used to fabricate TFT arrays by separating adjacent transistors from the thin film structure through using oxygen plasma etching. The TFT was patterned so that the DWCNTs confined within the source-drain electrodes were protected with bilayer photoresist while the remaining area was exposed. Exposure of the patterned substrates to oxygen plasma at a power of 100 W and a flow rate of 50 sccm for 30 seconds resulted in the complete removal of all DWCNT networks exposed while the DWCNTs within the protected regions remained intact. The electrodes were then passivated by patterning a 125 nm layer of SiO_2 using bilayer photolithography on top of the inner regions of the electrodes.

Characterization: DWCNT percolated networks confined within the source-drain regions were characterized using scanning electron microscope (SEM) for tube densities and fabrication quality.

Electrical Breakdown and Measurements: For the electrical breakdown of DWCNT TFTs, a large negative V_{SD} bias of -100 V was applied to DWCNT TFTs with a conduction channel length of 15 μm for 28 seconds as one cycle. Electrical characterization of I-V and transfer curves (Keithley 4200-SCS) was performed after every cycle.

Covalently Functionalized Networks: To verify that the DWCNT TFTs remained intact after electrical breakdown, electrically broken down TFTs were functionalized with 4-carboxylbenzenediazonium tetrafluoroborate. The reagent was synthesized from 4-aminobenzoic acid (Sigma Aldrich, ≥99%) using a previously described method.[62] The diazonium structure was confirmed by ^{1}H-NMR (Bruker DRX-400) and FTIR (Thermo Nicolet NEXUS 670 with ATR attachment) spectroscopies. For NMR analysis, samples were dissolved in acetonitrile-D3 (99.8%, Cambridge Isotope Laboratories, Inc). Covalent functionalization was achieved by flowing a 1 mM aqueous solution of 4-carboxylbenzenediazonium tetrafluoroborate at a rate of 25 μL/min through microfluidic channels attached to the TFTs for one hour. The residual reactants were then removed by flowing Nanopure^{TM} water through the microfluidic channels for 30 min at the same flow rate. Electrical characterization of the DWCNT TFTs was performed after functionalization and Raman spectroscopy (Horiba Jobin Yvon LabRAM Raman microscope, model ARAMIS) with an excitation line of 633 nm was used to characterize the extent of covalent functionalization.

3. Covalently Functionalized Double-Walled Carbon Nanotubes Combine High Sensitivity and Selectivity in the Electrical Detection of Small Molecules

(This chapter is adapted from Covalently Functionalized Double-Walled Carbon Nanotubes Combine High Sensitivity and Selectivity in the Electrical Detection of Small Molecules[13] by Huang, J.; Ng, A. L.; Piao, Y. M.; Chen, C. F.; Green, A. A.; Sun, C. F.; Hersam, M. C.; Lee, C. S.; Wang, Y. H. Ng, A. L. contributed to the fabrication of CNT transistors, electrical characterization, and manuscript writing.)

3.1. Introduction

One of the major challenges and opportunities in nanoscience lies in developing the ability to utilize the exceptional electrical properties of nanomaterials in complex chemical environments such as solar cells, fuel cells, microprocessors, and sensors. In the context of a sensor application, there is hope that nanomaterials will allow for fabrication of electrical sensors capable of detecting ultralow concentrations of analytes, e.g., explosives (such as TNT, nitroglycerin, cyclotetramethylene-tetranitramine) and biomolecules (such as HIV), with ultrahigh selectivity such that trace interferents will not trigger false positives. Various nanostructures and strategies have been explored for meeting this challenge. Some of the most sensitive sensors are based on graphene and pristine single-walled carbon nanotubes (SWCNTs).[12,31,80,82,84,100-107] In several specific cases some success has also been achieved with non-covalent functionalization of the surface with receptor molecules to overcome non-specific binding.[31,108] However, low long-term stability and incomplete surface coverage of non-covalent coatings remain general concerns for more demanding applications such as *in vivo* studies and those

involving more aggressive chemical reactions. Covalent attachment of receptor molecules to the surface is an effective strategy for improving chemical selectivity. However, the number of functional groups that can be covalently attached to a SWCNT sidewall or graphene surface is extremely limited since covalent modifications quickly destroy their electrical properties.[56]

Here, we demonstrate simultaneous high sensitivity and chemical selectivity in covalently functionalized DWCNT thin film transistors (TFTs) (**Figure 3-1**). A DWCNT consists of two concentric SWCNTs that exhibit complicated but relatively independent electronic properties.[61] Field-effect transistors integrating individual, pristine DWCNTs have been shown to have high on/off ratios ($>10^3$) and exceptional conductivity,[63,109] which are desirable for many electronics applications such as sensors. Advances in synthesis[57,110] and purification of DWCNTs[59,60] have made it possible to fabricate high quality thin film devices. Particularly, recent experiments by us[52,62] and others[63] have shown that the electrical properties of inner tubes can be retained even after heavy functionalization of the outer DWCNT wall by covalent chemistries. Furthermore, changes to the chemical or electrochemical environment at the surface of the outer wall of a DWCNT have been shown to induce electrical changes to the inner-wall of a DWCNT, suggesting the possibility of sensitive chemical detection via charge transport through the well-defined and chemically protected inner-wall.[111,112] In this report, we heavily functionalized the outer wall of the DWCNTs using diazonium chemistry, which readily provides a variety of terminating groups, including -COOH, -OH, $-CH_3$, $-NO_2$.[113,114] Because the inner tubes are hermetically sealed by the functional outer wall, non-specific binding can be significantly reduced. We found that the transduction

performance of the inner tube can be superior to other structures such as embedding SWCNTs in a functional coating or functionalized silicon nanowires, since the functionalized outer wall is only one atom-thick. This double wall structure thus makes it possible to fabricate high performance chemical sensors with tailored surface chemistry to simultaneously achieve ultrahigh sensitivity and selectivity along with long-term stability.

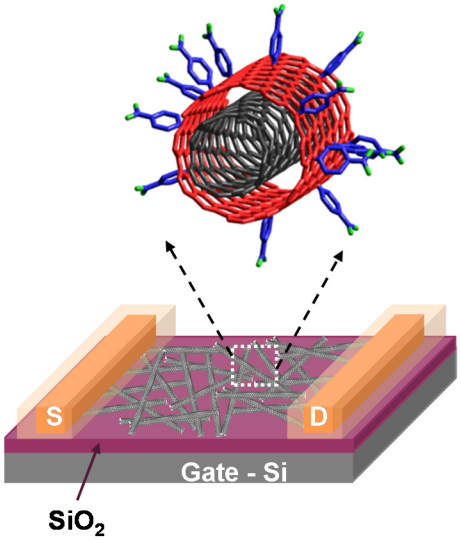

Figure 3-1. Schematic diagram of a Tube^2 TFT platform that combines semiconducting inner tubes as transducer elements and chemically tailored outer walls for improved chemical selectivity.

3.2. Results and Discussion

As a demonstration and proof of concept, we fabricated DWCNT TFTs from high-purity DWCNTs[59] and compared their device performance with SWCNTs and multi-walled carbon nanotubes (MWCNTs). The DWCNT TFT devices were covalently functionalized with $–C_6H_4COOH$ functional groups by reacting with 4-carboxylbenzenediazonium tetrafluoroborate in the dark at room temperature. Successful

covalent functionalization of the outer wall was confirmed by comparative Raman spectroscopy studies of DWCNTs and SWCNTs before and after the functionalization (**Figure 3-2**). After functionalization, the disorder mode (D band) around 1310 cm^{-1} appeared, signifying covalent modification of the nanotube sidewalls. In the functionalized DWCNTs, the radial breathing mode (RBM) of the inner tube (200-400 cm^{-1}) remained intact while that of the outer wall (under 200 cm^{-1}) completely disappeared, unambiguously confirming selective covalent functionalization of the outer wall.

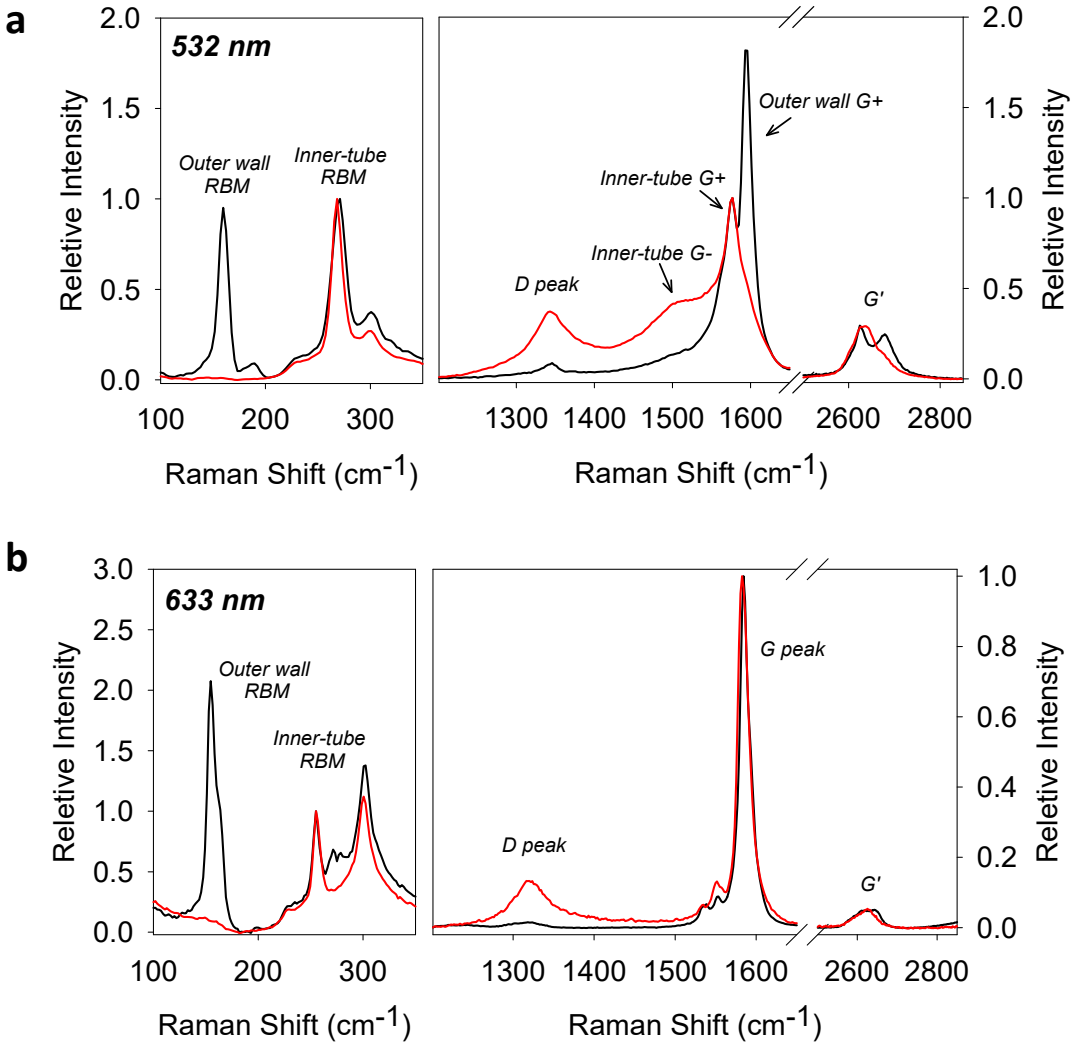

Figure 3-2. Raman spectra of DWCNT thin films before (black line) and after covalent functionalization with $-C_6H_4COOH$ groups (red line) for excitation lines of a) 532 nm and b) 633 nm showing evidence of outer wall selective covalent functionalization.

Figure 3-3 shows the I-V characteristics of the p-type DWCNT TFTs (Figure 3-3a and 3-3b) in comparison with similarly fabricated p-type SWCNT TFTs and MWCNT TFTs before and after covalent surface modification with $-C_6H_4COOH$ functional groups. After heavy covalent functionalization, the SWCNT TFT device lost all of its electrical conductivity and transistor characteristics (Figure 3-3e and 3-3f). In contrast, MWCNTs

did not show a significant decrease in electrical conductivity, but the highly metallic nature of the MWCNTs resulted in very low on/off ratios (~1). These MWCNT TFTs, with and without functionalization, exhibit characteristics of resistors rather than that of transistors as evident by their negligible gate amplification effects (Figure 3-3h and 3-3i); for sensing purposes, it is more desirable to have transistor properties especially a high on/off ratio which allows for gate modulation and amplification of drain current response. For DWCNT TFTs, pristine devices exhibited modest on-current with relatively high on/off ratios. After covalent functionalization, the Tube^2 devices showed 5-10 times lower source-drain current; the source-drain current at V_g = -40 V and V_{SD} = -1 V was reduced from 5.5 μA to 1.2 μA. However, the source-drain current of Tube^2 TFTs was still on the same magnitude of pristine SWCNTs and their transistor characteristics, most importantly, were retained (Figure 3-3b and 3-3c). **Table 3-1** compares the on-current, on/off ratio, and chemical selectivity of SWCNT, DWCNT and MWCNT TFTs before and after covalent functionalization. These results confirm that inner tubes in the covalently functionalized double-wall structure uniquely possess desirable semiconductor characteristics.

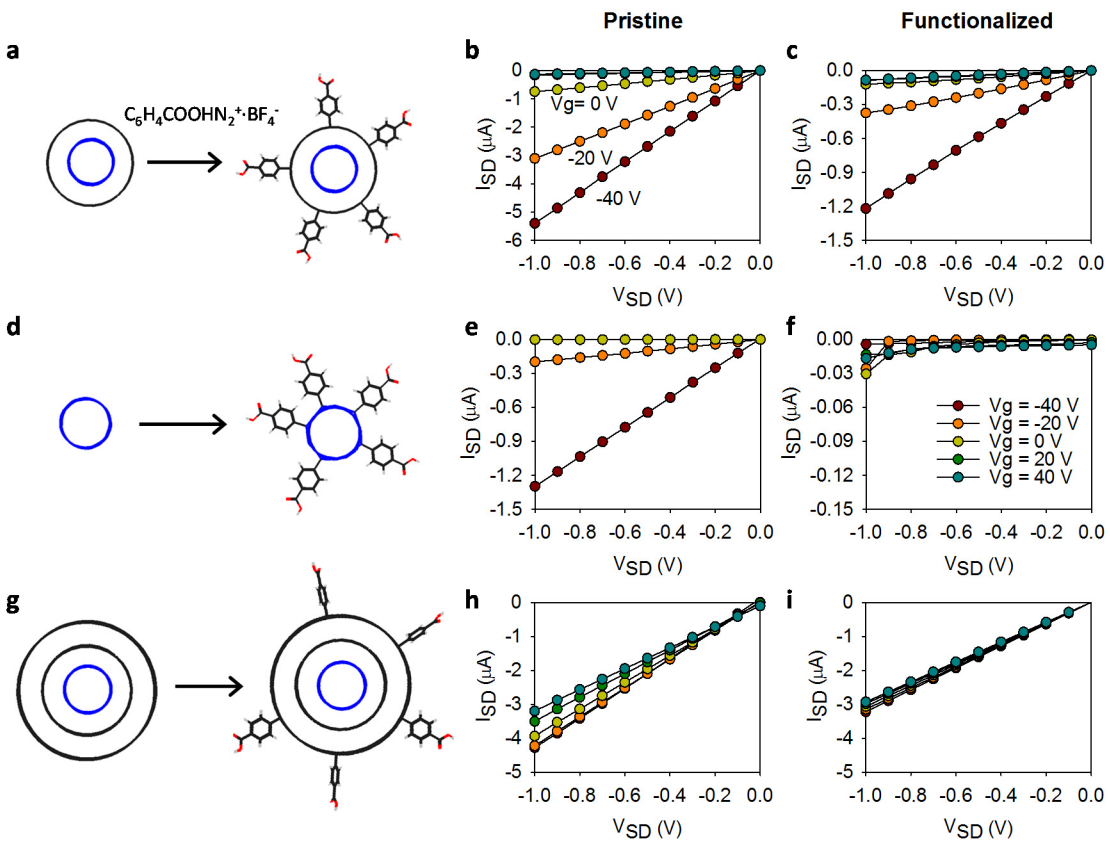

Figure 3-3. Source-drain I-V curves of *f*-DWCNT TFTs show persistent transistor properties in stark contrast to their single-walled and multi-walled counterparts.

Table 3-1. Chemical sensing characteristics of Tube^2 TFTs in comparison towards other pristine and functionalized CNT TFTs.

		On current	On/off ratio	selectivity
SWCNT	**Pristine**	Moderate	High	Low
	Functionalized	Low	N/A	N/A
DWCNT	**Pristine**	High	High	Low
	Functionalized	High	High	High
MWCNT	**Pristine**	High	Low	Low
	Functionalized	High	Low	Low

Upon exposure to analytes, a p-type CNT TFT with a high on/off ratio has an enhanced response when the device is turned on by applying a negative gate voltage. This phenomena arises because semiconducting CNTs are typically more sensitive to analytes than metallic CNTs.[105] When the TFT is turned on by applying a negative gate voltage, the semiconducting CNTs become conductive. When a high positive gate voltage is applied, the TFT is turned off and the semiconducting CNTs are insulating. A high on/off ratio is indicative of a large ratio of semiconducting CNTs to metallic CNTs in the conduction channel. In this scenario, semiconducting CNTs contribute to the majority of the drain current when the CNT TFT is turned on. Those semiconducting CNTs at the "ON" stage are sensitive to analytes due to charge transfer or trapping effects. The gate modulation effect can thus amplify the responsive component of the drain current and increase sensor response. **Figure 3-4** shows the normalized gate-dependent response of a Tube^2 TFT upon exposure to 60 μM NH_3 as a function of gate voltage. At a V_g of -40

V, the TFT was turned on and about 70% current reduction was observed when the device was exposed to NH_3 solution. When the TFT was turned off at a V_g of +40 V, only about 5% current response was observed, illustrating that semiconducting DWCNTs are more responsive to analytes than metallic DWCNTs and the importance of gate amplification effects in a DWCNT TFT sensor.

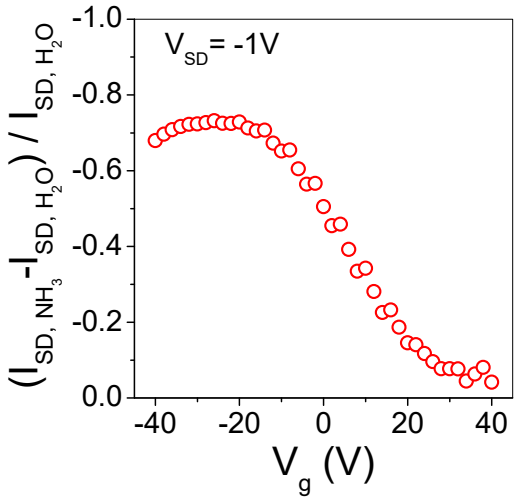

Figure 3-4. Relative response of a Tube^2 TFT upon exposure to 60 μM NH_3 as a function of gate voltage (V_g). Higher relative response was observed at negative V_g when the TFT is turned on. When the device was turned off at positive gate voltage much lower response was observed.

The electrical characteristics of DWCNT TFTs highly depend on the areal density of DWCNTs in the conduction channel, which can be straightforwardly controlled by adjusting the volume and concentration of the DWCNT solution used for filtration. **Figure 3-5** shows the source-drain current and on/off ratio of DWCNT thin-film TFTs as a function of DWCNT areal density. For each areal density, five devices were fabricated

and measured. The DWCNT areal density was calculated by dividing the mass of DWCNTs in the solution by the filtration membrane area.

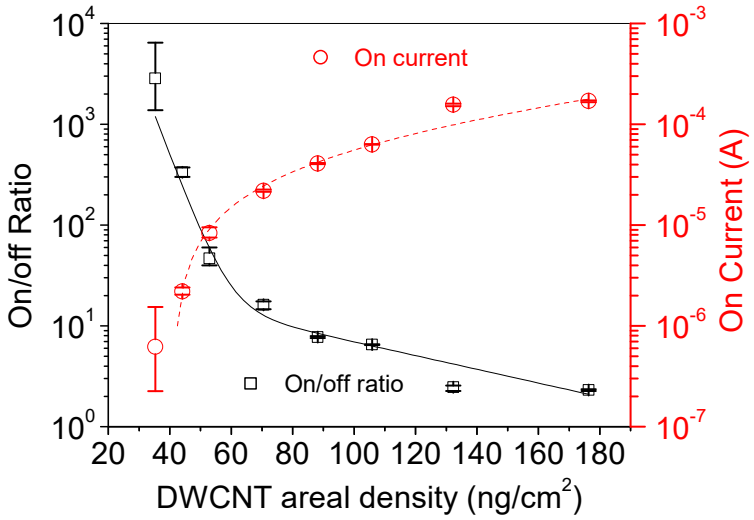

Figure 3-5. High source-drain current and on/off ratio can be simultaneously achieved in DWCNT TFTs at a network density around 50 ng/cm^2. The source-drain current at V_g = -40 V and V_{SD} = -1 V (red) and on/off ratio (black) of DWCNT TFTs were plotted as a function of DWCNT areal densities.

We found that both high on/off ratio and ON current can be simultaneously achieved at DWCNT densities around 50 ng/cm^2. As shown in **Figure 3-6**, TFTs prepared with an areal density of 35 ng/cm^2 DWCNTs possessed excellent transistor characteristics. Even after functionalization by $–C_6H_5COOH$ groups, this device still exhibited on/off ratio as high as 4,000 when measured in water. Higher on/off ratio can be achieved if DWCNTs with semiconducting inner tubes can be separated further from those with metallic inner tubes. However, low DWCNT density also leads to low source-drain current due the smaller quantity of DWCNTs within the network. With our device structure, the source-drain current of DWCNT TFTs with an areal density of 35 ng/cm^2 can be lower than 1

μA at V_g = -40 V and V_{SD} = -1 V, as shown in Figure 3-5. Vice versa, increasing DWCNT areal density increases the drain current of TFTs, but also decreases the on/off ratio of the device due to the larger number of DWCNTs with metallic inner tubes within the percolated network. In order to obtain sensor devices with desired on-current and reasonable on/off ratio, TFTs with a DWCNT areal density of 53 ng/cm^2 were chosen and used for the sensor platform.

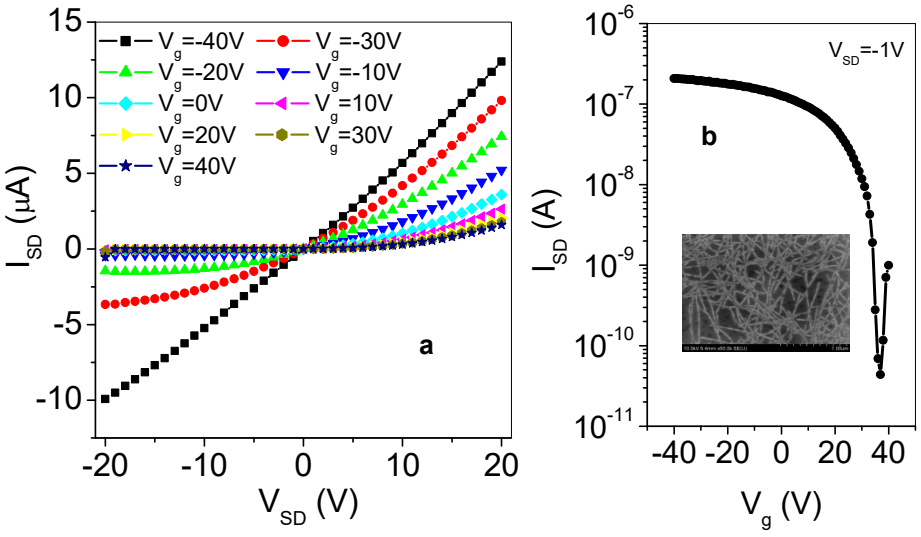

Figure 3-6. (a) Source-drain I-V curves and (b) transfer characteristics of a DWCNT TFT after covalent diazonium functionalization. Inset shows a SEM image of the DWCNT thin film.

To demonstrate the application of Tube^2 TFTs for selective chemical detection, outer wall-functionalized and pristine DWCNT TFTs were tested in 0.06 mM NH_3, 1 mM NH_2PhNH_2, 10 mM CH_3COOH, and 10 mM H_2SO_4 aqueous solutions. Acids with higher concentrations than NH_3 were used in order to show the selective response of the sensors. **Figure 3-7** compares the change in the transfer characteristics of DWCNT TFTs

with and without functionalization upon exposure to analyte solutions. The normalized TFT response was plotted as a function of gate voltage. The device with -C_6H_4COOH functionalized DWCNT exhibited much higher response upon exposure to NH_3 and NH_2PhNH_2 compared to that of pristine DWCNT TFTs. For the pristine DWCNT TFT, a reduction of about 34% in drain current was observed when the device was exposed to 0.06 mM NH_3 solution, while 68%, or twice as much drain current reduction was observed for the Tube^2 TFT. The normalized sensitivity (normalized drain-current change upon exposure to analytes, relative to water, per analyte concentration unit) of this device is as high as 1133% per mM NH_3. The sensitivity towards NH_2PhNH_2 was also improved by the –C_6H_4COOH functional groups. When the functionalized device was exposed to 1 mM NH_2PhNH_2 solution, we observed a 43% reduction in the drain current, versus the 22% with the pristine DWCNT TFTs. This nearly two-fold increase in sensitivity can be attributed to the -C_6H_4COOH functional groups on outer walls of the Tube^2 structures because of the acid-base interactions between the covalently attached carboxylic acids on the outer sidewall with the amine analytes.

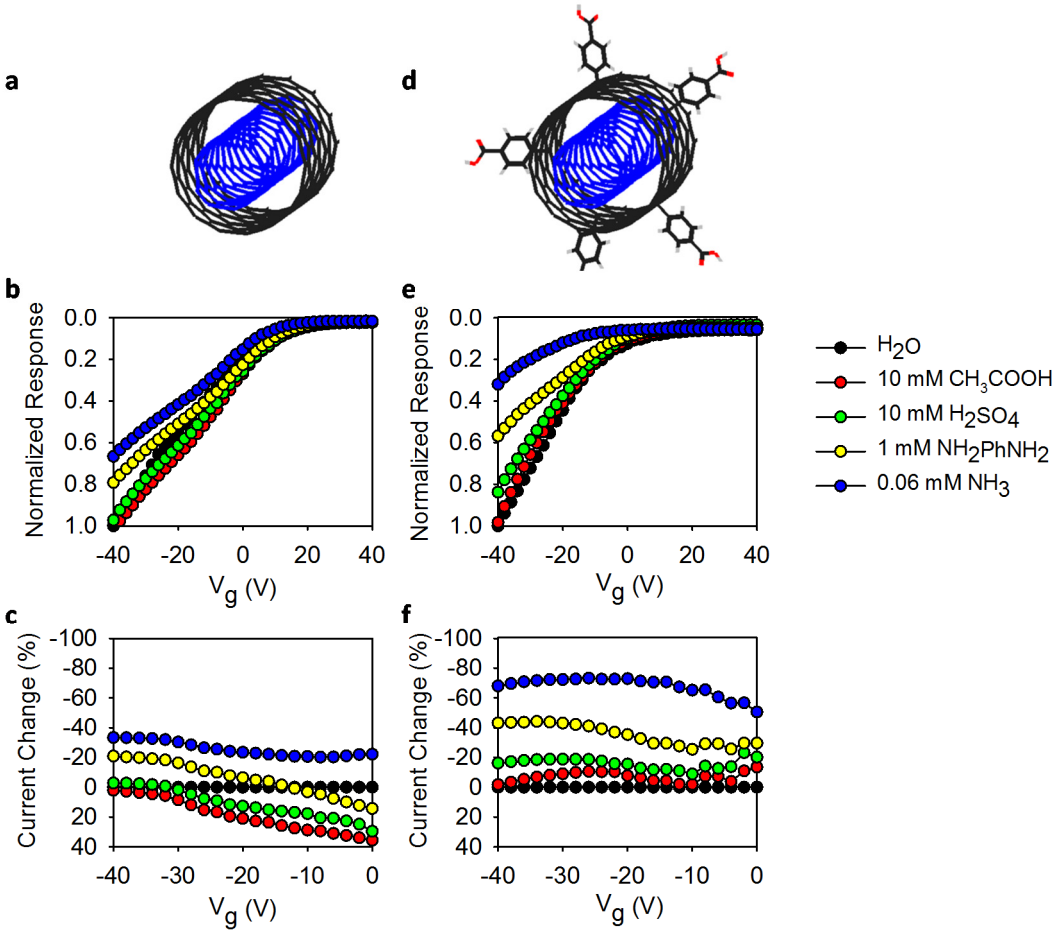

Figure 3-7. Tube^2 TFTs show much higher chemical selectivity than that of pristine DWCNTs.

In addition, the normalized sensitivity (1133% per mM) of the Tube^2 TFT upon exposure to 0.06 mM NH_3 was 6,000 times higher than the sensitivity to 10 mM acetic acid (0.17% per mM), which demonstrates the chemical selectivity of this novel sensor device based on the chemical interactions between the terminal groups on the outer sidewall with analytes. The diversity of sensor responses observed upon exposure to different analytes shows the selectivity of the sensor device.

To further demonstrate the capability of Tube^2 for low-concentration small molecule detection, a -C_6H_4COOH functionalized Tube^2 TFT was tested in diluted NH_3 solutions varying from 60 nM to 60 μM. The change of transfer characteristics of this device upon exposure to successively increasing concentrations of NH_3 solution is shown in **Figure 3-8**a, with the transfer characteristics measured in nanopure water acting as the baseline. Figure 3-8b summarizes the corresponding relative drain current response ($\Delta I_{SD}/I_{SD,H2O}$) of this Tube^2 TFT as a function of NH_3 concentration. Drain current measured at V_g = -20 V and V_{SD} = -1 V was used as output signal. NH_3 was detected at concentrations as low as 60 nM in water, which is comparable to state-of-the-art TFT sensors based on SWCNTs.[105,115] This value may be further improved by optimizing device structure and utilizing external aid such as pre-concentrators.

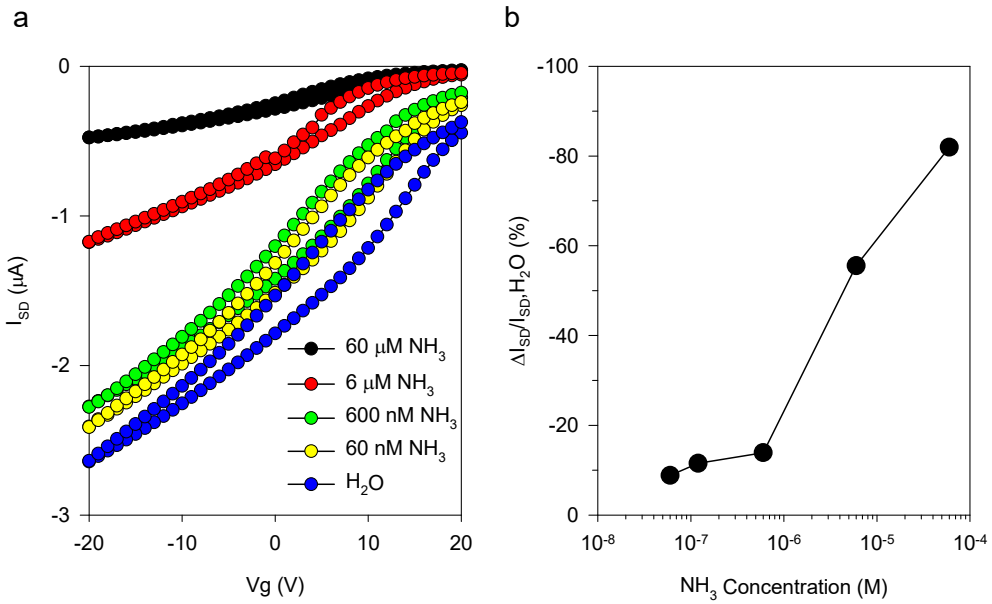

Figure 3-8. Sensitivity of Tube^2 TFTs. (a) Transfer characteristics and (b) the normalized current change ($\Delta I_{SD}/I_{SD},H_2O$, at V_g = -20 V) of a Tube^2 TFT as a function of NH_3 concentration.

3.3. Conclusions

We proposed a double-wall materials concept to address the challenge of simultaneously attaining ultrahigh selectivity and sensitivity in electrical sensing based on carbon nanostructures. Proof-of-concept TFT devices based on covalently functionalized DWCNTs were fabricated and analyzed against SWCNT and MWCNT TFTs for the detection of different amines in aqueous solutions. We found that the covalently functionalized DWCNT TFTs yielded excellent transistor properties showing an on/off ratio as high as 4,000. With carboxylic acid-functionalized outer walls, the devices displayed a sensitivity of 60 nM (or ~1 ppb), while simultaneously displaying a chemical selectivity as high as 6,000 towards a variety of amine containing analyte molecules over other small molecule analytes. This combined ultrahigh sensitivity and selectivity was made possible by the unique double-wall structure of DWCNTs, which simultaneously enables high sensitivity of SWCNT TFTs and the desirable chemical selectivity by outer wall selective covalent modification. This double-wall device platform thus opens new opportunities for chemical and biological sensing where simultaneously sensitivity and selectivity are desirable for detecting trace analytes of interest within the typically complex chemical environments.

3.4. Experimental Section

Nanotube Dispersions: High-purity DWCNTs were separated from a CVD-grown sample (Unidym DW411UA) using density gradient ultracentrifugation (DGU).[59] The sorted DWCNTs have an average diameter of 0.86 and 1.61 nm for the inner and outer wall nanotubes, respectively. Purified arc-discharge MWCNTs (n-Tec) were dispersed in aqueous 0.25% sodium dodecyl sulfate. SWCNT solutions were prepared using a

procedure derived from a previous publication.[18] Raw SWCNTs (10 mg, HiPco Lot R0513) were dispersed in a 25 mL of aqueous 1% sodium cholate solution (99.9% Sigma Aldrich) by tip-sonication (MISONIX ultrasonicator operated at a power level of 17 W) in a cooled (15 ℃) stainless steel cup for 2 hours. The nanotube dispersion was centrifuged at 64,700g for 2 hours (Beckman Coulter Optima LE-80K; 70 Ti fixed angle rotor), after which the supernatant was collected. The concentrations of the SWCNT dispersions were adjusted with 1% sodium cholate/H_2O solution to a similar optical absorbance as that of the DWCNT solution (O.D. ≈ 0.032 @ 1000 nm).

Diazonium Salt Preparation: 4-aminobenzoic acid (4.814 mmol, 99%, Sigma Aldrich) was added to 3 mL of nanopure water in a 10 mL round bottom flask. An aqueous solution of tetrafluoroboric acid (2.68 mL, 48 wt.%, Sigma Aldrich) was then added and the mixture cooled in an ice bath. 670 mg of sodium nitrite (Sigma Aldrich, ≥97.0%) was dissolved in 2 mL of nanopure water and added dropwise to the mixture while stirring. The mixture was allowed to react for 15 minutes. The precipitated diazonium salt was collected and washed with ~200 mL of diethyl ether. The purified salt was dried under vacuum in the dark for 20 minutes. The salt was stored at 4℃ and was used within a week after synthesis.

Raman Spectroscopy: Raman spectra were collected on Horiba Jobin Yvon LabRAM Raman microscope (model ARAMIS) with excitation lines that included 532 nm and 633 nm.

UV-vis-NIR Absorption Spectroscopy: Optical absorption spectra were measured using a PerkinElmer Lambda 1050 UV-Vis-NIR spectrophotometer equipped with a PMT and an InGaAs detector.

Device Fabrication: Heavily doped silicon wafers with 300 nm of thermally grown silicon dioxide were used as substrates for all the devices. Prior to the fabrication, the substrates were cleaned by rinsing sequentially with acetone, 2-propanol, ethanol, and water. Bottom-gate top-contact CNT TFTs were fabricated on carbon nanotube thin films that were prepared using a modified filtration method.[93] CNT solutions were filtered through 47 mm mixed cellulose ester (MCE) filter membranes and rinsed with water to remove surfactant. The resulting percolated CNT films along with the filter membranes were placed onto the substrate with the CNT films contacting with silicon oxide surfaces, compressed by applying force, and thermally annealed at 95℃ for one hour to provide the nanotube film with sufficient adhesion to the substrate. After heating and compression, the MCE filter membrane was dissolved using an acetone vapor bath and rinsed with fresh acetone and ethanol. Finally, Cr (10 nm) and Au (50 nm) electrodes were thermally evaporated through shadow masks. Channel length and width are 2.5 and 4.0 mm respectively. For devices with surface functionalization, the CNT TFTs were immersed into 236 mgL^{-1} diazonium solution and slowly stirred for 24 hours in the dark at room temperature, followed by copious rinsing in nanopure water.

Small Molecule Detection: For aqueous sensing measurements, a rectangular region was defined using electronic coating polymer (3M company Novec, EGC-1700) to hold a liquid droplet on each CNT TFT. The polymer was used to protect the Au electrodes from direct contact with the liquid solution. Each sensor was tested sequentially in air, nanopure water, and analyte solutions. Electrical measurements in liquid were performed by placing a droplet (4 μL) of liquid in the designed region between the source-drain electrodes, with the entire channel immersed by the liquid. All DWCNT TFTs exhibited

robust performance with stable drain currents in water. No obvious degradation of the CNT TFTs was observed during the measurements. Source-drain current-voltage (I_{SD}-V_{SD}) curves of the sensors in nanopure water were measured as the baseline for the devices. After the baselines were established, another droplet of analyte solution was added into the pool and I-V curves were measured over time. To recover the sensor devices, sensors were rinsed with copious amounts of nanopure water and then vacuum dried for 24 hours to remove water.

4. Chemical Gating of a Tube-in-a-Tube Semiconductor

(This chapter is adapted from the submitted article Chemical Gating of a Tube-in-a-Tube Semiconductor by Ng, A. L.; Chen, C. F.; Kwon, H.; Peng, Z.; Lee, C. S.; Wang, Y. H. Ng, A. L. performed the functionalization and modification of Tube^2, device and sensor fabrication, and wrote the manuscript.)

4.1 Introduction

The Information Age started with our ability to modulate current in a semiconductor by an electrical field. Exploitation of this gating effect, through chemical binding events, has generated sensitive field-effect transistor (FET) sensors capable of detecting a variety of biological and chemical species.[10,116-119] Owing to its real-time, label-free, and miniaturized size features, electrical sensing is an attractive platform for on-site biodetection of viruses and protein markers as current diagnostic techniques still typically rely on methods such polymerase chain reaction[120] (PCR) and enzyme-linked immunosorbent assays[121] (ELISA) are time-consuming, and require sophisticated instrumentation and specialized technicians due to multistep procedures However, a critical challenge to translating FETs into biochemical sensor platforms is the requirement of a gate electrode.[122,123] The gate electrode is used to apply an electrical potential in order to capacitively switch the semiconductor to a high sensitivity ON-state. Since the semiconductor has to be exposed to the analytes, the devices are typically gated through a bottom electrode or an immersed electrochemical electrode. In both cases the gating is typically applied globally. The gate electrode imposes restrictions on sensor device architectures typically to planar structures and also results in added expense,[48] poor scalability,[124] and electrical noise.[119]

Here we show that it is possible to eliminate the need of a physical gate electrode and dielectrics within the FET sensor configuration using a synthetic tube-in-a-tube (Tube^2) semiconductor. Tube^2 is uniquely composed of a semiconducting single-walled carbon nanotube nested in a charged, non-permeable covalent functional shell that allows the semiconducting conduction pathway to be modulated solely by surface receptor groups in a chemically gated-all-around configuration (**Figure 4-1**). The semiconducting channel and receptor shells are separated only by a subnanometer, van der Waals spacing. Compared to the conventional FET sensor device architecture, our new device architecture requires only two electrodes: source and drain, without the need of the third, gate electrode. The removal of the physical gate electrode significantly simplifies the device architecture and enables photolithography-free, highly scalable fabrication of nonconventional FET sensors. Miniaturized two-terminal point sensors can be readily fabricated using a simple, straightforward dice-and-dip procedure. We show that concomitant FET sensitivity and single mismatch selectivity can be achieved with Tube^2 even in a chemiresistor-like, two-terminal thin film device configuration.

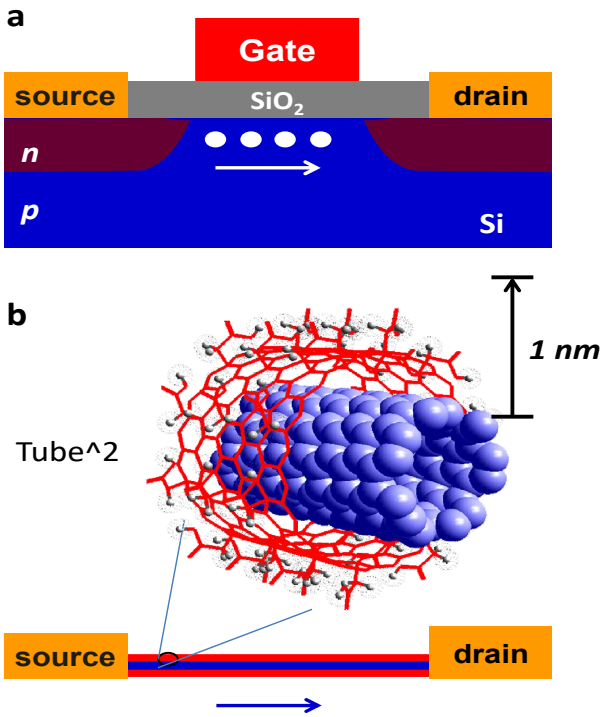

Figure 4-1. Schematic of chemical gating of a tube-in-a-tube semiconductor. (a) Schematic of a conventional top-gated silicon FET. (b) A chemically gated FET based on Tube^2.

4.2. Results and Discusssion

To demonstrate this new concept of gate electrode-free detection, Tube^2 thin film transistor (TFT) sensors were created through covalent, outer wall-selective functionalization of sub-monolayer networks of semiconducting double-walled carbon nanotube (DWCNT) precursors that were pre-sorted using density gradient ultracentrifugation.[21,59] Fabrication of these TFT sensors were prepared using hole doped silicon substrates with a 300 nm silicon oxide dielectric layer. Although the major goal of this work is to demonstrate the possibility of eliminating the need of gate electrodes, the fabricated transistors can be back-gated globally using the hole doped silicon substrate. This device configuration has been well established in the literature and allows us to

quantitatively compare chemical gating in Tube^2 with conventional TFT characteristics including threshold voltage (V_{th}) and carrier mobility.[80,83] Towards the later section of this paper, we will further show it is possible to fabricate two-terminal, free-standing point sensors.

The outer tube of DWCNT was selectively functionalized with 2-fluorobenzoic acid groups using an electrochemically accelerated diazonium reaction.[125] Diazonium chemistry was chosen due to its outer wall-selectivity and the tunable functionalization of aryl substituents, as demonstrated by us[13,35,62] and Martel *et al*.[63] Benzoic acid terminal groups provide concomitant versatility as a linker[126] and an abundance of negative charge at neutral pH (the pKa of benzoic acid is ~4), which is useful for chemical gating. We found that the presence of fluorine at positions ortho relative to the carboxylic acid group improved the functional degree by ~40%. This is attributed to reduced polymerization, which is known to inhibit the functionalization efficiency of diazonium reactants,[127] by the fluorine in place of an aryl hydrogen. Covalent attachment was verified through Raman spectroscopy (**Figure 4-2**a) showing the growth of the D phonon around 1300 cm^{-1}. The covalent functional degree of the Tube^2 channel was assessed using the peak area ratio of the D and G bands, which quantify the relative ratio between sp^3 and sp^2 carbon sites, respectively. By modulating the reaction time and aryldiazonium salt concentration, various functional degrees can be achieved. Transmission peaks indicative of the covalent attachment of 2-fluorobenzoic acid were observed in the IR spectra, which include the broad carboxylic acid feature of the functional group and the absence of the diazonium peak that usually appears at 2250 cm^{-1}.

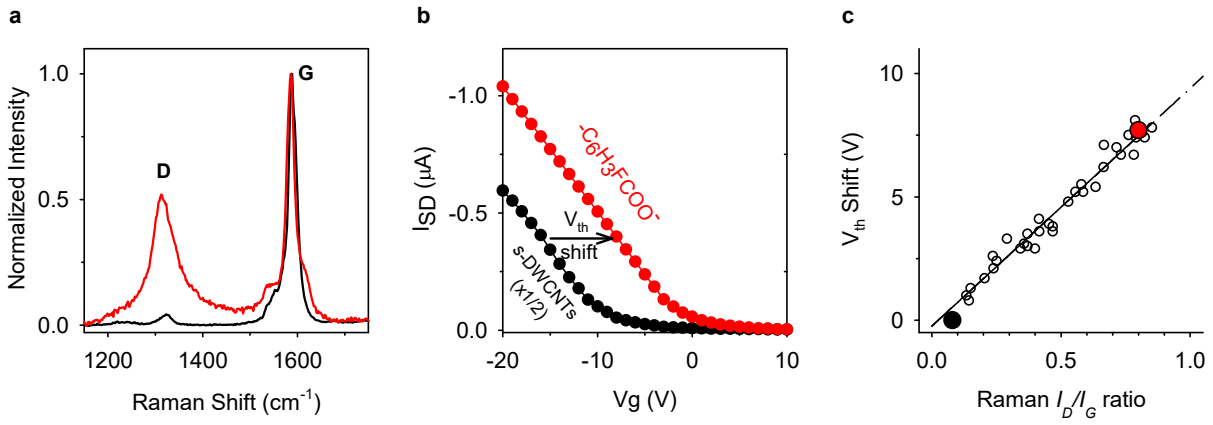

Figure 4-2. Chemical gating mechanism of Tube^2 thin film transistors. (a) Raman scattering of a 2-fluorobenzoic acid functionalized Tube^2 thin film (red curve) and its precursor, DWCNT (black curve). (b) Transfer characteristics of the DWCNT TFT (black; current divided by a factor of two), and the Tube^2 TFT (red). (c) V_{th} shift as a function of Raman I_D/I_G ratio for 35 Tube^2 TFTs. The data points corresponding to the black and red curves in (a) and (b) are highlighted as the solid black and red dots, respectively.

After outer wall covalent functionalization of DWCNTs to generate Tube^2, two approximately independent and distinct changes in the electrical transport are observed. As previously reported by us,[62] the first change is approximately a 50% decrease in conductance associated with the loss of electrical transport mobility of the outer wall. The second change results from chemical gating effects associated with the charge from the attached group[128] and can be measured as shifts in the transport properties (Figure 4-2b). The threshold voltage (V_{th}) shifts of functionalized DWCNT films show a strong linear correlation with the Raman I_D/I_G peak area ratios, after accounting for the loss of outer wall mobility (Figure 4-2c). We deduce that the increasing functional density of the negatively charged benzoic acid groups is generating shifts in the transport properties indicating that

the dominant sensing mechanism for the Tube^2 devices is chemically-driven electrostatic gating. The mechanism of electrostatic gating is further evidenced by the ability of the Tube^2 devices to have higher sensitivity towards ammonium molecules at higher pH when the carboxylic acid groups are deprotonated. The ability to chemically modulate the gating environment of the Tube^2 transistor by simple tuning of the functional group and functional density allows for new opportunities to use chemically attached groups as integral gate components to the device architecture.

Unlike unfunctionalized and noncovalently-modified single-walled carbon nanotube (SWCNT) transistors, we have observed that our Tube^2 devices have additional advantages such as minimal nonspecific binding to the graphitic surface. We believe the higher packing of functional groups in the outer functional shell creates sufficient steric and electrostatic repulsion to inhibit nonspecific binding to the graphitic surface (**Figure 4-3**). Ruling out nonspecific binding of target and interferant compounds, we can deduce that the chemical gating of our Tube^2 TFTs are predominantly a result of specifically bound functional groups.

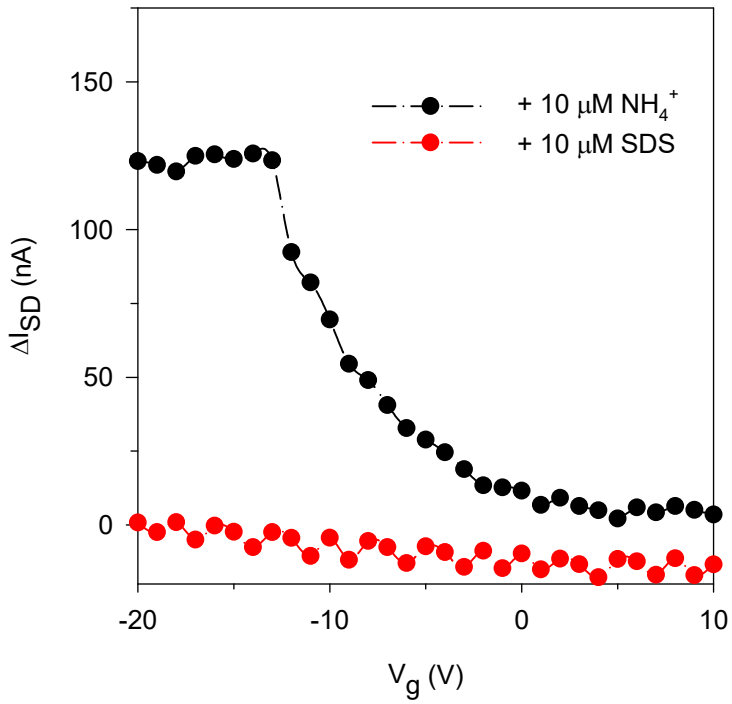

Figure 4-3. Transport curves of Tube^2 TFTs to specific and nonspecific binding. Current versus gate voltage for a p-type Tube^2 TFT when exposed to target (ammonium, black) solution and interferant (sodium dodecyl sulfate, red).

To demonstrate the extensiveness of chemical gating in Tube^2 and its applicability towards sensing, a terminal 23–base amino-modified single-stranded oligonucleotide (ssDNA) (5'-/AmMC6/ATG GTG GAT AGG CGA CTC ACG TT/-3') was linked to the Tube^2 benzoic acid moieties for DNA detection (**Figure 4-4**a). DNA possesses a doubly negative charged phosphate group per base. With increasing oligonucleotide base length, larger electrostatic gating effects can be applied to the inner tube transducer. Upon attachment of the ssDNA, the V_{th} shifts by an additional factor of two compared with the fluorobenzoic acid groups and effectively turns the transistor "ON" without the use of a physical gate (Figure 4-4b). Accordingly, the conductance increases over 10 times (Figure

4-4c). These observations unambiguously demonstrate that chemical gating can be used as a technique to switch our Tube^2 thin film devices from the OFF-state to the ON-state and can provide the same amplification effect as that achieved through gating with a conventional gate electrode.

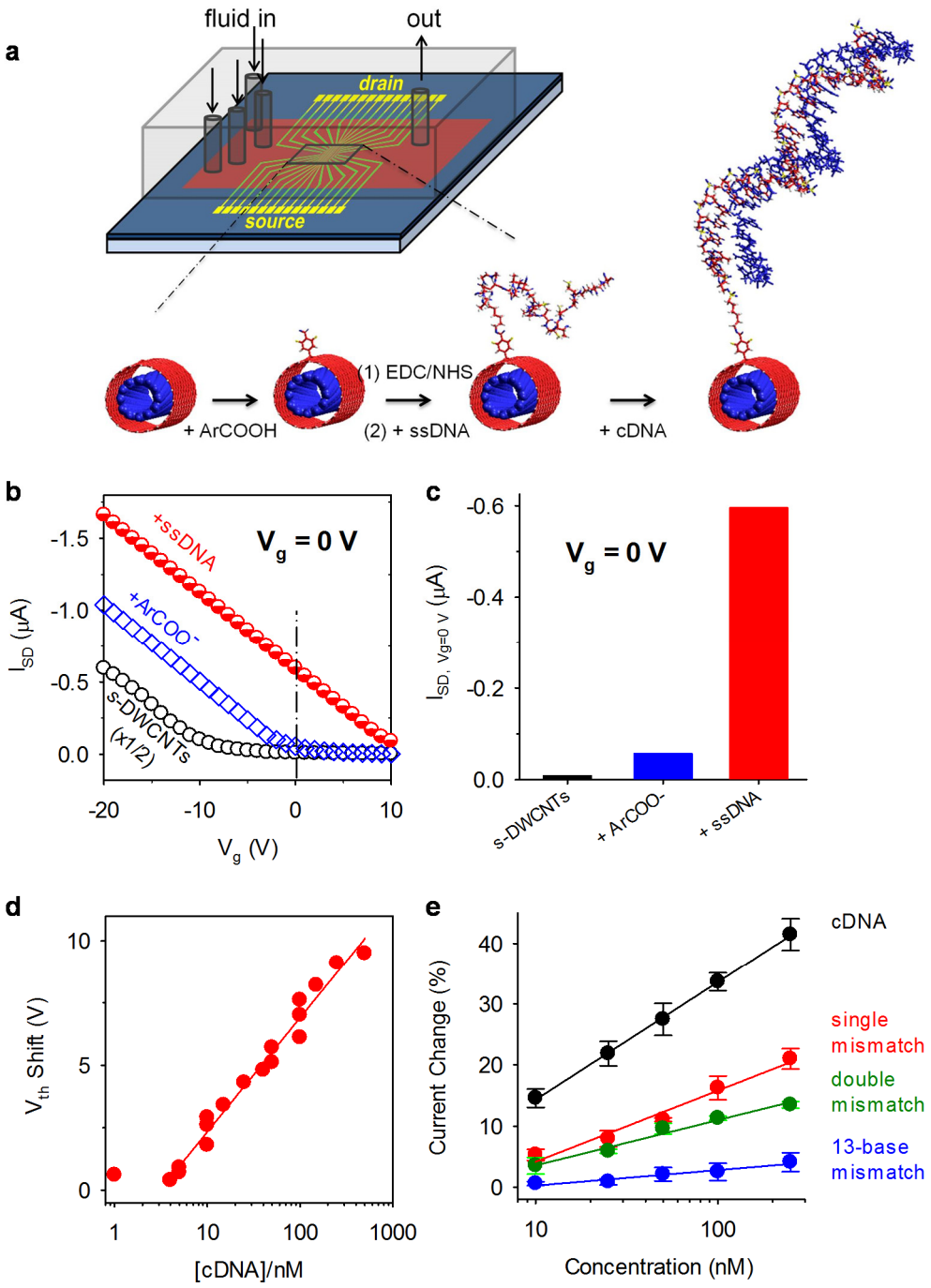

Figure 4-4. Gate electrode-free ssDNA TFT sensors show concomitant high selectivity and sensitivity.

To demonstrate that the ssDNA tagged Tube^2 TFT under non-gated conditions can perform as well as electrode-gated TFTs, varying amounts of the 23-base complementary DNA (cDNA) (sequence: 5'-/AAC GTG AGT CGC CTA TCC ACC AT/-3') were added to test the sensor sensitivity (Figure 4-4d). All oligonucleotide solutions used for detection were prepared in 10 mM phosphate buffered saline (PBS). The cDNA concentration could be approximately quantified by V_{th} shifts in the electrical transport after the addition of cDNA. Nine devices with different mobilities (0.5 - 5.0 cm^2/Vs), but similar functional degrees, were tested and show a strong correlation between cDNA concentration and V_{th} shift down to below 5 nM, which is comparable with three-terminal electrochemical[129] and FET sensors.[130] Upon hybridization, higher concentrations of cDNA generated larger chemical gating shifts resulting in significant modulation in the conductance. This enables the cDNA to be electrically detected without the use of an external gate. The selectivity of ssDNA-modified Tube^2 TFTs were evaluated by differences in conductance when exposed to a non-complementary DNA sequence (ncDNA) versus the cDNA sequence. Addition of ncDNA sequences with single (5'-AAC GTG AGT CGC CTA TCC AC**T** AT-3'), double (5'-AAC GT**T** AGT CGC CTA TCC AC**T** AT-3'), and 13 mismatched bases (5'-/**T**A**T** T**AT TA**T **TAT** T**AT TT**T/-3') showed progressively smaller conductance increase than the cDNA (Figure 4-4e). Single mismatch selectivity, at nanomolar concentrations and throughout the large concentration range tested, can be achieved without the use of an external gate and any amplification

techniques. This exceptional selectivity can be explained by the high functional degree of probes on the Tube^2 surface, allowing for affinity between fully matched sequences, but selectivity for mismatched sequences due to steric effects. These experiments clearly show that chemically gated Tube^2 TFTs possess simultaneous high sensitivity and selectivity similar to their electrode-gated counterparts, which have further shown that when combined with amplification techniques femtomolar detection of oligonucleotides can be achieved.[53,82]

To further verify that electrostatic/chemical gating is the dominant sensing mechanism, oligonucleotide length dependence studies were performed. In support of this hypothesis, longer ssDNA sequences, which have more negative charge, generate larger chemical gating effects and signal response upon hybridization due to a larger amount of bound charge. By increasing the ssDNA probe and cDNA target from 10 to 23 bases, the projected detection limit improved by approximately 40% and the concentration dependence on V_{th} shift (the slope) decreased by a factor of about 2.5 (**Figure 4-5**).

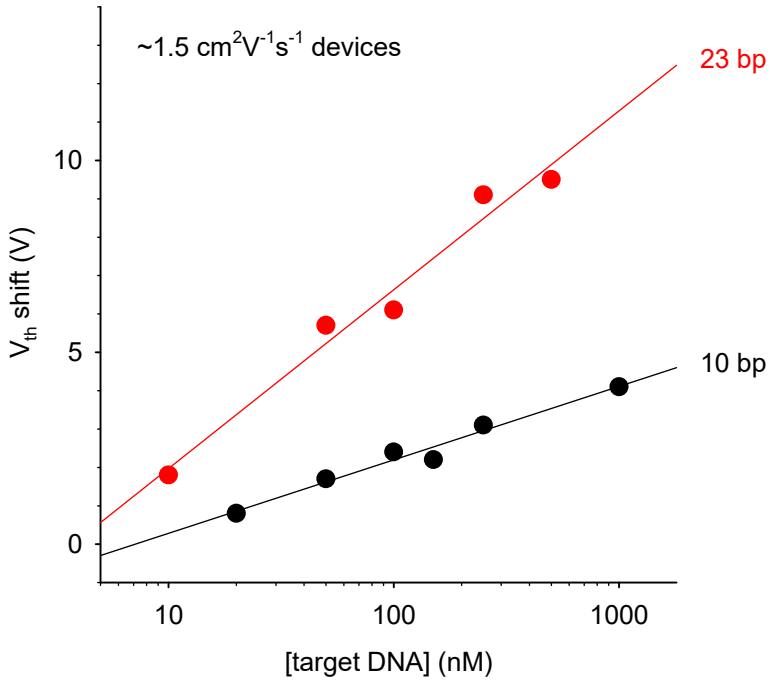

Figure 4-5. Base pair dependence. Threshold voltage shifts in response to oligonucleotide concentration for ssDNA modified Tube^2 TFTs.

To test the feasibility of the chemically gated Tube^2 TFT platform for detecting realistic targets, we demonstrate the detection of the 123-base Mycobacterium tuberculosis biomarker (IS6110). Although tuberculosis is treatable, its extremely high transmission rate and few symptoms cause it to result in an approximately 1.5 million deaths annually worldwide. Current diagnostic methods are either low in sensitivity (only 34–80%, sputum smear microscopy), time consuming (requires 9-16 days for culture of bacilli), or too sophisticated (molecular species diagnostics) to be adopted for developing countries. Furthermore, the majority of newly infected cases are in the developing countries meaning a rapid, simple, low cost, and highly accurate on-site detection platform for early diagnosis can have great positive impact on public health. To detect IS6110, a 15-base amino-modified ssDNA probe (/5AmMC6/GC GAG CGT AGG CGT C) that is complementary

at the 3' end of one of the IS6110 DNA strands was linked to the functionalized Tube^2 devices. The IS6110 double-stranded DNA (dsDNA) was dehybridized by melting and immediately dispensed through the ssDNA-modified TFTs using microfluid channels. Upon addition of IS6110 marker, similar to the binding of the model 23-base cDNA, chemical gating shifts in transport properties that resulted in an increase in conductance were observed. This is consistent with specific IS6110 attachment to the probe-modified Tube^2 TFT.

Without the need for a third terminal and a dielectric, a Tube^2 point sensor can be assembled with only two device requirements: source/drain electrodes and the Tube^2 thin film (**Figure 4-6**a). To demonstrate the functionality gained through eliminating a physical gate electrode, two-terminal point sensor was created using a photolithography-free, high throughput dice-and-dip procedure. Electrodes are easily fabricated by double-sided deposition of gold on an undoped silicon wafer and individual devices are mass produced by dicing the metal-silicon-metal wafer into millimeter scale pieces (Figure 4-6b). The channel length (20 μm) of the device is defined directly by the cross-sectional thickness of the Si wafer. Tube^2 sensing devices are created in parallel by self-assembling DWCNT networks across the cross-section of the wafers followed by diazonium functionalization and oligonucleotide coupling. The overall conductivity between point sensors varied more than the traditionally fabricated TFTs, which may arise due to varying Tube^2 densities and network morphologies from the dice-and-dip procedure, but for a set of 24 point sensors, all readily achieved nanomolar sensitivity for IS6110, closely matching the performance of microfabricated on-chip devices (Figure 4-6c,d).

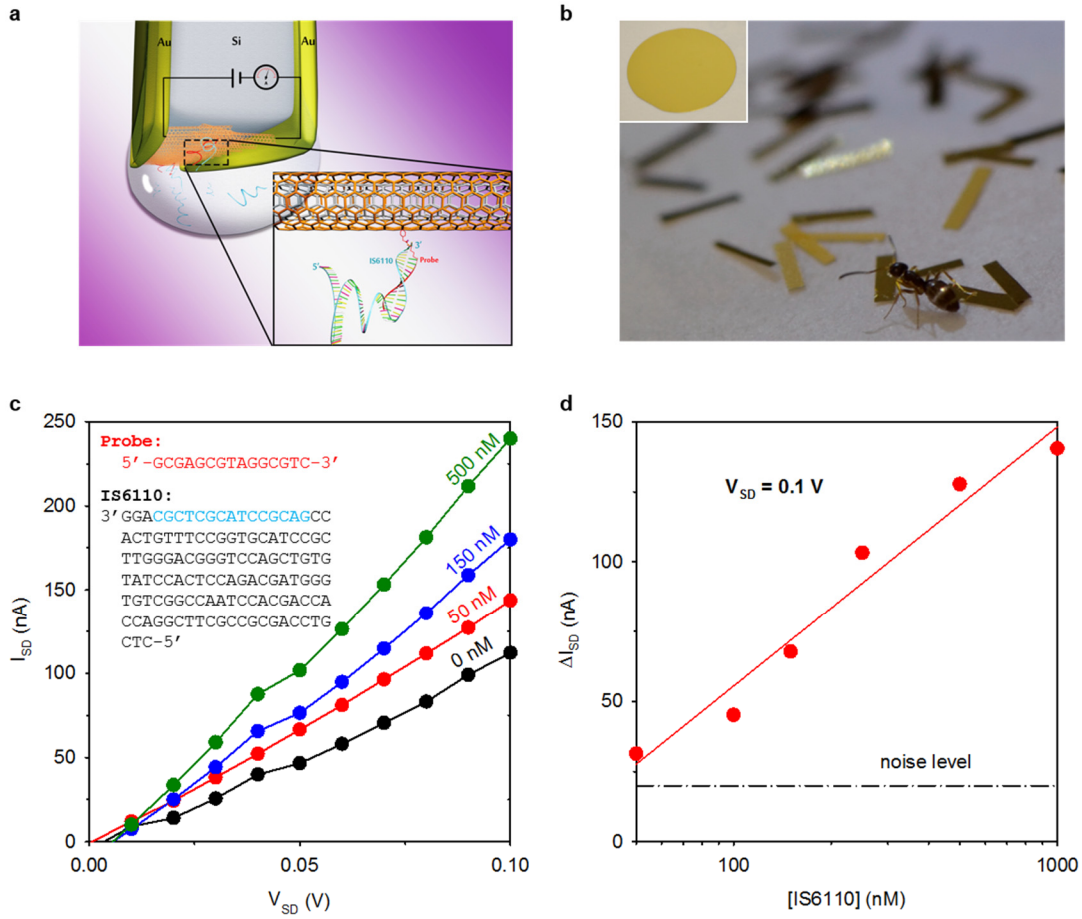

Figure 4-6. Tube^2 point sensor for tuberculosis biomarker detection. (a) Schematic of a Tube^2 point sensor immersed in a drop of biofluid containing IS6110. (b) Photograph of Tube^2 point sensors fabricated from a metal-silicon-metal wafer (inset) by a simple dice-and-dip procedure. Note that the paratrechina flavipes ant that is exploring has a size similar to the sensors (3.5 mm × 0.5 mm × 20 μm). (c) I-V curves of Tube^2 point sensors in response to IS6110. Inset shows the sequences of the probe DNA and IS6110. (d) Current change of Tube^2 point sensors when exposed to various IS6110 concentrations.

4.3. Conclusion

In conclusion, we demonstrated that Tube^2 semiconductors can be gated solely by chemically attached groups enabling gate electrode-free thin film transistor sensors. Enabled by this novel semiconductor, two-terminal thin film transistor sensors were shown to reach nanomolar detection limits towards the detection of a 23-base cDNA sequence, while simultaneously achieving single base mismatch selectivity. Our chemically gated TFT sensors have also demonstrated the ability to detect IS6110, a known DNA biomarker of tuberculosis. The ability to fabricate a high performance sensor without a gate electrode enabled the creation of a photolithography-free, high throughput Tube^2 point sensor with FET sensitivity and selectivity, but using a two-terminal configuration that is significantly simplified compared to the conventional three-terminal FET sensors. This two-terminal FET sensor architecture is readily compatible with other versatile fabrication techniques such as paper electronics[131] and lab-on-a-chip devices[132] to maximize the portable, real-time, and label-free advantages of electrical sensing. Even in their infancy, prototypical devices have shown detection limits of oligonucleotides and tuberculosis biomarkers comparable to state-of-the-art three-terminal counterparts that are physically gated.[82,133] This new concept thus may open up new opportunities for device and material innovation.

4.4. Experimental Section

Tube^2 Thin Film Preparation: Double-walled carbon nanotubes (DWCNTs; Unidym DW411UA) were dispersed in 1% wt/vol sodium cholate and sorted by density gradient ultracentrifugation.[59] DWCNT thin films (50 mm diameter) were created using a vacuum filtration method[13,35] where 0.4 μg of DWCNTs were added to 50 nm pore size

nitrocellulose membranes. DWCNTs were transferred to silicon wafers with 300 nm thermal oxide (Silicon Quest International) coating through application of heat and pressure. Nitrocellulose membranes were dissolved using an acetone vapor bath and the DWCNT film was rinsed copiously with isopropyl alcohol, ethanol, and water, followed by an annealing step at 200 ºC in vacuum.

On-chip devices of 15 and 20 μm channel length were patterned using photolithography with Cr/Au contacts of 10 and 75 nm thickness respectively using electron beam deposition. Additional steps of photolithography were used to remove residual DWCNTs between transistor arrays and passivate the electrodes from any reaction.

Devices were characterized for conductance and transport properties using a Keithley 4200 Semiconductor Characterization System followed by an electrical breakdown step to remove metallic DWCNTs. Outer tube selective functionalization was performed using 3-fluoro-4-carboxylbenzenediazonium tetrafluoroborate using electrochemical acceleration with a V_{SD} of 1 V for 30-60 minutes. Further verification of the functionalization was accomplished with FT-IR spectroscopy and further corroborated through Raman scattering (Figure 4-2b).

Further covalent linking of oligonucleotides was performed by linking amino-modified single stranded DNA sequences using 20 mM 1-ethyl-3-(3-dimethylaminopropyl)carbodiimide and 20 mM N-hydroxysuccinimide with 1 μM of the oligonucleotide sequence to the carboxylic acid groups attached to the outer tube.

Device Fabrication: DWCNT TFTs were prepared from hole doped silicon wafers with a 300 nm silicon oxide layer (Silicon Quest International). To reduce hysteresis associated with the charge transfer from the oxide layer, a monolayer of hexamethyldisilazane was

spin-coated on the substrate. Device fabrication was performed using a procedure from previous work.[35] Polydimethylsiloxane microfluidic channels (300 × 300 μm cross-section) were attached to the chip for functionalization and solution introduction.

Electrochemically Accelerated Functionalization with Diazonium Salts: DWCNT TFTs were reacted with 3-fluoro-4-carboxylbenzenediazonium tetrafluoroborate electrochemically. The reagent was synthesized from 4-amino-2-fluorobenzoic acid (Sigma Aldrich, ≥97%), fluoroboric acid, and sodium nitrite using a previously described method.[62] The diazonium structure was confirmed by ^{1}H-NMR (Bruker DRX-400) and FTIR (Thermo Nicolet NEXUS 670 with ATR attachment) spectroscopies. For NMR analysis, samples were dissolved in acetonitrile-d3 (99.8%, Cambridge Isotope Laboratories, Inc). Covalent functionalization was achieved by flowing a 1 mM aqueous solution of 3-fluoro-4-carboxylbenzenediazonium tetrafluoroborate at a rate of 25 μL/min through microfluidic channels attached to the TFTs for one hour. A source-drain voltage (V_{SD}) of 1 V was applied to the transistor region to electrochemically accelerate the reaction. The residual byproducts and reactants were then removed by flowing Nanopure^{TM} water through the microfluidic channels for 30 min at the same flow rate. Raman spectroscopy (Horiba Jobin Yvon LabRAM Raman microscope, model ARAMIS) with an excitation line of 632.8 nm and FTIR was used to characterize the extent of covalent functionalization.

Oligonucleotide Attachment: To efficiently link amino-modified oligonucleotides to Tube^2 thin films with carboxylic acid terminal groups, 1-ethyl-3-(3-dimethylaminopropyl)carbodiimide (EDC) and N-hydroxysuccinimide (NHS) were used to activate the carboxylic acid to the more reactive NHS ester terminal group. The

activation experiment was performed by flowing a mixture of 20 mM EDC and 20 mM NHS at pH 5.8 at a rate of 25 μL/min through microfluidic channels attached to the TFTs for one hour to create the NHS ester moiety. A concentration of 1 μM ssDNA in PBS was then pumped through the microfluidic channels for 5 hours. The channel was washed as previously with Nanopure^{TM} water for 30 minutes.

Complementary oligonucleotide detection was performed by microfluidic flow of cDNA to Tube^2 film. Selectivity experiments were performed by flowing the ncDNA sequence through TFT channel regions using the same flow rate, time, and rinsing process. After each modification step, TFTs were electrically characterized by taking a transfer characteristics plot after stabilization of current values.

IS6110 Biomarker: Luria Bertani (LB) plates containing standard plasmid and the IS6110 123 base fragment were obtained from Department of Laboratory Medicine, Chang Gung Memorial Hospital, Taiwan. The white colonies were selected and grown in LB broth containing 50 μg/mL Ampicilin in a shaker at 37 °C at 225 rpm overnight. DNA was isolated from the culture using AxyPrep Maxi Plasmid Kits and amplified using HotStar Taq DNA Polymerase to confirm the presence of the 123-base fragment. 10 μL of DNA template was used in a 50 μL reaction mixture containing 0.6 μL of each 25 μM primer, 4 μL of 2.5 mM dNTP, 5 μL of 5X Q solution, 5 μL of 10X buffer, 0.25 μL of 5U μl-1 HotStar Taq, and 24.55 μL of RNase free H_2O. The temperature cycling conditions for PCR amplification are initial denaturalized at 94 °C for 15 min, 35 cycles of 94 °C for 1 min, 68 °C for 1 min, 72 °C for 1 min, and a final extension of 72 °C for 10 min. The amplified products were analyzed by gel electrophoresis in 2 % agarose prepared in TBE

buffer, mixed with fluorophore Novel Juice for visualization, and bands were visualized on a UV-light transilluminator.

Covalent linking of 15-base amino-modified ssDNA to the carboxylic acid modified TFT was performed as mentioned in the DNA attachment part of Methods. IS6110 was heated to 95 ºC to dehybridize the dsDNA. The solution was quickly transported to a microfluidic injection system and flowed through the Tube^2 TFT channels at a flow rate of 25 μL/min. Nanopure water was then flowed through the channels to rinse off nonspecifically bound species.

Two-terminal Point Sensors: The Tube^2 point sensors were fabricated by a dice-and-dip procedure. We firstly coated both sides of an undoped Si wafers of 20 μm thickness (Virginia Semiconductor) with Cr (10 nm) for adhesion and then gold (150 nm). Afterwards, the metal-silicon-metal wafer was diced into rectangular pieces (~3.5×0.5 mm^2). The freshly cleaved end was dipped into a 1% sodium cholate stabilized aqueous solution of DWCNTs (20 mg/L) to allow a network of Tube^2 precursors assembled across the two gold terminals. The residual surfactant was removed by Joule heating under a source-drain voltage of 5-10 V and then immersed in ethanol for 10 seconds and repeated two additional times to remove residual surfactants or contaminants. The DWCNTs were converted to Tube^2 by immersing the device in the diazonium and then DNA solutions.

Electrical Characterization: Electrical characterization was performed on a Keithley 4200-SCS semiconductor parameter analyzer. For back-gated devices and gated measurements, transfer characteristic curves were taken after every covalent modification step. Non-gated sampled measurements were taken with Vg = 0 V.

5. Laser Lithography of Tube-in-a-Tube Nanostructures

(This chapter is adapted from the submitted article Laser Lithography of Tube-in-a-Tube Nanostructures by Ng, A. L.; Piao, Y.; Wang, Y. Ng, A. L. contributed to the Tube^2 thin film preparation, electrical characterization, DWCNT network patterning, device fabrication, assistance in Raman characterization, and manuscript writing. Some text and figures are derived from Ref. 144: Electronically Tailored Functionalization of Carbon Nanotubes by Piao, Y. who with Wang, Y. initially conceived this work.)

5.1. Introduction

Carbon nanomaterials, such as single-walled carbon nanotubes (SWCNTs) and graphene, possess remarkable optical,[3] electrical,[134] and mechanical properties,[135] which hold vast potential for innovation[4] in biotechnology,[137] electronic,[138,139] and optoelectronic applications.[140] However, two critical challenges for the integration of CNTs into next-generation electronic and optoelectronic devices are mixed electronic types of CNTs and the ability to create ordered structures from these nanoscale materials. As such, a major goal is the ability to pattern CNTs with high spatial precision with electronic-type specificity.[14,38] Patterning techniques such as directed assembly[141] and guided growth[142] have attempted to meet this challenge, but require lengthy, sophisticated steps and electronic type specificity that falls well short. Selective growth of CNTs by electronic type[38,39,143] and other solution-based purification techniques have been developed, but there is still no technique that completely sorts semiconducting CNT structures.[21,40,43,45]

A previous, unpublished study done by a previous group member and project collaborator Yanmei Piao,[144] developed a CNT lithography method that is capable of

patterning CNTs with the potential of electronic type specificity (**Figure 5-1**). This method is enabled by a unique tube-in-a-tube (Tube^2) structure, which were created synthetically from outer tube-selective functionalization of double-walled carbon nanotubes (DWCNTs).[62,63] Using a laser, we demonstrated the ability to remove the functional groups from the outer wall of the Tube^2 structure, restoring optical and electrical properties of the outer wall. We found that annealing of the outer tube of the Tube^2 samples required a threshold power density (**Figure 5-2**a), below which structural recovery does not occur no matter how long the Tube^2 thin film was exposed to the 532 nm laser (Figure 5-2b). This power threshold feature allowed us to anneal CNT structures ("write") and to characterize ("read") the annealed films *in situ* Raman spectroscopy by operating beneath the power threshold to ensure that further defunctionalization does not occur. We then demonstrated the ability to draw dot arrays (**Figure 5-3**) on an initially insulating nanotube thin film by annealing.

It is important to clarify that the initial insulating few monolayer film of Tube^2 nanostructures are insulating not because of covalent functionalization to the outer wall, but because functional groups (~ 1 nm in length) are long enough to prevent the graphitic lattice of the outer tubes to come in contact with one another to allow for electrical conduction through the thin film network. Within each nanostructure, there should still be conductance if individually probed. Upon annealing with a laser this physical barrier of covalently attached groups that impede network conduction is removed allowing for the individual nanostructure to reconfigure likely due to strong interactive forces so that outer tube are in contact for network conduction. At this point, the networks of interest are representative of DWCNT structures as reported in previously reported works that when

functionalized with outer-wall specific functionalization preserves the conduction of the channel without compromising inner-tube properties and characteristics as a result of junctions not being functionalized.[13,62]

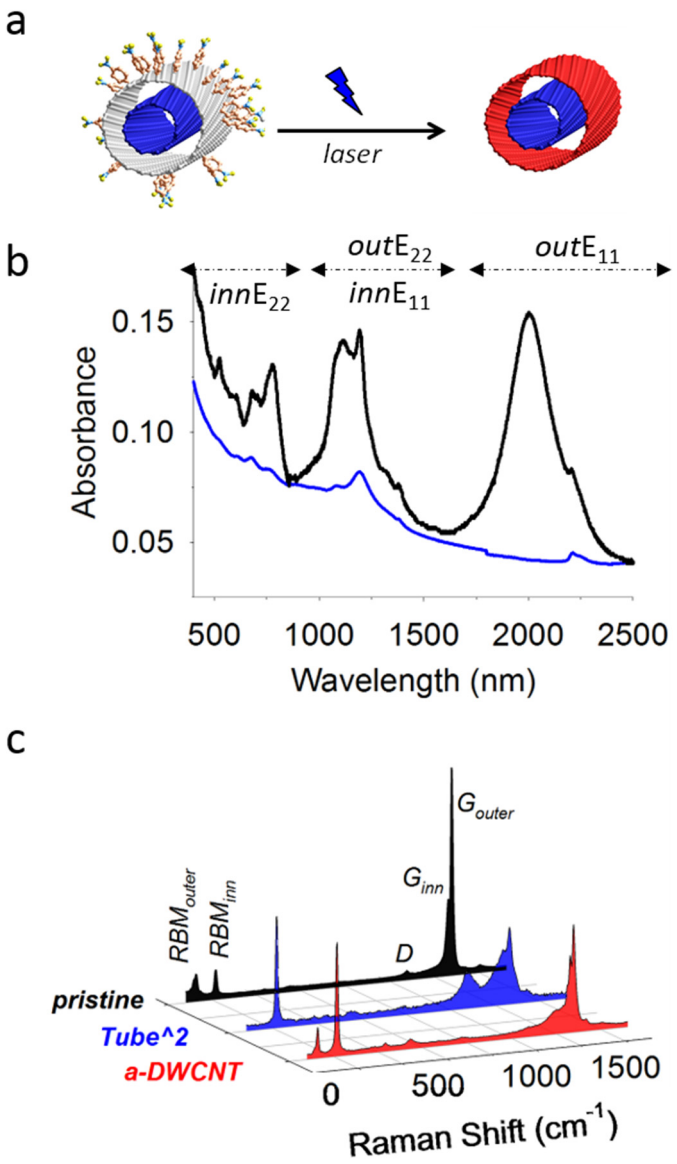

Figure 5-1. Optical removal of surface functional groups on Tube^2 structures. (a) Schematic illustration of optical de-functionalization of a Tube^2 structure with a laser tuned into resonance with the inner tube. (b) Visible-NIR absorption spectra of a DWCNT

film on a quartz substrate, before (black curve) and after outer tube-selective functionalization (blue curve). (c) Raman spectra normalized to G_{inn} reveals the structural recovery of the DWCNT characteristics from the functionalized Tube^2 precursors upon laser annealing. Adapted from ref. 144.

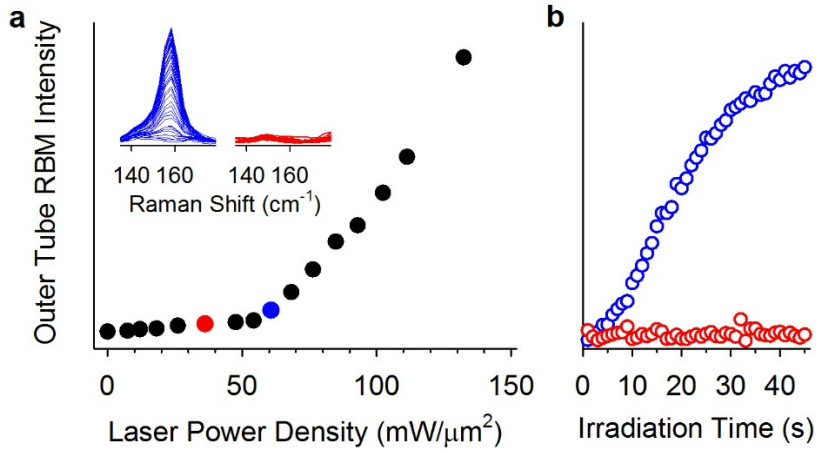

Figure 5-2. (a) Critical power density threshold for annealing the outer tubes of Tube^2 structures. (b) The outer tube Raman intensities of the red and blue spots in (a) are plotted as a function of the laser irradiation time. Adapted from ref. 144.

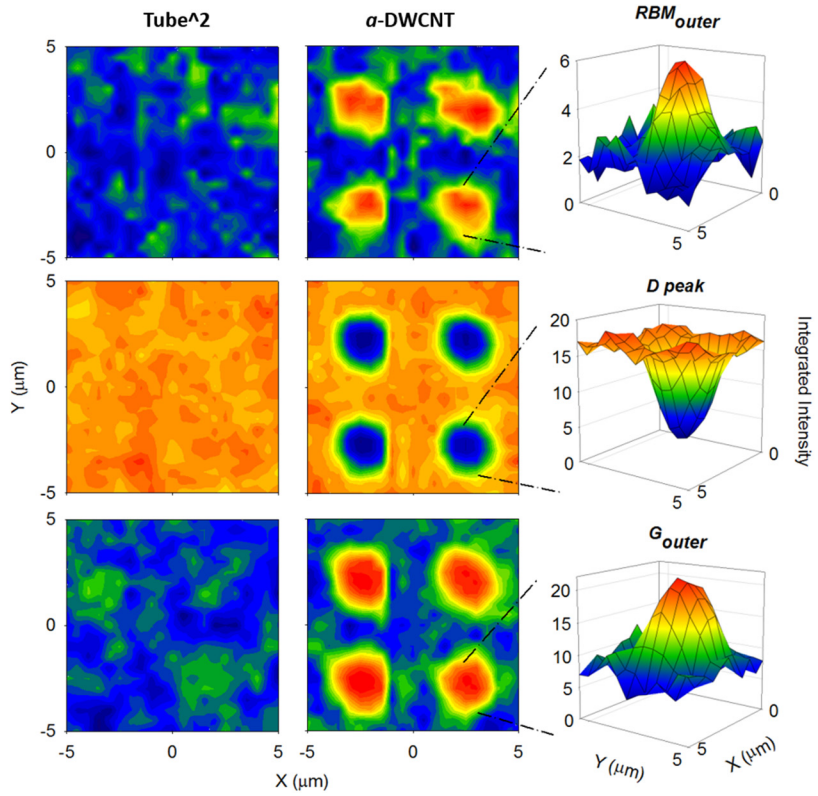

Figure 5-3. *In situ* Raman mapping confirmed the fabrication of a 2 x 2 dot array on a Tube^2 thin film by direct laser patterning. The array was *written* using a 532 nm laser at a power density of 50 mW/μm^2. Next, the Raman spectra were *read* using the same 532 nm laser at 0.5 mW/μm^2, which was lower than the critical power density required for annealing/writing. The Raman maps unambiguously confirm the recovery of the DWCNT characteristics, as evidenced by the recovery of the RBM$_{outer}$ and diminishing D peaks at the patterned dots. Adapted from ref. 144.

Building on this work, we determined that this annealing technique was selective to specific Tube^2 subpopulations whose inner tube was resonant with the laser wavelength and by using two different lasers that selectively excite metallic and semiconducting inner tubes, we show that both metallic and semiconducting patterns can be created, suggesting

a possible new path to overcome the critical barrier toward the practical realization of CNT electronics.

5.2. Results and Discussion

The outer tubes of DWCNTs were selectively functionalized with 4-nitrobenzenediazonium salt to the exclusion of the inner tube, as we previously reported,[62] to create the Tube^2 structure. The sodium dodecyl sulfate (SDS) surfactant that had been used to encapsulate and suspend the DWCNTs in aqueous solutions for the reaction was subsequently removed by vacuum filtration to make a thin film of the Tube^2 structures. The visible-NIR absorption spectra of the Tube^2 thin film confirmed that both the E_{11} and E_{22} inner tube absorption features remain after the diazonium reaction, while the outer tube E_{11} absorbance transition greatly diminished compared with the non-functionalized DWCNT control (Figure 5-1b), suggesting successful outer tube selective covalent functionalization.

Raman spectroscopy also corroborated this conclusion (Figure 5-1c). A DWCNT is composed of one single-walled carbon nanotube (SWCNT) nested within another; each tube giving rise to a unique set of Raman features, including the radial breathing modes (RBM, 100-350 cm^{-1}), the tangential mode (G peak, ~1590 cm^{-1}), and the disorder mode (D peak, ~1350 cm^{-1}). The DWCNTs used in this study have two sets of RBM, which are assigned to the outer (RBM_{outer}, 100-260 cm^{-1}, diameter ~1.61 nm) and inner tubes (RBM_{inner}, 260-350 cm^{-1}, diameter ~0.86 nm).[59] Upon covalent sidewall functionalization of the DWCNTs to create the Tube^2 structures, both the RBM_{outer} and G peak of the outer tube diminished, and the D peak intensity concomitantly increased due to the incorporation

of sp^3 defects on the outer tube. After annealing the Tube^2 structures using a laser (*a*-DWCNT), we observed the successful removal of the aryl groups from the outer tubes as shown by the recovery of the RBM_{outer} and G peak, as well as by the concomitant decrease of the D peak intensity (Figure 5-1c). Similar removal of aryl groups from Tube^2 structures were observed for bromo-terminated functional groups under the same annealing conditions (excitation wavelength, exposure time, and power density) demonstrating that this technique can be utilized to remove various functional groups.

The existence of a threshold power density can be partially understood by the balance of laser-induced heating and heat dissipation. The Tube^2 films convert photons to heat, while the substrate acts as a heat sink. We hypothesize that the sharp transition in Figure 5-2a is the point at which the energy absorbed by the Tube^2 thin film is balanced by heat dissipation. The energy at this point is the minimum power density needed to locally anneal the Tube^2 structure. When the laser power density is higher than the threshold energy, resonant excitation of the inner tubes anneals the outer tubes and the extent of annealing increases as a function of irradiation time.

We further observed that this annealing of functional groups from Tube^2 is unique to its structure. An experiment using a functionalized SWCNT (*f*-SWCNT) thin film of similar functional degree and tube density was used to explicitly demonstrate that the unfunctionalized inner tube within the Tube^2 structure is an essential part of the annealing process. After irradiation by a 532 nm laser under the same irradiation power and duration, Raman scattering showed that the Tube^2 sample recovered its outer tube RBM peak, while the *f*-SWCNT RBM remained flat (**Figure 5-4**), indicating that it was still functionalized and not annealed. We attribute this distinct difference to the presence of

non-functionalized inner tubes in the Tube^2 sample, which can be optically excited to allow the annealing process to occur, while the *f*-SWCNT could not be annealed because functionalization of the lone nanotube resulted in the loss of the optical transitions that were needed to facilitate resonance-enhanced annealing.

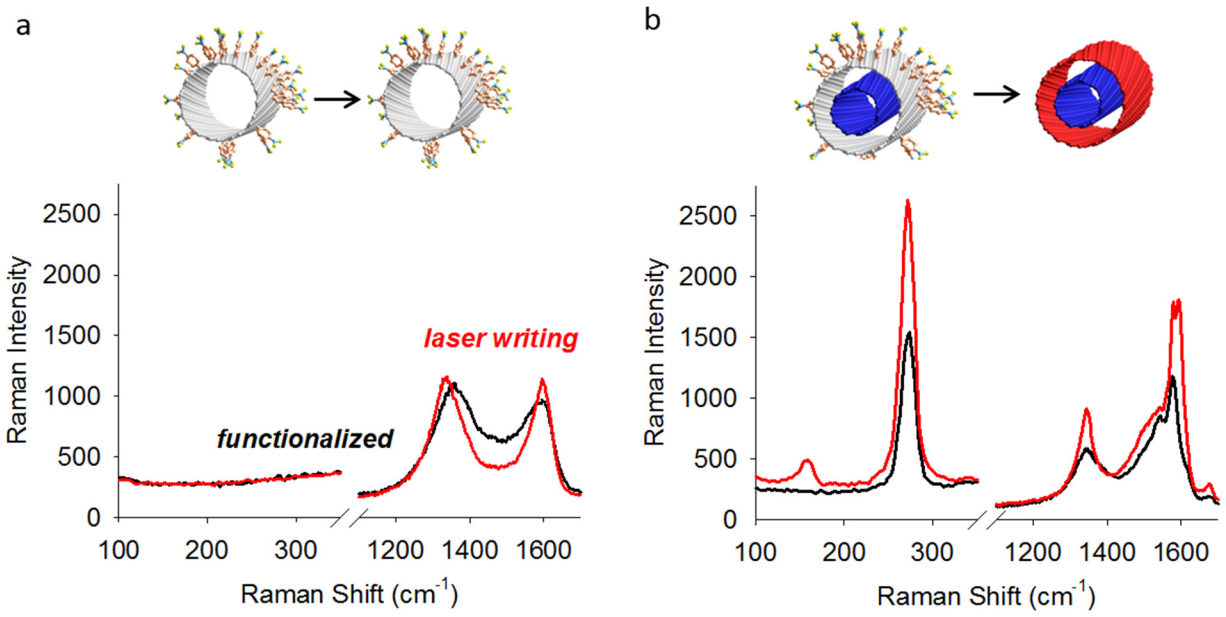

Figure 5-4. The Raman spectra of (a) *f*-SWCNT and (b) Tube^2 thin films before and after patterning with the 532 nm laser using the same irradiation time (50 s), irradiation power density (55 mW/μm^2), and tube density. Molecular models show the different response of the *f*-SWCNT and Tube^2 samples upon laser writing. Adapted from ref. 144.

The hypothesis that the unfunctionalized inner tube optical transitions are essential for this annealing technique is corroborated by evidence that only select outer tube diameter populations are annealed when a single inner tube chirality is excited (**Figure 5-5**). Each DWCNT has a pair of RBM peaks, whose Raman shift peak positions are from the outer

and inner tubes, respectively inversely related to tube diameter.[87,145] When creating the Tube^2 structures, the outer-walls of the DWCNTs are selectively functionalized, resulting in the RBM_{outer} peaks greatly diminishing, which suggests indiscriminate functionalization of all the outer tube chiralities. Based on the Kataura plot,[146] when these Tube^2 structures are annealed with a 532 nm laser, only the red-shaded RBM_{outer} (160 cm^{-1}) peak was restored while the grey-shaded RBM (147 cm^{-1}) peak was not.

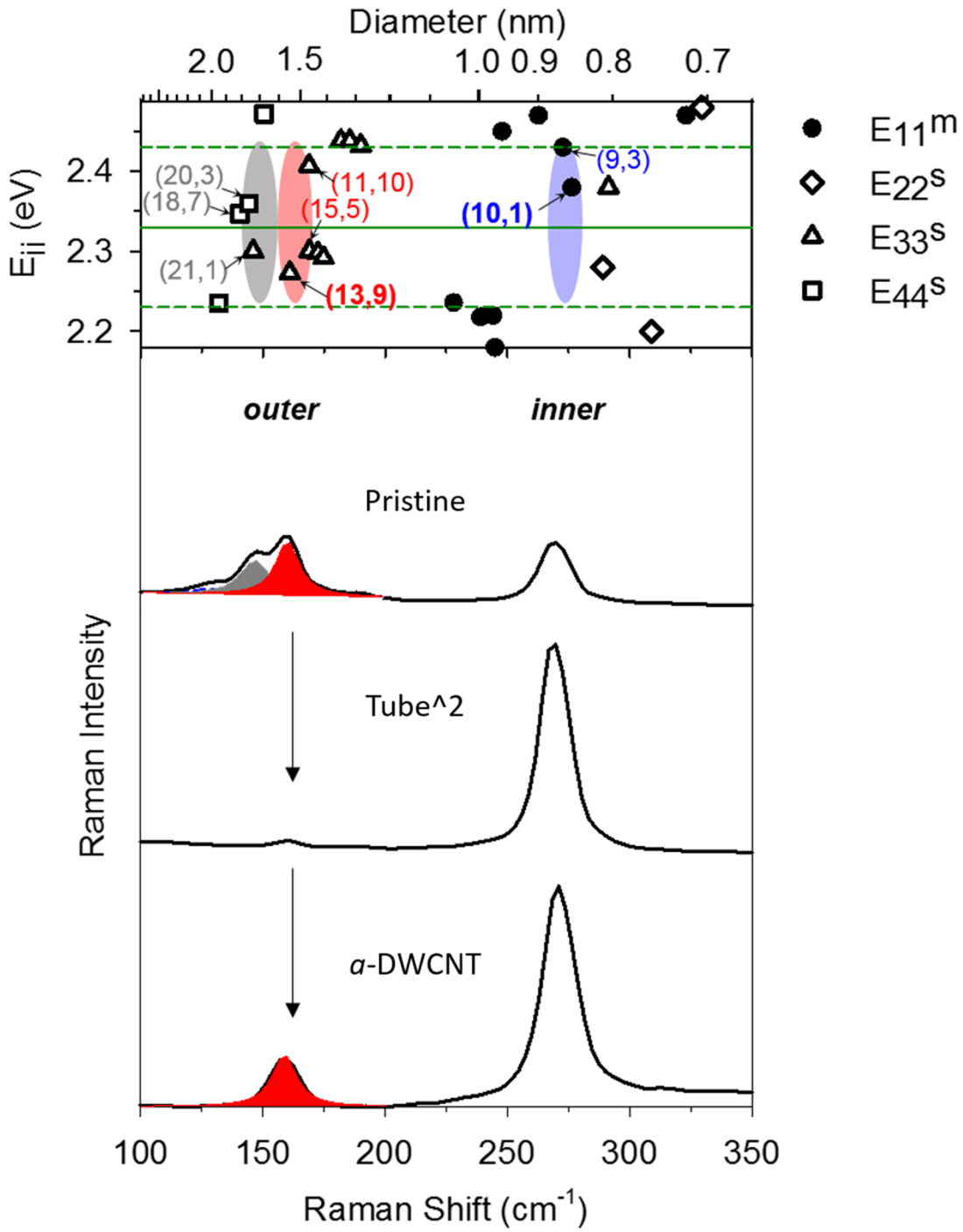

Figure 5-5. Raman spectral evidence of inner tube selectivity. The Raman spectra of the RBMs of pristine DWCNT, Tube^2, and *a*-DWCNT samples are shown. The top panel displays a Kataura plot in the resonant window of the 532 nm excitation. The laser excitation energy is marked by the solid green line, and the window of resonant

excitation is defined by the pair of dashed green lines. In the Raman spectra, the peak in the RBM_{outer} region was de-convoluted into two Lorentzian peak shapes, which are shaded in red and grey for clarity. The possible chiralities for each outer and inner tube peak are highlighted in the Kataura plot.

The reason behind this selective annealing of different outer tube diameter populations can be understood using our knowledge of the inter-tube separation distance of DWCNT and Tube^2 structures, which is equal to the van der Waals spacing of carbon (~0.36 nm).[59,61] The single Raman peak within the inner tube region, shaded in blue is located at 269 cm^{-1}, and can be assigned to (9,3) or (10,1) chiralities. However, the (9,3) inner tube is located at the very edge of the resonance window and is therefore expected to show low RBM peak intensity. As a result, we can assign the inner tube at 269 cm^{-1} to predominantly the (10,1) chirality, which has a diameter of 0.825 nm. Due to a fixed inter-wall spacing distance and inner tube diameter, the diameter of the outer-wall chiralities is roughly equal to the inner tube diameter plus twice the van der Waals spacing of carbon (0.72 nm). Therefore, the outer tube diameter associated with the (10,1) inner tube should be ~1.55 nm, which translates to an RBM_{outer} peak at 160 cm^{-1}. In Figure 3, the red-shaded RBM_{outer} peak that we observed in pristine DWCNTs and after the Tube^2 sample had been annealed also occurs at 160 cm^{-1}, therefore it appears that the outer tubes associated with this red-shaded peak are part of DWCNT structures which feature the (10,1) inner tube. This is strong evidence that for annealing of the outer tubes to occur, the inner tube nested within it must be optically excited. This conclusion is also corroborated by the lack of annealing of the grey-shaded outer tube populations (d ~ 1.68 nm), which are too large in

diameter to be part of a (10,1) inner tube-containing DWCNT structure, and therefore must contain inner tubes that are not optically resonant with the 532 nm laser wavelength. This can be observed by the absence of a peak at ~258 cm^{-1} (*i.e.*, the lack of a left shoulder for the RBM_{inner} peak), which would be the approximate inner tube peak position of the grey-shaded outer tubes, indicating that the inner tubes are optically transparent at 532 nm. Thus resonant excitation of these non-functionalized inner tubes cannot occur at 532 nm. We observed additional evidence of selective annealing of the outer tube in which the inner tube is excited by the synchronous increase of both inner and outer RBM intensity of the annealed structures.

We attribute the observed de-functionalization of the Tube^2 materials to thermal annealing effects.[147] Tour *et al.* have demonstrated with thermogravimetric analysis that the temperature needed to thermally detach aryl groups from the CNT lattice is 400 °C to 500 °C.[148] Although the exact temperature of the Tube^2 material upon annealing to *a*-DWCNTs is difficult to determine, several works have shown that a high power density laser, such as that is used here, is capable of heating CNTs to 300 °C to 800 °C.[149-150]

Additionally, the annealing exhibited a strong dependence on the Tube^2 film density. We found that at a higher nanotube film density, a lower power density was required to induce laser writing on the Tube^2 thin films. Additionally, denser Tube^2 thin films exhibited more difficulty in selectively annealing the intended outer tube chiralities, while thinner Tube^2 films were much easier to control, which we hypothesize to be a result of heat transfer within the nanotube network. At a higher nanotube density, more inner tubes are available to absorb and dissipate the heat with the laser, and there is also a greater amount of tube-tube interaction within the network, which results in a higher

chance of thermal cross-talk between the nanotubes to generate greater nonselective defunctionalization.[35] We also note that laser annealing of *f*-SWCNTs can occur at much higher power densities for denser films. However, not being a resonance excitation, annealing of the relatively more transparent *f*-SWCNT structures is much less efficient compared to inner tube resonant annealing in Tube^2 thin films.

We further explored this lithography technique using two different laser excitations: 532 nm and 633 nm. Using either the 532 nm or 633 nm laser, we wrote pathways on the Tube^2 films and then read both sets of patterns using 532 nm and 633 nm excitation lines at a lower power density (**Figure 5-6**). Both lasers are capable of exciting both the inner and outer tubes of the Tube^2 and *a*-DWCNT films. The result in Figure 5 demonstrates that only the Tube^2 structures with inner tubes that were in resonance with the laser were selectively de-functionalized, further corroborating that annealing occurs as a result of optical excitation of the inner tube. Additionally, after annealing/writing the Tube^2 thin film using the 532 nm laser, the outer tube RBM recovery was revealed by subsequently reading the pattern using the same 532 nm laser at a lower power density, though the pattern could not be observed when read with the 633 nm laser. Similarly, when the 633 nm laser was used for writing the Tube^2 sample, the recovered outer tube RBM only emerged when also read by the 633 nm laser.

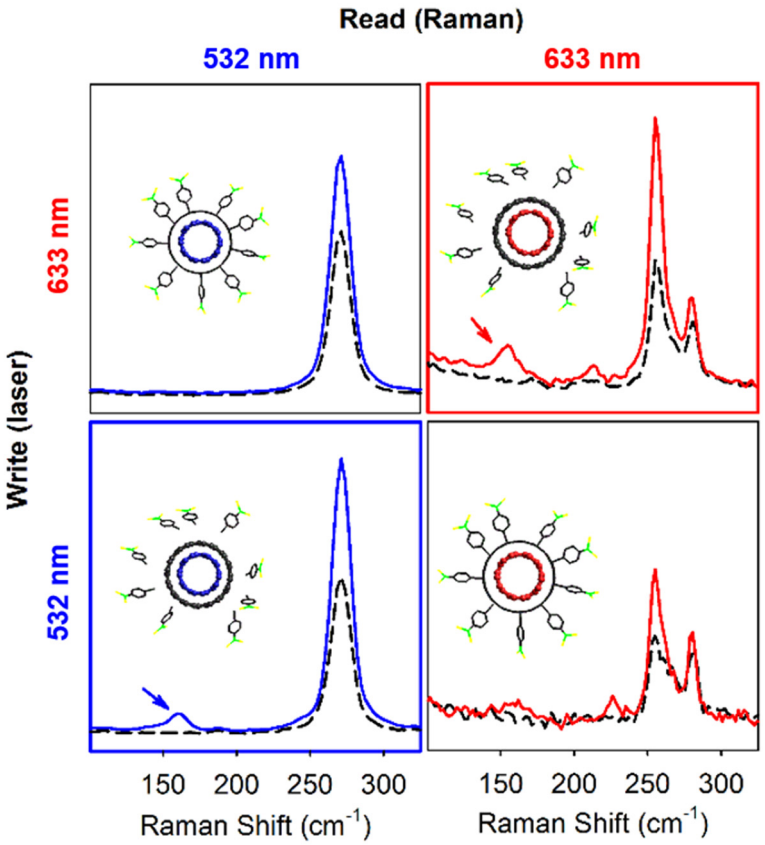

Figure 5-6. Optical patterning is specific to the inner tube electronic structure. The Tube^2 thin film was written with one laser and subsequently read using Raman spectroscopy. Two laser lines, 532 nm and 633 nm, were used for the writing and reading, resulting in 4 spectral combinations. In the Raman spectra, Tube^2 thin films were shown before (dashed lines) and after (solid lines) laser annealing. Adapted from ref. 144.

To demonstrate the potential application of this nanostructure lithography technique, we optically patterned conductive channels between Au electrodes with a channel length of 15 μm to create circuit arrays by direct-writing on insulating Tube^2 thin films using two lasers with wavelengths of 532 nm and 561 nm. Scanning electron

microscopy (SEM) images of these *a*-DWCNT circuits also revealed distinctly different conductance between the *written* and non-written areas of the thin film (**Figure 5-7**a,b). Successful creation of the line patterns were also evidenced by concomitant decrease in the D/G ratio and increase in the RBM_{outer} peaks of the patterned areas (Figure 5-7c), which was also observed from the dot arrays. Areas that had been exposed to the laser (*i.e.*, *a*-DWCNT) showed brighter contrast, indicative of higher conductivity than the non-exposed regions (*i.e.*, Tube^2), which is consistent with the recovery of the extended π-conjugated structure.

We further demonstrate that this lithography technique can be extended to more sophisticated patterns and larger scale using a photomask to pattern circuits of Tube^2. The circuit arrays are 100 μm wide with a 50 μm pitch perpendicular to the Au electrodes, and created in a facile and rapid fashion that mimics the resolution of photolithography patterned features without the use of a photoresist. The nanotubes in the masked areas of the Tube^2 film retain their functional groups and insulating properties, while the exposed areas become de-functionalized and conductive as evident by the contrast within SEM images between the interface of covered and exposed areas.

Conductance measurements show that the film was originally insulating with a conductivity 0.4 μS (Figure 5-7d, black open circles), which was attributed to the functional groups of the outer tube preventing the inter-tube contact needed for a conductive percolating pathway. Upon laser exposure, the Tube^2 structures within the patterned line were de-functionalized, allowing inter-tube contact between neighboring nanostructures. In this manner, we fabricated a 17 μm wide conductive pathway by laser writing. These patterned channels possessed a conductance of 87 μS, which is over a 200-fold

improvement in conductivity (Figure 6d, red filled circles). The conductance of the patterned channel increases linearly with the channel width (Figure 5-7e).

To further demonstrate the inner tube selectivity of this resonance-enhanced annealing and extend the applicability of this patterning technique to semiconducting features, we re-functionalize the de-functionalized channels with outer-wall selective functionalization. This re-functionalization removes the optical and electrical features of the outer tube again, but preserves the inter-tube contact created through laser annealing. By removing the electronic contributions of the outer wall through re-functionalization, the desired inner tube properties, which can be selected by laser wavelength excitation, dominate the overall electrical transport. Using a 532 nm laser, with the ability to selectively excite metallic inner tubes and a 561 nm laser that is resonant with semiconducting inner tube populations, we show that semiconducting and metallic lines can be drawn, respectively (Figure 5-7f). I_{SD}-V_g curves determined that predominantly metallic inner tube features (I_{ON}/I_{OFF} = 5) were created with the 532 nm laser, while p-type semiconducting inner tube (I_{ON}/I_{OFF} = 50) features were created upon annealing with the 561 nm laser. We anticipate based on the Kataura plot that the semiconducting selectivity can be significantly improved by using a laser with a longer wavelength although such a laser was currently not accessible to us.

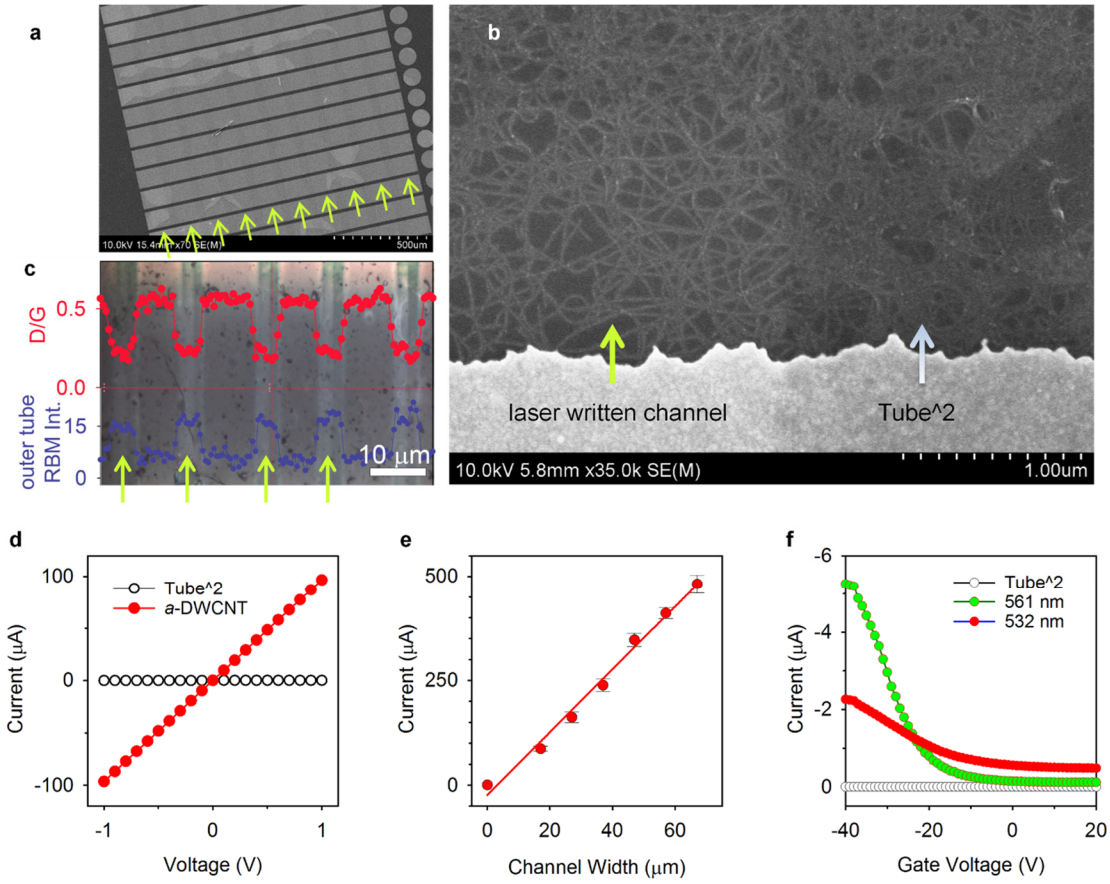

Figure 5-7. Conductive pathways generated by direct-write laser lithography. (a) An array of Tube^2 devices with the patterned conductive channels (15 μm × 100 μm) highlighted by arrows. (b) SEM image resolving laser written channel and insulating Tube^2 film. The laser used here is 561 nm. Adapted from ref. 144. (c) Periodic intensity profiles of the Raman D/G ratio and the RBM_{outer} peak intensity revealed for a Tube^2 film patterned using a 532 nm laser. A parallel array of written channels is shown, as indicated by the arrows. (d) I-V curves of a 17 μm wide channel on a Tube^2 film before and after laser writing and (e) current *vs.* channel width of the pathways written using a 532 nm laser. Adapted from ref. 144. (f) Transport characterization (V_{SD} = -0.1 V) of a Tube^2 film (black) and patterned circuits made with 561 nm (green) and 532 nm (red) lasers then re-functionalized.

5.3. Conclusions

We demonstrate that Tube^2 materials, which are tube-in-a-tube nanostructures, can be used to scalably pattern high resolution electronic features using a laser tuned to the resonance of the inner tubes in order to selectively desorb surface functional groups from the associated outer tubes. This phenomenon is unique to Tube^2 structures, and does not occur for their SWCNT counterparts under the same irradiation conditions. Power-dependence experiments reveal a sharp power threshold, below which de-functionalization does not occur. The selective desorption/annealing is attributed to laser-induced selective heating of the inner tubes, as evidenced by resonant Raman spectroscopy. This inner tube selectivity opens the opportunity to defunctionalize the outer tubes of the Tube^2 structures based on the optical properties of the inner tube. This phenomenon enables a novel laser lithography method for nanostructures, allowing direct-write patterning of both semiconducting channels and electrically conductive pathways on an insulating thin film made of Tube^2 materials.

5.4. Experimental Section

Preparation of DWCNT Solution: High-purity DWCNTs were separated from a CVD-grown sample (Unidym DW411UA) using density-gradient ultracentrifugation, as previously reported.[59] The sorted DWCNTs have an average diameter of 0.86 nm and 1.61 nm for the inner and outer tubes, respectively. 1 mL of the DWCNT solution was dialyzed (Spectra/Por Float-A-Lyzer G2 100 kDA) against 500 mL of 1 wt% SDS/water solution (freshly changed at 2 h, 12 h and 24 h) for a total of 48 h. The DWCNT solution was then diluted with and suspended in 1% SDS/water to a final concentration at which the optical absorbance (O.D.) was 0.2 @ 1000 nm.

Diazonium Salt Preparation and Synthesis of Tube^2 Solutions: 4-nitrobenzenediazonium tetrafluoroborate was synthesized and functionalized to the exclusion of the inner tube, as we previously reported.[62] The salts were stored at 4 °C, protected from light, and used within a week after synthesis. Exposure to light was limited by covering the vial with aluminum foil. Afterwards solutions were diluted to a tube density of 1 mg/L.

Creation of Insulating Tube^2 Film: Thin films were prepared using a vacuum filtration setup in which 1.5 mL of the diluted Tube^2 solution was created using a 47 mm Whatman Anodisc aluminum oxide membrane to filter out surfactants and unreacted reagents. Following filtration 500 mL of nanopure water was added to remove the residual surfactant. We then carefully loaded the Tube^2 thin film/AAO membrane in a petri dish containing 40 mL of 3 M sodium hydroxide (Sigma Aldrich) solution. The thin film was left in the sodium hydroxide solution for 15 min to dissolve the membrane, leaving the Tube^2 thin film floating in solution. The film was delicately transferred to fresh water 4 times to rinse the surface and afterwards picked with a clean substrate. The film was then dried on the substrate overnight at room temperature in vacuum. The film thickness could be tuned by controlling concentration and volume of the Tube^2 solution.

Device Fabrication: A 10 nm chromium adhesion layer and 50 nm gold deposited through electron beam deposition on a Tube^2 thin film transferred on an n-type silicon substrate with a 300 nm silicon oxide dielectric layer (Silicon Quest International). Photolithography was then used to pattern electrodes on the Tube^2 thin film, which were 100 μm long and 1500 μm wide, separated by 15 μm to define the channel length.

Annealing of Tube^2 Films: Tube^2 films were annealed in discrete spots using a laser with an exposure time of 50 s. The exposed laser power was tuned by changing the

percentage of the power output using optical filters. To pattern Tube^2 thin films, annealing was extended from spots to lines by annealing adjacent areas within a distance equal to half the laser spot size.

We patterned large-scale arrays of conductive pathways on Tube^2 thin films with the use of a 4" chrome photomask on glass (Front Range Photo Mask LLC) and a 561 nm Cobalt Jive laser. The photomask was clamped to the substrate after aligning it to circular patterned alignment markers at the sides of the electrodes. Patterned regions were perpendicular to the electrode arrays with a channel length of 15 μm in length, with exposed areas being 100 μm and 50 μm in width and pitch, respectively. To pattern areas larger than the spot size, the substrate and mask was moved along the XY plane of the pattern.

Characterization: Raman spectra and maps were collected on an Aramis model LabRAM Raman microscope (Horiba Jobin Yvon) using the available excitation lines, 633 nm and 532 nm. The output of the 633 nm and 532 nm lasers were 100 mW and 10 mW, respectively. The conditions for measuring (*i.e.*, *reading*) the Raman spectra included 1 s exposure time, 600 lines/mm grating, and 400 nm slit width. Absorption spectra were measured using a PerkinElmer Lambda 1050 UV-Vis-NIR spectrophotometer equipped with a photomultiplier tube (σ = 2.03% over 48 h of continuous use) and a broadband InGaAs detector (σ = 1.56% over 48 h of continuous use). The instrument was warmed up for 15 min prior to each use. Electrical measurements were performed using a Keithley 4200-SCS analyzer. For gated measurements, the devices were back-gated using the silicon substrate.

6. Fabrication of Functionalized Graphene/Semiconducting Single Walled Carbon Nanotube Hybrid Thin Films

6.1. Introduction

Atomically thick carbon nanomaterials, including carbon nanotubes (CNTs) and graphene, have generated enormous interest due to their interesting optical, electrical, and mechanical properties.[151-153] Aside from exceptional material properties, CNTs and graphene also possess large surface area for modification generating intrigue for additional functionality applications such as optical labels in bio-imaging,[8,137] drug delivery,[154,155] molecule detection,[12,13,156] polymer nanocomposites,[157,158] and electrode materials.[159] In particular, functionalized carbon nanomaterials have demonstrated the capability for detection, capturing and separation at molecular level, such as CNT-based field-effect transistor (FET) sensors[160-162] and graphene-based heavy metal sorbents.[163,164]

While promising, a major challenge for the application of these carbon nanomaterials is the incorporation of covalent functionalization that is required to provide functionality sufficient enough for practical needs without compromising their desired intrinsic properties.[48] Upon functionalization, the breaking of sp^2 geometry to sp^3 defects creates electron scattering sites resulting in removal of desirable optical and electrical properties of these carbon nanomaterials.[51,165,166] As an alternative, many state-of-the-art studies have demonstrated various techniques for passivating graphitic surfaces, such as by noncovalent functionalization[31,167] or extremely low covalent functional degrees[3,156] which provide incomplete protection of the sp^2 carbon lattice or minimal functionality, respectively. However, the functional group densities using these techniques are difficult

to control, which impacts the scalability and compatibility of these techniques for industrial commercialization.

Recently, our group developed a tube-in-a-tube (Tube^2) nanostructure from double walled carbon nanotubes (DWCNTs) combining unfunctionalized inner tube within a chemically modified outer tube for use as chemical sensors.[168] While the functionalized outer tube provides sufficient functional groups for molecular recognition, the unreacted inner tube retains its semiconducting characteristic just like individual single walled carbon nanotubes (SWCNTs). However, the complex purification process for DWCNTs may hinder the realization of the Tube^2 structure for practical use.[66] In the meantime, there has been growing interest in building of hybrid multi-dimensional carbon-based nanomaterials by combining their respective advantages, for instance, rebar graphene which utilizes CNT networks to reinforce the strength of graphene films,[169] and graphene-CNT carpets that exhibit superior conductivity and ultra-large surface area for high performance supercapacitors.[170,171]

In this work, we demonstrate the fabrication of a novel carbon based 2D-1D hybrid thin film comprised of semiconducting (6,5)-SWCNT (sSWCNT) networks protected by an atom-thick functionalized graphene layer (fG/sSWCNT). The hybrid structure is first created by assembling an unfunctionalized monolayer graphene sheet on top of a (6,5)-SWCNT thin film. Subsequently, using diazonium chemistry, we functionalized the top graphene layer to provide a high density of functional groups that can be used as probes for targeted molecular detection. Meanwhile, the sSWCNT networks beneath the graphene layer were protected from the diazonium functionalization reaction, and thus maintained their desirable semiconducting properties that are required for electrical transduction.

Because of this unique 2D-1D hybrid structure, the fabricated fG/sSWCNT thin film transistors (TFTs) featured a transistor ON/OFF ratio as high as 5400. When we used carboxylic acid groups as the functional moieties on the graphene surface, the fG/sSWCNT TFTs could act as chemical sensors toward the detection of aqueous ammonium cations (NH_4^+) with a low sensing limit of 250 nM in 1 mM ionic strength solution. The structural synthetic paradigm presented here that combines chemical functionalization with passivation may lead the way toward the fabrication of multidimensional functional materials for wider applications.

6.2. Results and Discussion

Figure 6-1 illustrates working mechanism and fabrication steps of fG/sSWCNT TFTs. (6,5) SWCNT were sorted by size-exclusion gel chromatography[66] and the thin film was prepared by a vacuum filtration[35], and monolayer graphene was grown on Cu foil through CVD process. Then, the SWCNT thin film and graphene were assembled together, and the resulting G/sSWCNT film was transferred onto the SiO_2/Si substrate for selective diazonium functionalization on the graphene coverage layer in order to obtain the fG/sSWCNT structure (for details see the experiment section). Due to the enhanced strength from CNT networks and strong graphitic interactions between components, the transfer of G/sSWCNT from Cu etchant solution to substrate did not need additional polymer protection, thus avoiding a potential source of contaminations.[35,169-172] Upon functionalization, the semimetallic graphene layer became insulating,[173] and the functional groups from diazonium reactant allowed specific absorption of certain chemical molecules. Meanwhile, the covered (6,5) SWCNT thin film was protected from reactants during

diazonium reaction, maintaining their desirable semiconducting properties. When the targeted molecules are attracted to the fG/sSWCNT surface, the interaction between the target molecule and the functional groups on graphene layer will modulate the local chemical gating conditions, causing the change of electrical properties of fG/sSWCNT that can be detected by the fabricated transistor device.

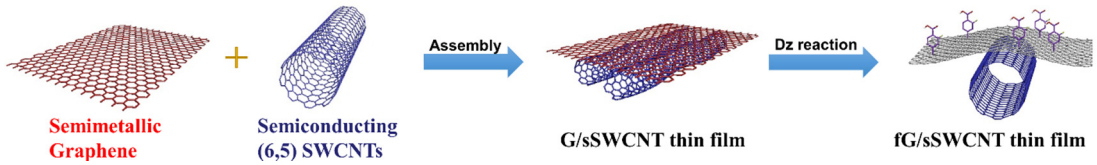

Figure 6-1. Schematic of the fabrication process to create fG/sSWCNT hybrid thin films.

The morphology of the G/sSWCNT hybrid thin film was first characterized using scanning electron microscopy (SEM) and transmission electron microscopy (TEM). The SEM image in **Figure 6-2**a shows a continuous graphene layer covering the sSWCNT thin film without noticeable breakage, indicating the successful transfer and high coverage of graphene across the substrate. At higher resolution, we can see small wrinkles in the graphene "blanket" (Figure 6-2b), which could be caused by variations in the underlying sSWCNT network. As a control, sSWCNT thin film without graphene coverage was also transferred to the SiO_2/Si substrate, and its SEM images show typical nanotube network morphology at the surface. The TEM image in Figures 6-2c further verifies the G/sSWCNT hybrid thin film structure, as it shows the graphene covering the sSWCNT network. The selected area electron diffraction (SAED) image taken at the same area (the inset of Figure 6-2c) confirms the hexagonal lattice structure from graphene, suggesting that the graphene layer maintains its high quality and integrity during the assembly and transfer of the G/sSWCNT thin film. While we observed sSWCNT bundles in the TEM images,

individual sSWCNTs could also be seen from the high-resolution TEM image, as shown in Figure 6-2d. This complete graphene coverage is crucial to the formation of the fG/sSWCNT hybrid structure, as it provides sufficient protection of the sSWCNTs underneath, preventing them from being covalently functionalized and losing their semiconducting characteristics.

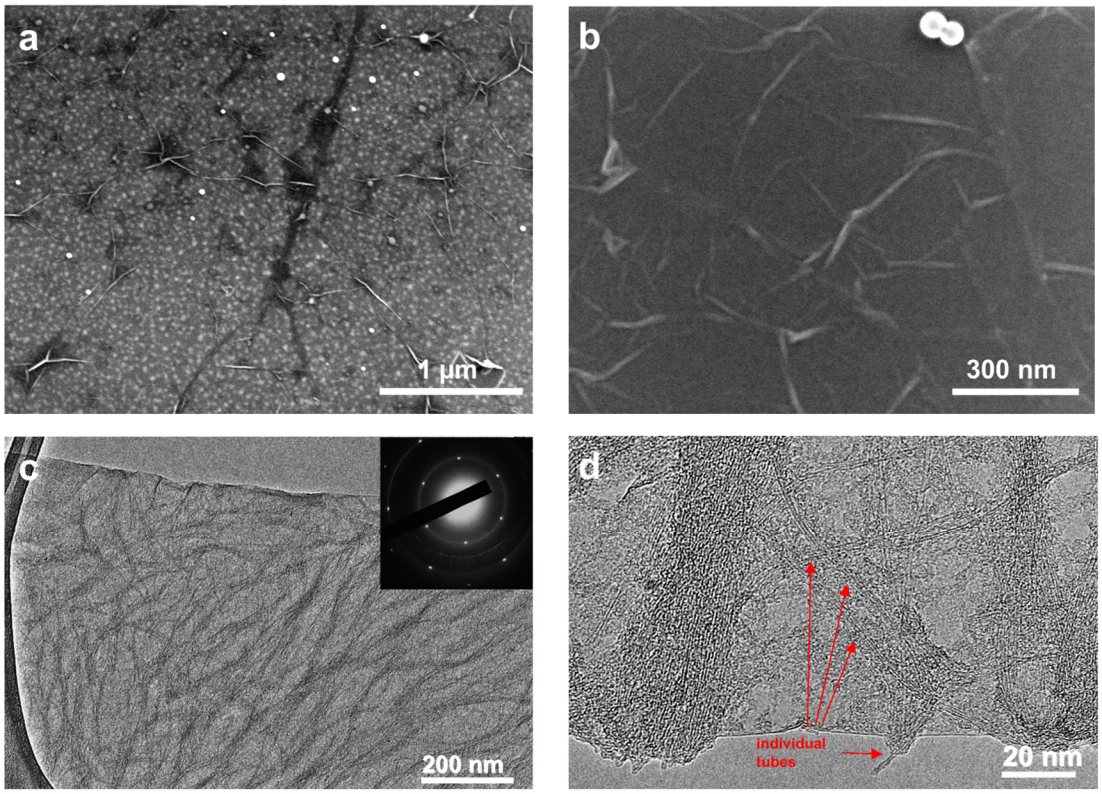

Figure 6-2. Morphology of the G/sSWCNT hybrid thin films. (a,b) SEM images of the G/sSWCNT thin films on the SiO_2/Si substrate. (c,d), TEM images of the G/sSWCNT thin films. The inset in (c) is the SAED images taken in the same region. The arrows in (d) indicate the individual nanotubes beneath the graphene layer.

Upon successful assembly of the hybrid G/sSWCNT thin film, diazonium chemistry was performed using 3-fluoro-4-carboxylbenzenediazonium to selectively

functionalize the top graphene layer with 2-fluorobenzoic acid terminal groups, a receptor that could be used for has molecular affinity to NH_4^+ or other amine molecules. Due to the extensive coverage of graphene over the CNT network, functionalization happens exclusively on graphene, while the underlying semiconducting (6,5) SWCNTs remain unreacted and their electrical properties preserved. The functional degree was first determined using Raman spectroscopy (**Figure 6-3**a) from the ratio between the D peak at ~1350 cm^{-1} originated from defect or symmetry broken sites and the G peak at ~1590 cm^{-1} originated from graphitic sp^2 carbon.[145] It was observed that the I_D/I_G peak ratio increased from 0.11 to 0.50 after functionalization of the G/sSWCNT film. On the contrary, when a control sample of sole graphene film was functionalized under the same reaction conditions, the I_D/I_G ratio increased to 1.9. This could be understood by the protected (6,5) SWCNTs that remain unreacted because of graphene coverage, thus they contribute to a higher G peak without any additional contributions to the D peak, resulting in a moderate I_D/I_G peak ratio in the fG/sSWCNT sample. Also, the domination of 2D peak contribution at ~2685 cm^{-1} from graphene layer in the G/sSWCNT sample was suppressed by the 2D peak contribution at ~2625 cm^{-1} from CNT thin film in the fG/sSWCNT sample after diazonium functionalization (Figure 6-3b), indicating that the covalent chemistry was occurring exclusive to the graphene layer. The successful functionalization was further confirmed from X-ray photoelectron spectroscopy (XPS) measurement as shown in Figure 6-3c. After reaction, fluorine and nitrogen elements are detected in the fG/sSWCNT film, a sign of attachment of fluorobenzoic acid functional groups onto the graphene surface. The comparison of C1s spectra before and after functionalization (Figure 6-3d) witnessed

the increase of C-C, C-F and COR contributions, again indicating the covalent bonding between functional groups and graphene.

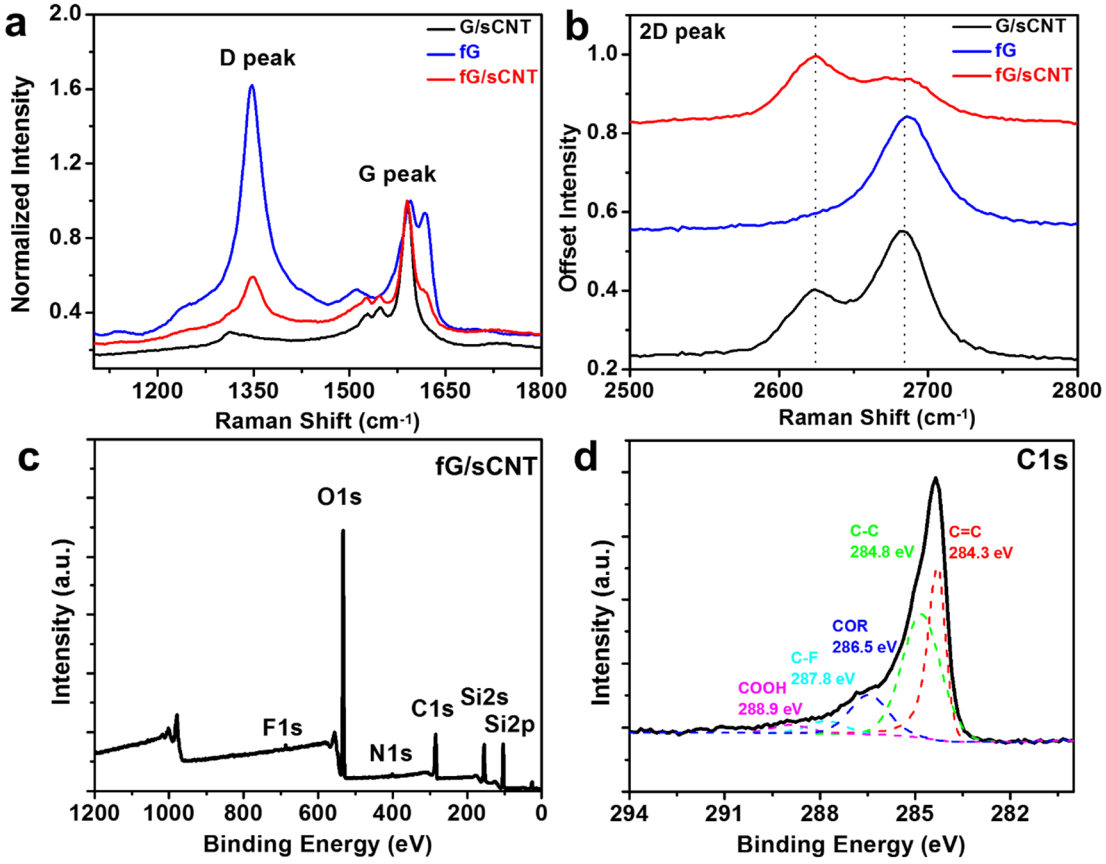

Figure 6-3. Characterization of fG/sSWCNT films. (a) Raman spectra of G/sSWCNT thin films before and after diazonium functionalization. Functionalized graphene film (fG) underwent same reaction conditions was presented as control. (b) Raman 2D peak comparison of G/sSWCNT, fG, and fG/sSWCNT samples. (c) XPS spectra of fG/sSWCNT thin film. (d) C1s XPS spectra of fG/sSWCNT thin film.

After synthesizing the fG/sSWCNT hybrid structure, we fabricated TFTs to characterize their transistor performance and used G/sSWCNT TFTs as a control (**Figure 6-4**a,b). Before the diazonium reaction, the electrical properties of the G/sSWCNT thin

film were dominated by the semi-metallic graphene, with an ON/OFF source-drain current (I_{SD}) ratio of 1.4 at a source-drain voltage (V_{SD}) of -0.5 V (Figure 6-4c,e). Upon functionalization, the resulting fG/sSWCNT thin film became semiconducting, as evidenced by the increased ON/OFF ratio to ~5400, which was three orders of magnitude enhancement (Figure 4d,f). Note that the absolute difference between the ON-current at a gate voltage (V_g) of -40 V and the OFF-current at V_g of 40 V in both the G/sSWCNT and fG/sSWCNT samples was approximately the same (~30 μA), indicating that covalent functionalization had caused the graphene layer to be insulating, while the sSWCNT network retained its semiconducting properties. The high ON/OFF ratio of the fG/sSWCNT was also a result of the pre-purification of the SWCNT source, which was primarily made up of single-chirality and semiconducting (6,5)-SWCNTs. Therefore, no additional electrical breakdown steps were needed to minimize the impact from metallic CNT impurities.[32] This high semiconducting purity of the resultant fG/sSWCNT hybrid thin film was further evidenced by the fact that the experimentally measured electrical properties of the fG/sSWCNT TFT were very similar to the corresponding theoretical calculations (**Figure 6-5**).

The resulting fG/sSWCNT hybrid thin film featured the combined properties of a pristine sSWCNT film, but was physically decorated with an insulating, functionalized graphene layer that could be tailored for specific applications. When compared to each component, either with or without functionalization (namely G, fG, (6,5)-SWCNTs, and functionalized (6,5)-SWCNTs), only the 2D-1D hybrid structure of the fG/sSWCNT material offered both a high ON/OFF ratio and a measurable ON-current, which could be beneficial for high-performance applications as sensors.

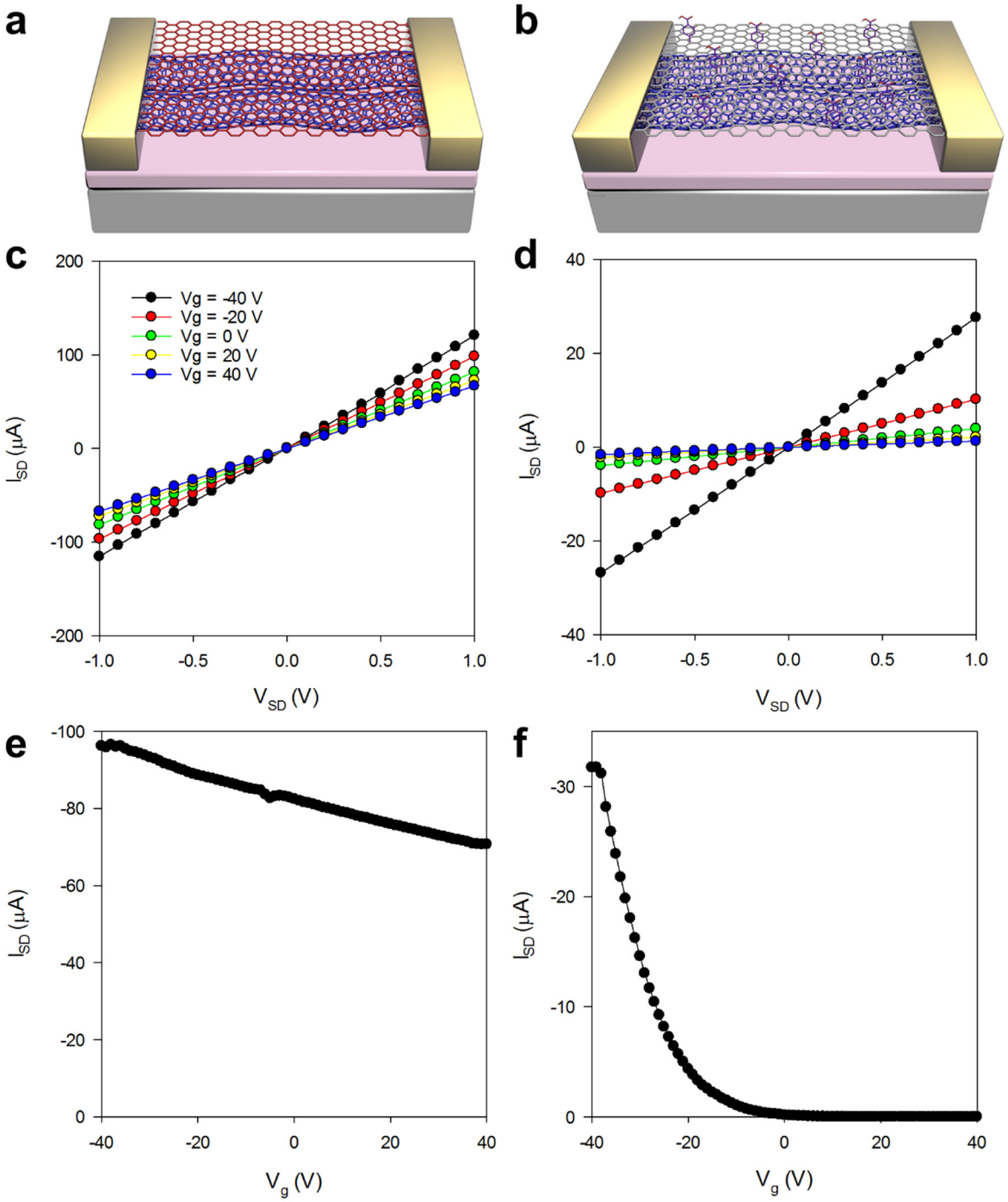

Figure 6-4. Electrical properties of G/sSWCNT and fG/sSWCNT thin films. The structures of the G/sSWCNT and fG/sSWCNT TFTs are shown in (a) and (b), respectively. The I_{SD}-V_{SD} curves of the (c) G/sSWCNT and (d) fG/sSWCNT TFTs are shown at different gate

voltages. The I_{SD} profiles of the (e) G/sSWCNT and (f) fG/sSWCNT TFTs are displayed at different V_g with a source-drain voltage (V_{SD}) of -0.5 V.

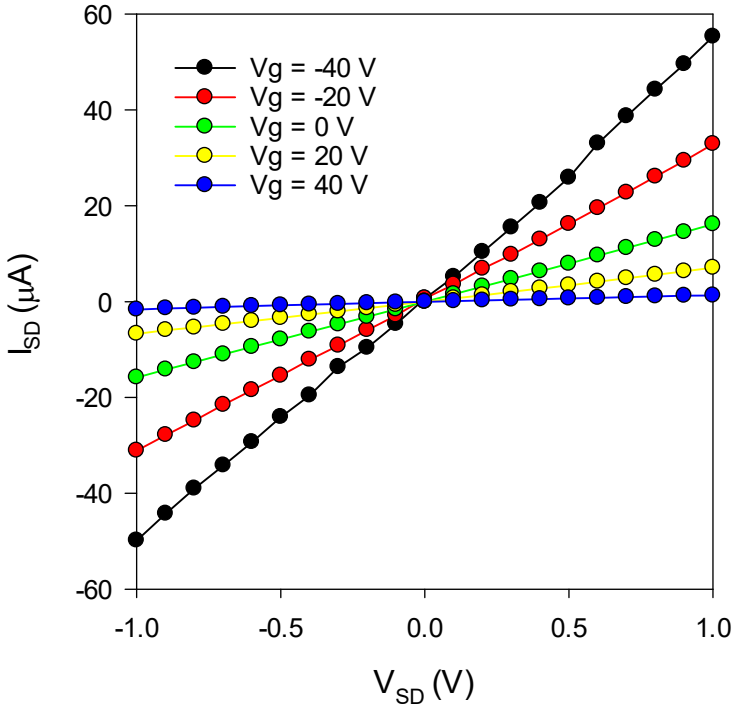

Figure 6-5. Theoretical calculations of fG/sCNT thin film electrical properties.

Due to a combination of the excellent transistor properties and high mobility of the sSWCNTs and a significantly high functional degree of the fG material, we found that fG/sSWCNT TFTs performed well as a platform for chemical sensing. The functional groups on the graphene surface are used to attract the analyte bringing it close to the hybrid film surface, while the underlying sSWCNT network detects the changes in the electronic environmental caused by the absorption of the targeted analyte molecules. When the analyte is attracted to the functional probes on the graphene surface, it modifies the chemical environment of the graphene, which accordingly modulates the electrical properties of the sSWCNTs via the strong π-π interactions between these materials,

generating correlated electrical signals that can be measured to calculate the analyte concentration. Thus, in the fG/sSWCNT TFT sensor, fG layer works as the sensing unit, while the sSWCNT network acts as the detection module.

To demonstrate this application, the as-fabricated fG/sSWCNT TFTs were tested for the detection of ammonium cations (NH_4^+) (**Figure 6-6**a). As shown in Figure 6-6b, in the device's ON-state at a V_g of -40 V, I_{SD} increased in correlation with a higher NH_4^+ concentration at the same V_{SD}. Note that at $V_{SD} > 0.7$ V, side reactions started to occur, which caused the nonlinear response in the I_{SD}-V_{SD} curves. Therefore, we chose a V_{SD} of 0.7 V as the working voltage and plotted the change in I_{SD} (ΔI_{SD}) at various NH_4^+ concentrations in Figure 6-6c. When we measured the fG/sSWCNT electrical response as a function of the logarithm of the NH_4^+ concentration (Figure 6-6d), the fG/sSWCNT sensors showed high affinity to NH_4^+ comparable with our previously reported Tube^2 sensors that utilize similar sensing transducers as well as other state-of-the-art NH_4^+ nanosensors.[174-176] Comparatively, the fG/sSWCNT sensors showed a similar relative change in conductance as a function of the NH_4^+ concentration, which is indicative of similar sensing mechanisms, but possessed higher absolute change in operating current[27] that allowed our fG/sSWCNT-based sensors to detect NH_4^+ down to a limit of 250 nM in solutions of millimolar ionic strengths.

This high and sensitive ON-state conductance response of the fG/sSWCNT sensing device stems from the use of highly purified (6,5)-SWCNTs with superior semiconducting properties, as well as the atom-thick and impermeable monolayer graphene cover, which provides the large surface area needed for sufficient functionalization as well as passivation of the underlying sSWCNTs in order to ensure that they maintain their semiconducting

electrical response. As a result, the fG/sSWCNT hybrid structure combines highly functionalized graphene as the sensing interface for maximum molecule detection and an unreacted semiconducting (6,5)-SWCNT network as the semiconductor for generating a high-sensitivity detection signal. With the freedom to attach functional groups other than carboxylic acids onto graphene, fG/sSWCNT-based TFTs could also be designed for the detection of other targeted chemical species, rendering the fG/sSWCNT hybrid structure as a promising candidate for high-performance chemical and biological sensors.

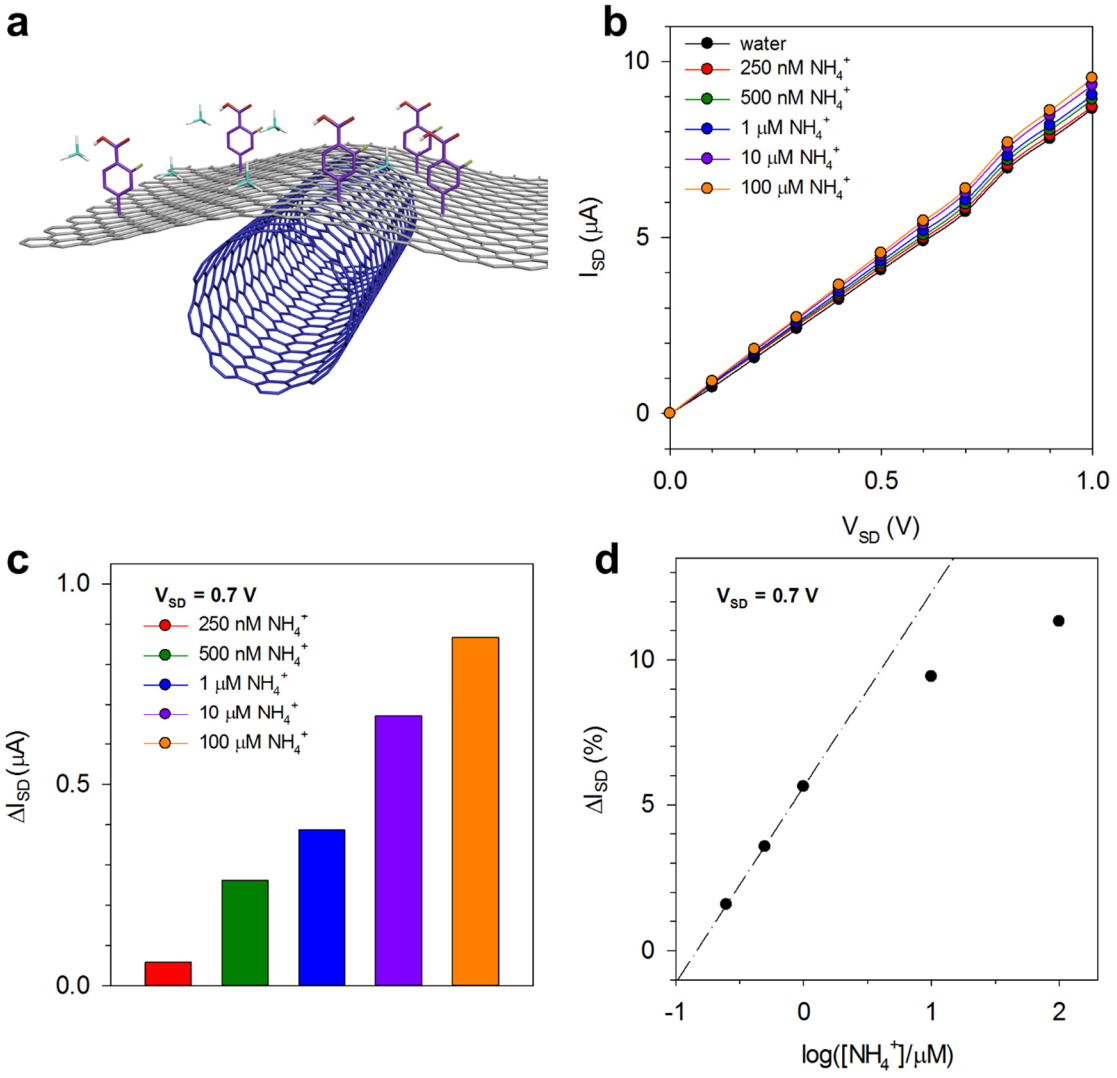

Figure 6-6. Application of the fG/sSWCNT thin films as chemical sensors. (a) Schematic demonstrating the sensing mechanism of fG/sSWCNT-based sensors. (b) I_{SD}-V_{SD} curves of fG/sSWCNT TFTs with various NH_4^+ concentrations. V_g was set at -40 V. (c) ΔI_{SD} with various NH_4^+ concentrations. V_g was set at -40 V, and V_{SD} was set at 0.7 V. (d) ΔI_{SD} as a function of $\log([NH_4^+]/\mu M)$. V_g was set at -40 V, and V_{SD} was set at 0.7 V.

6.3. Conclusion

In summary, we have prepared a novel 2D-1D hybrid thin film by selectively functionalizing graphene with diazonium chemistry and simultaneously using this layer to protect the graphitic integrity of the underlying SWCNT network to preserve its semiconducting properties. TFTs made from fG/sSWCNT materials exhibited a high ON/OFF current ratio of ~5400 and featured high sensitivity toward the detection of NH_4^+ ions with a detection limit as low as 250 nM. Such high performance is a result of the unique features of the fG/sSWCNT hybrid structure that combine a high functional degree from the graphene layer for molecular recognition and superior semiconducting properties from the highly purified single-chirality SWCNT network. The realization of this novel carbon-based hybrid thin film not only shows high potential as a functional material for next-generation scalable electronics and sensors, but may also provide a new strategy for the utilization of various carbon nanomaterials in wider applications, such as energy generation and storage nanodevices.

6.4. Experimental Details

Growth of Monolayer Graphene. Monolayer graphene films were grown by a standard CVD system using research grade CH_4 as the carbon feedstock and ultrahigh purity H_2 as the reduction gas. A 25-μm-thick Cu foil (99.8% purity, Alfa Aesar) was first loaded into cool zone of the tubular furnace and the reaction chamber was evacuated to ~10 mTorr for 10 min. Then 300 sccm H_2 was introduced into the CVD chamber with a pressure of ~0.9 Torr and the temperature was increased to 1050 ˚C. After stabilization, the Cu foil was quickly moved to the hot zone and annealed for 20 min. After that, the temperature was lowered down to 1000 ˚C, and 11 sccm CH_4 was introduced into the system while keeping the H_2 flow at 300 sccm for 15 min. After the growth, CH_4 flow was turned off and the Cu foil was quickly removed out of the hot zone to cool down to room temperature.

Generation of (6,5) SWCNT Thin Film. The semiconducting (6,5)-SWCNTs were sorted using gel chromatography on a Sephacryl S-200 HR column (GE Healthcare) as previously reported.[3] (6,5) solutions in 1% wt.% SDS were diluted using 1% SDS to a concentration of ~1 mg/L (OD @ 561 nm ~ 0.18). 2 mL of the diluted solutions added to 47 mm nitrocellulose filter membranes with a 50 nm pore size (Millipore VMWP) and the thin films created using a vacuum filtration method.[35] Films were then dried in room temperature under vacuum overnight.

Generation of G/sSWCNT Hybrid Film. The (6,5) SWCNT thin film on nitrocellulose was first transferred onto graphene on the Cu foil by applying heat and pressure. The nitrocellulose was then dissolved using acetone and then the G/sSWCNT film on copper was sequentially rinsed with isopropyl alcohol, ethanol, and water, and then annealed at 200 ˚C evaporate any residual solvents. Then, the backside of the Cu foil was exposed to UV-ozone for 10 min to break the graphene film on this side. 0.1 M $(NH_4)_2S_2O_8$ solution

was then employed to etch away Cu, allowing G/sSWCNT film to float on the solution. The G/sSWCNT film was carefully picked up by a glass slide and transferred onto DI water several times for cleaning, and finally picked up onto SiO_2/Si substrate upside down. Then the substrate with G/sSWCNT film was dried in a vacuum oven at ~50 Torr and 60 ˚C overnight and annealed in a CVD chamber with 200 sccm Ar at 300 ˚C for 1 h.

Device Fabrication and Functionalization. Electrodes (50 μm × 50 μm) consisted of a 10 nm chromium adhesion layer, 100 nm gold layer, and a 125 nm silicon oxide passivation layer were deposited through electron beam deposition with a device channel length and width of 10 μm and 50 μm, respectively, onto the G/sSWCNT thin film area on the SiO_2/Si substrate. The as-made G/sSWCNT transistor arrays were then functionalized by immersion in 100 mM 3-fluoro-4-carboxylbenzenediazonium tetrafluoroborate for 1 day.

fG/sSWCNT Sensor Detection. NH_4^+ solutions were prepared through the dissolution of NH_4Cl in water. NaCl was added to the solutions to adjust the ionic strength of each solution to 1 mM to control the effect of Debye screening. 0.5 μL of analyte solutions are added between the transistor area using a micropipette and electrical measurements characterized after the conductivity stabilizes.

Characterization. SEM measurement was done on a Hitachi SU-70 Schottky field emission SEM using an acceleration voltage of 10.0 kV. TEM measurement was done on a JEM 2100 LaB_6 TEM using acceleration voltage of 200 kV. Raman spectra were collected on a Horiba Jobin Yvon LabRAM Raman microscope (model: ARAMIS) with an excitation line of 532 nm. XPS measurement was done on a high sensitivity Kratos AXIS 165 spectrometer. Electrical properties were measured using a Cascade probe station equipped with an Keithley-4200 SCS semiconductor parameter analyzer.

7. Conclusions and Outlooks

Tube^2, created through the outer wall selective covalent functionalization of its precursor double-walled carbon nanotubes, possesses a variety of exceptional features that include high performance sensing, electrode free gating, and chiral-specific patterning. Utilization of chemistries with high efficiency and functional densities greatly enhance the applicability and performance of Tube^2 devices allowing them to overcome fundamental challenges associated with CNTs. Further gains in transistor performance can be achieved through electrical breakdown of metallic Tube^2 structures. Tube^2 TFT were fabricated with ON/OFF ratio of over 20000 for devices in which the channel length was 20 times the length of the average structure length. Tube^2 semiconductors fabricated as circuits for TFTs demonstrated concomitant high sensitivity and selectivity as a small molecule sensor for ammonia. Similar sensitivity and selectivity was achieved for the detection of oligonucleotides that included a 123-base tuberculosis biomarker and discrimination of single base mismatches. Furthermore, it was determined for that chemical gating was a dominant sensing mechanism for semiconducting Tube^2 structures, which enabled the concept of using attached groups to significantly gate the structure. Without the utilization of a physical gate terminal, Tube^2 TFTs could be turned to the linear ON-state through the use of chemically attached groups.

Owing to their unique structure and retained properties, a film of Tube^2 can also be easily patterned using a laser resonant to its inner tube, allowing for selective electronic type defunctionalization through localized thermal dissipation. Using laser with excitation wavelengths resonant with semiconducting or metallic inner tube chiralities, circuits of either electronic type can be created.

Due to these unique features, Tube^2, and its thin film analog fG/sSWCNT, is a promising material that may pave avenues for next generation functional materials, device innovation, and high performance electronics. Development of chemistries that can increase the functional degree without sacrificing the versatility offered through diazonium chemistry may result in further enhancement in chemical gating effects, passivation of functional shell surface, and receptor packing density. Using two lasers that are resonant with semiconducting and metallic wavelengths, Tube^2 lithography can be potentially used as a high throughput technique for IC creation and applications that include sensor arrays. Furthermore, the ability of Tube^2 transistors to be turned ON without a gate provides opportunities to simplify device configuration greatly, opening up possibilities innovative two-terminal platforms that may include printable lab-on-a-chip Tube^2 devices.

8. References

1. Iijima, S. *Nature* **1991**, *354*, 56.
2. Riggs, J. E.; Guo, Z. X.; Carroll, D. L.; Sun, Y. P. *J. Am. Chem. Soc.* **2000**, *122*, 5879.
3. Piao, Y.; Meany, B.; Powell, L. R.; Valley, N.; Kwon, H.; Schatz, G. C.; Wang, Y. *Nat. Chem.* **2013**, *5*, 840.
4. Wildoer, J. W. G.; Venema, L. C.; Rinzler, A. G.; Smalley, R. E.; Dekker, C. *Nature* **1998**, *391*, 59.
5. Durkop, T.; Getty, S. A.; Cobas, E.; Fuhrer, M. S. *Nano Lett.* **2004**, *4*, 35.
6. Yu, M. F.; Files, B. S.; Arepalli, S.; Ruoff, R. S. *Phys. Rev. Lett.* **2000**, *84* (24), 5552.
7. Yu, M. F.; Lourie, O.; Dyer, M. J.; Moloni, K.; Kelly, T. F.; Ruoff, R. S. *Science* **2000**, *287*, 637.
8. Liu, Z.; Tabakman, S.; Welsher, K.; Dai, H. *Nano Res.* **2009**, *2*, 85.
9. Welsher, K.; Liu, Z.; Daranciang, D.; Dai, H. *Nano Lett.* **2008**, *8*, 586.
10. Choi, Y. K.; Moody, I. S.; Sims, P. C.; Hunt, S. R.; Corso, B. L.; Perez, I.; Weiss, G. A.; Collins, P. G. *Science* **2012**, *335*, 319.
11. Peng, G.; Trock, E.; Haick, H. *Nano Lett.* **2008**, *8*, 3631.
12. Kong, J.; Franklin, N. R.; Zhou, C. W.; Chapline, M. G.; Peng, S.; Cho, K. J.; Dai, H. J. *Science* **2000**, *287*, 622.
13. Huang, J.; Ng, A. L.; Piao, Y. M.; Chen, C. F.; Green, A. A.; Sun, C. F.; Hersam, M. C.; Lee, C. S.; Wang, Y. H. *J. Am. Chem. Soc.* **2013**, *135*, 2306.
14. Shulaker, M. M.; Hills, G.; Patil, N.; Wei, H.; Chen, H. Y.; Philip Wong, H. S.; Mitra, S. *Nature* **2013**, *501*, 526.

15. Edwards, B. C. *Acta Astronaut.* **2000**, *47*, 735.

16. Baughman, R. H.; Zakhidov, A. A.; de Heer, W. A. *Science* **2002**, *297*, 787.

17. Dalton, A. B.; Collins, S.; Munoz, E.; Razal, J. M.; Ebron, V. H.; Ferraris, J. P.; Coleman, J. N.; Kim, B. G.; Baughman, R. H. *Nature* **2003**, *423*, 703.

18. O'Connell, M. J.; Bachilo, S. M.; Huffman, C. B.; Moore, V. C.; Strano, M. S.; Haroz, E. H.; Rialon, K. L.; Boul, P. J.; Noon, W. H.; Kittrell, C.; Ma, J. P.; Hauge, R. H.; Weisman, R. B.; Smalley, R. E. *Science* **2002**, *297*, 593.

19. Bachilo, S. M.; Strano, M. S.; Kittrell, C.; Hauge, R. H.; Smalley, R. E.; Weisman, R. B. *Science* **2002**, *298*, 2361.

20. Saito, R.; Dresselhaus, G.; Dresselhaus, M. S. *Physical Properties of Carbon Nanotubes*; Imperial College Press: London, 1998; pp. 1–38.

21. Moore, K. E.; Tune, D. D.; Flavel, B. S. *Adv. Mater.* **2015**, *27*, 3105.

22. Avouris, P.; Appenzeller, J.; Martel, R.; Wind, S. J. *Proc. IEEE* **2003**, *91*, 1772.

23. Liu, K. H.; Wang, W. L.; Xu, Z.; Bai, X. D.; Wang, E. G.; Yao, Y. G.; Zhang, J.; Liu, Z. F. *J. Am. Chem. Soc.* **2009,** *131*, 62.

24. Terrones, M.; Grobert, N.; Olivares, J.; Zhang, J. P.; Terrones, H.; Kordatos, K.; Hsu, W. K.; Hare, J. P.; Townsend, P. D.; Prassides, K.; Cheetham, A. K.; Kroto, H. W.; Walton, D. R. M. *Nature* **1997,** *388*, 52.

25. Hilding, J.; Grulke, E. A.; Zhang, Z. G.; Lockwood, F. *J. Dispersion Sci. Technol.* **2003**, *24*, 1.

26. Matarredona, O.; Rhoads, H.; Li, Z. R.; Harwell, J. H.; Balzano, L.; Resasco, D. E. *J. Phys. Chem. B* **2003**, *107*, 13357.

27. Strano, M. S.; Moore, V. C.; Miller, M. K.; Allen, M. J.; Haroz, E. H.; Kittrell, C.; Hauge, R. H.; Smalley, R. E. *J. Nanosci. Nanotechnol.* **2003**, *3*, 81.

28. Kapralov, A. A.; Feng, W. H.; Amoscato, A. A.; Yanamala, N.; Balasubramanian, K.; Winnica, D. E.; Kisin, E. R.; Kotchey, G. P.; Gou, P. P.; Sparvero, L. J.; Ray, P.; Mallampalli, R. K.; Klein-Seetharaman, J.; Fadeel, B.; Star, A.; Shvedova, A. A.; Kagan, V. E. *ACS Nano* **2012**, *6*, 4147.

29. Nilsson, H. M.; Meany, B.; Ticey, J.; Sun, C. F.; Wang, Y. H.; Cumings, J. *Langmuir* **2015**, *31*, 6948.

30. Pan, B.; Xing, B. S. *Environ. Sci. Technol.* **2008**, *42*, 9005.

31. Chen, R. J.; Bangsaruntip, S.; Drouvalakis, K. A.; Kam, N. W. S.; Shim, M.; Li, Y.; Kim, W.; Utz, P. J.; Dai, H. *Proc. Natl. Acad. Sci.* **2003**, *100*, 4984.

32. Kingrey, D.; Khatib, O.; Collins, P. G. *Nano Lett.* **2006**, *6*, 1564.

33. Collins, P. G.; Bradley, K.; Ishigami, M.; Zettl, A. *Science* **2000**, *287*, 1801.

34. Avouris, P. *Chem. Phys.* **2002**, *281*, 429.

35. Ng, A. L.; Sun, Y.; Powell, L.; Sun, C. F.; Chen, C. F.; Lee, C. S.; Wang, Y. *Small* **2015**, *11*, 96.

36. Wang, C. A.; Zhang, J. L.; Zhou, C. W. *ACS Nano* **2010**, *4*, 7123.

37. Montoro, L. A.; Matsubara, E. Y.; Rosolen, J. M. *J. Power Sources* **2014**, *257*, 205.

38. Ding, L.; Tselev, A.; Wang, J. Y.; Yuan, D. N.; Chu, H. B.; McNicholas, T. P.; Li, Y.; Liu, J. *Nano Lett.* **2009**, *9*, 800.

39. Li, Y. M.; Mann, D.; Rolandi, M.; Kim, W.; Ural, A.; Hung, S.; Javey, A.; Cao, J.; Wang, D. W.; Yenilmez, E.; Wang, Q.; Gibbons, J. F.; Nishi, Y.; Dai, H. J. *Nano Lett.* **2004**, *4*, 317.

40. Arnold, M. S.; Green, A. A.; Hulvat, J. F.; Stupp, S. I.; Hersam, M. C. *Nat. Nanotechnol.* **2006**, *1*, 60.

41. Ghosh, S.; Bachilo, S. M.; Weisman, R. B. *Nat. Nanotechnol.* **2010**, *5*, 443.

42. Liu, H. P.; Nishide, D.; Tanaka, T.; Kataura, H. *Nat. Commun.* **2011**, *2*, 8.

43. Flavel, B. S.; Kappes, M. M.; Krupke, R.; Hennrich, F. *ACS Nano* **2013**, *7*, 3557.

44. Zheng, M.; Jagota, A.; Semke, E. D.; Diner, B. A.; McLean, R. S.; Lustig, S. R.; Richardson, R. E.; Tassi, N. G. *Nat. Mater.* **2003**, *2*, 338.

45. Ao, G. Y.; Khripin, C. Y.; Zheng, M. *J. Am. Chem. Soc.* **2014**,*136*, 10383.

46. Strano, M. S.; Dyke, C. A.; Usrey, M. L.; Barone, P. W.; Allen, M. J.; Shan, H. W.; Kittrell, C.; Hauge, R. H.; Tour, J. M.; Smalley, R. E. *Science* **2003**, *301*, 1519.

47. Banerjee, S.; Hemraj-Benny, T.; Wong, S. S. *Adv. Mater.* **2005**, *17*, 17.

48. Wang, F.; Swager, T. M. *J. Am. Chem. Soc.* **2011**, *133*, 11181.

49. Chen, J.; Liu, H. Y.; Weimer, W. A.; Halls, M. D.; Waldeck, D. H.; Walker, G. C. *J. Am. Chem. Soc.* **2002**, *124*, 9034.

50. Nakashima, N.; Tomonari, Y.; Murakami, H. *Chem. Lett.* **2002**, 6, 638.

51. Bahr, J. L.; Tour, J. M. *J. Mater. Chem.* **2002**, *12*, 1952.

52. Brozena, A. H.; Moskowitz, J.; Shao, B. Y.; Deng, S. L.; Liao, H. W.; Gaskell, K. J.; Wang, Y. H. *J. Am. Chem. Soc.* **2010**, *132*, 3932.

53. Dong, X. C.; Lau, C. M.; Lohani, A.; Mhaisalkar, S. G.; Kasim, J.; Shen, Z. X.; Ho, X. N.; Rogers, J. A.; Li, L. J. *Adv. Mater.* **2008**, *20*, 2389.

54. Lee, S. W.; Kim, B.-S.; Chen, S.; Shao-Horn, Y.; Hammond, P. T. *J. Am. Chem. Soc.* **2009**, *131*, 671.

55. Liu, Y.; Wu, D. C.; Zhang, W. D.; Jiang, X.; He, C. B.; Chung, T. S.; Goh, S. H.; Leong, K. W. *Angew. Chem. Int. Ed.* **2005**, *44*, 4782.

56. Goldsmith, B. R.; Coroneus, J. G.; Khalap, V. R.; Kane, A. A.; Weiss, G. A.; Collins, P. G. *Science* **2007**, *315*, 77.

57. Endo, M.; Muramatsu, H.; Hayashi, T.; Kim, Y. A.; Terrones, M.; Dresselhaus, N. S. *Nature* **2005**, *433*, 476.

58. Qi, H.; Qian, C.; Liu, J. *Nano Lett.* **2007**, *7*, 2417.

59. Green, A. A.; Hersam, M. C. *Nat. Nanotechnol.* **2009**, *4*, 64.

60. Green, A. A.; Hersam, M. C. *ACS Nano* **2011**, *5*, 1459.

61. Shen, C.; Brozena, A. H.; Wang, Y. *Nanoscale* **2011**, *3*, 503.

62. Piao, Y. M.; Chen, C. F.; Green, A. A.; Kwon, H.; Hersam, M. C.; Lee, C. S.; Schatz, G. C.; Wang, Y. H. *J. Phys. Chem. Lett.* **2011**, *2*, 1577.

63. Bouilly, D.; Cabana, J.; Meunier, F.; Desjardins-Carriere, M.; Lapointe, F.; Gagnon, P.; Larouche, F. L.; Adam, E.; Paillet, M.; Martel, R. *ACS Nano* **2011**, *5*, 4927.

64. Tseng, C. H.; Wang, C. C.; Chen, C. Y. *Chem. Mater.* **2007**, *19*, 308.

65. Lopez-Bezanilla, A. *J. Phys. Chem. C* **2014**, *118*, 1472.

66. Lilienfield, J. E. Method and Apparatus for Controlling Electric Currents. U. S. Patent 1,745,175, Jan. 28 1930.

67. Tanenbaum, M.; Valdes, L. B.; Buehler, E.; Hannay, N. B. *J. Appl. Phys.* **1955**, *26*, 686.

68. Caras, S.; Janata, J. *Anal. Chem.* **1980**, *52*, 1935.

69. Rothberg, J. M.; Hinz, W.; Rearick, T. M.; Schultz, J.; Mileski, W.; Davey, M.; Leamon, J. H.; Johnson, K.; Milgrew, M. J.; Edwards, M.; Hoon, J.; Simons, J. F.; Marran, D.; Myers, J. W.; Davidson, J. F.; Branting, A.; Nobile, J. R.; Puc, B. P.; Light, D.; Clark, T. A.; Huber, M.; Branciforte, J. T.; Stoner, I. B.; Cawley, S. E.; Lyons, M.; Fu, Y. T.; Homer, N.; Sedova, M.; Miao, X.; Reed, B.; Sabina, J.; Feierstein, E.; Schorn, M.; Alanjary, M.; Dimalanta, E.; Dressman, D.; Kasinskas, R.; Sokolsky, T.; Fidanza, J. A.; Namsaraev, E.; McKernan, K. J.; Williams, A.; Roth, G. T.; Bustillo, J. *Nature* **2011**, *475*, 348.

70. Moore, G. E. *Electron.* **1965**, *86*, 114.

71. Huang, X. J.; Lee, W. C.; Kuo, C.; Hisamoto, D.; Chang, L. L.; Kedzierski, J.; Anderson, E.; Takeuchi, H.; Choi, Y. K.; Asano, K.; Subramanian, V.; King, T. J.; Bokor, J.; Hu, C. M. *IEEE Trans. on Electron Devices* **2001**, *48*, 880.

72. Skotnicki, T.; Hutchby, J. A.; King, T. J.; Wong, H. S. P.; Boeuf, F. *IEEE Circuits Devices* **2005**, *21*, 16.

73. Tans, S. J.; Verschueren, A. R. M.; Dekker, C. *Nature* **1998**, *393*, 49.

74. Xuan, Y.; Wu, Y. Q.; Ye, P. D. *IEEE Electron Device Lett.* **2008**, *29*, 294.

75. Patolsky, F.; Zheng, G. F.; Lieber, C. M. *Nat. Protoc.* **2006**, *1*, 1711.

76. Moss, S. D.; Janata, J.; Johnson, C. C. *Anal. Chem.* **1975**, *47*, 2238.

77. Gao, Z. Q.; Agarwal, A.; Trigg, A. D.; Singh, N.; Fang, C.; Tung, C. H.; Fan, Y.; Buddharaju, K. D.; Kong, J. M. *Anal. Chem.* **2007**, *79*, 3291.

78. Lee, D. J.; Chander, Y.; Goyal, S. M.; Cui, T. H. *Biosens. Bioelectron.* **2011**, *26*, 3482.

79. Choi, Y.; Olsen, T. J.; Sims, P. C.; Moody, I. S.; Corso, B. L.; Dang, M. N.; Weiss, G. A.; Collins, P. G. *Nano Lett.* **2013**, *13*, 625.

80. Cao, Q.; Rogers, J. A. *Adv. Mater.* **2009**, *21*, 29.

81. Kang, S. J.; Kocabas, C.; Ozel, T.; Shim, M.; Pimparkar, N.; Alam, M. A.; Rotkin, S. V.; Rogers, J. A. *Nat. Nanotechnol.* **2007,** *2*, 230.

82. Star, A.; Tu, E.; Niemann, J.; Gabriel, J. C. P.; Joiner, C. S.; Valcke, C. *Proc. Natl. Acad. Sci. U. S. A.* **2006**, *103*, 921.

83. Sun, D.; Timmermans, M. Y.; Tian, Y.; Nasibulin, A. G. *Nat. Nanotechnol.* **2011**, *6*, 156.

84. Sorgenfrei, S.; Chiu, C. Y.; Gonzalez, R. L.; Yu, Y. J.; Kim, P.; Nuckolls, C.; Shepard, K. L. *Nat. Nanotechnol.* **2011**, *6*, 125.

85. Kim, Y. A.; Muramatsu, H.; Hayashi, T.; Endo, M.; Terrones, M.; Dresselhaus, M. S. *Chem. Phys. Lett.* **2004**, *398*, 87.

86. Peng, B.; Locascio, M.; Zapol, P.; Li, S. Y.; Mielke, S. L.; Schatz, G. C.; Espinosa, H. D. *Nat. Nanotechnol.* **2008**, *3*, 626.

87. Villalpando-Paez, F.; Son, H.; Nezich, D.; Hsieh, Y. P.; Kong, J.; Kim, Y. A.; Shimamoto, D.; Muramatsu, H.; Hayashi, T.; Endo, M.; Terrones, M.; Dresselhaus, M. S. *Nano Lett.* **2008**, *8*, 3879.

88. Liu, K. H.; Hong, X. P.; Wu, M. H.; Xiao, F. J.; Wang, W. L.; Bai, X. D.; Ager, J. W.; Aloni, S.; Zettl, A.; Wang, E. G.; Wang, F. *Nat. Commun.* **2013**, *4*, 6.

89. Wei, B. Q.; Vajtai, R.; Ajayan, P. M. *Appl. Phys. Lett.* **2001**, *79*, 1172.

90. Cao, Q.; Kim, H. S.; Pimparkar, N.; Kulkarni, J. P.; Wang, C. J.; Shim, M.; Roy, K.; Alam, M. A.; Rogers, J. A. *Nature* **2008**, *454*, 495.

91. Javey, A.; Wang, Q.; Ural, A.; Li, Y. M.; Dai, H. J. *Nano Lett.* **2002**, *2*, 929.

92. Zhang, G. Y.; Qi, P. F.; Wang, X. R.; Lu, Y. R.; Li, X. L.; Tu, R.; Bangsaruntip, S.; Mann, D.; Zhang, L.; Dai, H. J. *Science* **2006**, *314*, 974.

93. Wu, Z. C.; Chen, Z. H.; Du, X.; Logan, J. M.; Sippel, J.; Nikolou, M.; Kamaras, K.; Reynolds, J. R.; Tanner, D. B.; Hebard, A. F.; Rinzler, A. G. *Science* **2004**, *305*, 1273.

94. Huh, J. Y.; Walker, A. R. F.; Ro, H. W.; Obrzut, J.; Mansfield, E.; Geiss, R.; Fagan, J. A. *J. Phys. Chem. C* **2010**, *114*, 11343.

95. Deng, S. L.; Piao, Y. M.; Brozena, A. H.; Wang, Y. H. *J. Mater. Chem.* **2011**, *21*, 18568.

96. Collins, P. C.; Arnold, M. S.; Avouris, P. *Science* **2001**, *292*, 706.

97. Zhou, Y. X.; Gaur, A.; Hur, S. H.; Kocabas, C.; Meitl, M. A.; Shim, M.; Rogers, J. A. *Nano Lett.* **2004**, *4*, 2031.

98. Otsuka, K.; Inoue, T.; Chiashi, S.; Maruyama, S. *Nanoscale* **2014**, *6*, 8831.

99. Khamis, S. M.; Jones, R. A.; Johnson, A. T. C. *AIP Adv.* **2011**, *1*, 5.

100. Kim, T. H.; Lee, S. H.; Lee, J.; Song, H. S.; Oh, E. H.; Park, T. H.; Hong, S. *Adv. Mater.* **2009**, *21*, 91.

101. Li, C.; Curreli, M.; Lin, H.; Lei, B.; Ishikawa, F. N.; Datar, R.; Cote, R. J.; Thompson, M. E.; Zhou, C. *J. Am. Chem. Soc.* **2005**, *127*, 12484.

102. Ganzhorn, M.; Vijayaraghavan, A.; Dehm, S.; Hennrich, F.; Green, A. A.; Fichtner, M.; Voigt, A.; Rapp, M.; Von Löhneysen, H.; Hersam, M. C.; Kappes, M. M.; Krupke, R. *ACS Nano* **2011**, *5*, 1670.

103. Kim, T. H.; Lee, B. Y.; Jaworski, J.; Yokoyama, K.; Chung, W.-J.; Wang, E.; Hong, S.; Majumdar, A.; Lee, S.-W. *ACS Nano* **2011**, *5*, 2824.

104. Forzani, E. S.; Li, X.; Zhang, P.; Tao, N.; Zhang, R.; Amlani, I.; Tsui, R.; Nagahara, L. A. *Small* **2006**, *2*, 1283.

105. Roberts, M. E.; LeMieux, M. C.; Bao, Z. *ACS Nano* **2009**, *3*, 3287.

106. Myung, S.; Solanki, A.; Kim, C.; Park, J.; Kim, K. S.; Lee, K.-B. *Adv. Mater.* **2011**, *23*, 2221.

107. Myung, S.; Yin, P. T.; Kim, C.; Park, J.; Solanki, A.; Reyes, P. I.; Lu, Y.; Kim, K. S.; Lee, K.-B. *Adv. Mater.* **2012**, *24*, 6081.

108. Martínez, M. T.; Tseng, Y.-C.; Ormategui, N.; Loinaz, I.; Eritja, R.; Bokor, J. *Nano Lett.* **2009**, *9*, 530.

109. Liu, K.; Wang, W.; Xu, Z.; Bai, X.; Wang, E.; Yao, Y.; Zhang, J.; Liu, Z. *J. Am. Chem. Soc.* **2009**, *131*, 62.

110. Qi, H.; Qian, C.; Liu, J. *Nano Lett.* **2007**, *7*, 2417.

111. Kalbac, M.; Green, A. A.; Hersam, M. C.; Kavan, L. *ACS Nano* **2010**, *4*, 459.

112. Kalbac, M.; Green, A. A.; Hersam, M. C.; Kavan, L. *Chem. - Eur. J.* **2011**, *17*, 9806.

113. Nair, N.; Kim, W.-J.; Usrey, M. L.; Strano, M. S. *J. Am. Chem. Soc.* **2007**, *129*, 3946.

114. Doyle, C. D.; Rocha, J.-D. R.; Weisman, R. B.; Tour, J. M. *J. Am. Chem. Soc.* **2008**, *130*, 6795.

115. Peng, N.; Zhang, Q.; Chow, C. L.; Tan, O. K.; Marzari, N. *Nano Lett.* **2009**, *9*, 1626.

116. A. M. Munzer, Z. R. Michael, A. Star, *ACS Nano* **2013**, *7*, 7448.

117. F. Patolsky, G. Zheng, C. M. Lieber, *Nanomedicine* **2006**, *1*, 51.

118. R. M. Penner, *Annu. Rev. Anal. Chem.* **2012**, *5*, 461.

119. N. K. Rajan, X. X. Duan, M. A. Reed, *Wiley Interdiscip. Rev. Nanomed. Nanobiotechnol.* **2013**, *5*, 629.

120. I. M. Mackay, K. E. Arden, A. Nitsche, *Nucleic Acids Res.* **2002**, *30,* 1292.

121. G. Mor, I. Visintin, Y. Lai, H. Zhao, P. Schwartz, T. Rutherford, L. Yue, P. Bray-Ward, D. C. Ward, *Proc. Natl. Acad. Sci. U. S. A.* **2005,** *102,* 7677.

122. E. Stern, J. F. Klemic, D. A. Routenberg, P. N. Wyrembak, D. B. Turner-Evans, A. D. Hamilton, D. A. LaVan, T. M. Fahmy, M. A. Reed, *Nature* **2007**, *445*, 519.

123. E. S. Snow, F. K. Perkins, J. A. Robinson, *Chem. Soc. Rev.* **2006**, *35*, 790.

124. A. Abdellah, A. Abdelhalim, M. Horn, G. Scarpa, P. Lugli, *IEEE Trans. Nanotechnol.* **2013**, *12*, 174.

125. C. J. Shih, Q. H. Wang, Z. Jin, G. L. C. Paulus, D. Blankschtein, P. Jarillo-Herrero, M. S. Strano, *Nano Letters* **2013**, *13*, 809.

126. W. Ren, J. R. Reimers, N. S. Hush, Y. Zhu, J. Wang, H. Guo, *J. Phys. Chem. C* **2007**, *111*, 3700.

127. G. Schmidt, S. Gallon, S. Esnouf, J. P. Bourgoin, P. Chenevier, *Chem.-Eur. J.* **2009**, *15*, 2101.

128. I. Heller, A. M. Janssens, J. Mannik, E. D. Minot, S. G. Lemay, C. Dekker, *Nano Lett.* **2008**, *8*, 591.

129. S. S. Mahshid, S. Camire, F. Ricci, A. Vallee-Belisle, *J. Am. Chem. Soc.* **2015,** *137,* 15596.

130. M. H. Park, D. Hang, R. Chand, D. H. Lee, Y. S. Kim, *J. Phys. Chem. C* **2016,** *120,* 4854.

131. M. M. Hamedi, A. Ainla, F. Guder, D. C. Christodouleas, M. T. Fernandez-Abedul, G. M. Whitesides, *Adv. Mater.* **2016**, *28*, 5054.

132. T. Laksanasopin, T. W. Guo, S. Nayak, A. A. Sridhara, S. Xie, O. O. Olowookere, P. Cadinu, F. Meng, N. H. Chee, J. Kim, C. D. Chin, E. Munyazesa, P. Mugwaneza, A. J. Rai, V. Mugisha, A. R. Castro, D. Steinmiller, V. Linder, J. E. Justman, S. Nsanzimana, S. K. Sia, *Sci. Transl. Med.* **2015**, *7,* 273re1.

133. S. P. White, K. D. Dorfman, C. D. Frisbie, *Anal. Chem.* **2015,** *87,* 1861.

134. Ando, T. *NPG Asia Mater.* **2009**, *1*, 17.

135. Wang, W.; Li, S.; Mair, L.; Ahmed, S.; Huang, T. J.; Mallouk, T. E. *Angew. Chem., Int. Ed.* **2014**, *53*, 3201.

136. De Volder, M. F.; Tawfick, S. H.; Baughman, R. H.; Hart, A. J. *Science* **2013**, *339*, 535.

137. De la Zerda, A.; Zavaleta, C.; Keren, S.; Vaithilingam, S.; Bodapati, S.; Liu, Z.; Levi, J.; Smith, B. R.; Ma, T. J.; Oralkan, O.; Cheng, Z.; Chen, X.; Dai, H.; Khuri-Yakub, B. T.; Gambhir, S. S. *Nat. Nanotechnol.* **2008**, *3*, 557.

138. Franklin, A. D.; Luisier, M.; Han, S. J.; Tulevski, G.; Breslin, C. M.; Gignac, L.; Lundstrom, M. S.; Haensch, W. *Nano Lett.* **2012**, *12*, 758.

139. Aguirre, C. M.; Ternon, C.; Paillet, M.; Desjardins, P.; Martel, R. *Nano Lett.* **2009,** *9*, 1457.

140. Nanot, S.; Haroz, E. H.; Kim, J. H.; Hauge, R. H.; Kono, J. *Adv. Mater.* **2012**, *24*, 4977.

141. Park, H.; Afzali, A.; Han, S. J.; Tulevski, G. S.; Franklin, A. D.; Tersoff, J.; Hannon, J. B.; Haensch, W. *Nat. Nanotechnol.* **2012,** *7*, 787.

142. Schvartzman, M.; Tsivion, D.; Mahalu, D.; Raslin, O.; Joselevich, E. *Proc. Natl. Acad. Sci. U. S. A.* **2013**, *110*, 15195.

143. Kim, W.; Choi, H. C.; Shim, M.; Li, Y. M.; Wang, D. W.; Dai, H. J. *Nano Lett.* **2002,** *2*, 703.

144. Piao, Y. Electronically Tailored Functionalization of Carbon Nanotubes. Ph. D. Dissertation, University of Maryland, College Park, MD, **2014**.

145. Dresselhaus, M. S.; Dresselhaus, G.; Saito, R.; Jorio, A. *Phys. Rep.* **2005,** *409*, 47.

146. Kataura, H.; Kumazawa, Y.; Maniwa, Y.; Umezu, I.; Suzuki, S.; Ohtsuka, Y.; Achiba, Y. *Synth. Met.* **1999**, *103*, 2555.

147. Kim, Y. A.; Hayashi, T.; Osawa, K.; Dresselhaus, M. S.; Endo, M. *Chem. Phys. Lett.* **2003**, *380*, 319.

148. Bahr, J. L.; Yang, J.; Kosynkin, D. V.; Bronikowski, M. J.; Smalley, R. E.; Tour, J. M. *J. Am. Chem. Soc.* **2001**, *123*, 6536.

149. Mases, M.; Noël, M.; Dossot, M.; McRae, E.; Soldatov, A. V. *Phys. Status Solidi B* **2011**, *248*, 2540.

150. Zandian, B.; Kumar, R.; Theiss, J.; Bushmaker, A.; Cronin, S. B. *Carbon* **2009**, *47*, 1292.

151. Avouris, P.; Chen, Z.; Perebeinos, V. *Nat. Nanotechnol.* **2007**, *2*, 605.

152. Rao, C. e. N. e. R.; Sood, A. e. K.; Subrahmanyam, K. e. S.; Govindaraj, A. *Angew. Chem. Int. Ed.* **2009**, *48*, 7752.

153. Jariwala, D.; Sangwan, V. K.; Lauhon, L. J.; Marks, T. J.; Hersam, M. C. *Chem. Soc. Rev.* **2013**, *42*, 2824.

154. Bianco, A.; Kostarelos, K.; Prato, M. *Curr. Opin. Chem. Biol.* **2005**, *9*, 674

155. Liu, Z.; Robinson, J. T.; Sun, X.; Dai, H. *J. Am. Chem. Soc.* **2008**, *130*, 10876.

156. Kwon, H.; Kim, M.; Meany, B.; Piao, Y.; Powell, L. R.; Wang, Y. *J. Phys. Chem. C* **2015**, *119*, 3733.

157. Ramanathan, T.; Abdala, A.; Stankovich, S.; Dikin, D.; Herrera-Alonso, M.; Piner, R.; Adamson, D.; Schniepp, H.; Chen, X.; Ruoff, R. *Nat. Nanotechnol.* **2008**, *3*, 327.

158. Spitalsky, Z.; Tasis, D.; Papagelis, K.; Galiotis, C. Carbon nanotube–polymer composites: chemistry, processing, mechanical and electrical properties. *Prog. Polym. Sci.* **2010**, *35*, 357.

159. Hecht, D. S.; Hu, L.; Irvin, G. *Adv. Mater.* **2011**, *23*, 1482.

160. Someya, T.; Small, J.; Kim, P.; Nuckolls, C.; Yardley, J. T. *Nano Lett.* **2003**, *3*, 877.

161. Staii, C.; Johnson, A. T.; Chen, M.; Gelperin, A. *Nano Lett.* **2005**, *5*, 1774.

162. Kuang, Z.; Kim, S. N.; Crookes-Goodson, W. J.; Farmer, B. L.; Naik, R. R. *ACS Nano* **2009**, *4*, 452.

163. Zhao, G.; Li, J.; Ren, X.; Chen, C.; Wang, X. *Environ. Sci. Technol.* **2011**, *45*, 10454.

164. Kyzas, G. Z.; Deliyanni, E. A.; Matis, K. A. *J. Chem. Technol. Biotechnol.* **2014**, *89*, 196.

165. Umek, P.; Seo, J. W.; Hernadi, K.; Mrzel, A.; Pechy, P.; Mihailovic, D. D.; Forró, L. *Chem. Mater.* **2003**, *15*, 4751.

166. Tasis, D.; Tagmatarchis, N.; Bianco, A.; Prato, M. *Chem. Rev.* **2006**, *106*, 1105.

167. Zhao, Y.-L.; Stoddart, J. F. *Acc. Chem. Res.* **2009**, *42*, 1161.

168. Ng, A. L.; Wang, Y. In *A tube-in-a-tube semiconductor*, Active-Matrix Flatpanel Displays and Devices (AMFPD), 2016 The 23rd International Workshop on Active-Matrix Flatpanel Displays and Devices, FTFMD: 2016; pp 42-44.

169. Yan, Z.; Peng, Z.; Casillas, G.; Lin, J.; Xiang, C.; Zhou, H.; Yang, Y.; Ruan, G.; Raji, A.-R. O.; Samuel, E. L. *ACS Nano* **2014**, *8*, 5061.

170. Lin, J.; Zhang, C.; Yan, Z.; Zhu, Y.; Peng, Z.; Hauge, R. H.; Natelson, D.; Tour, J. M. *Nano Lett.* **2013**, *13*, 72.

171. Zhu, Y.; Li, L.; Zhang, C.; Casillas, G.; Sun, Z.; Yan, Z.; Ruan, G.; Peng, Z.; Raji, A. R.; Kittrell, C.; Hauge, R. H.; Tour, J. M. *Nat. Commun.* **2012**, *3*, 1225.

172. Li, Y.; Peng, Z.; Larios, E.; Wang, G.; Lin, J.; Yan, Z.; Ruiz-Zepeda, F.; José-Yacamán, M.; Tour, J. M. *ACS Nano* **2014**, *9*, 532.

173. Lomeda, J. R.; Doyle, C. D.; Kosynkin, D. V.; Hwang, W.-F.; Tour, J. M. *J. Am. Chem. Soc.* **2008**, *130*, 16201.

174. Crowley, K.; O'Malley, E.; Morrin, A.; Smyth, M. R.; Killard, A. J. *Analyst* **2008**, *133*, 391.

175. Pandey, S.; Goswami, G. K.; Nanda, K. K. *Carbohydr. Polym.* **2013**, *94*, 229.

176. Dar, G.; Umar, A.; Zaidi, S. A.; Baskoutas, S.; Hwang, S.; Abaker, M.; Al-Hajry, A.; Al-Sayari, S. *Talanta* **2012**, *89*, 155.